Bubble-Induced Vibration in Liquid Nitrogen Cryopump

A Thesis Submitted to

Nirma University

In Partial Fulfilment of the Requirements for

The Degree of

Doctor of Philosophy

in

Technology and Engineering

By

Manoj Kumar Gupta

(13EXTPHDE99)

Institute of Technology

Nirma University

Ahmedabad – 382481

Gujarat, India

NIRMA UNIVERSITY

INSTITUTE OF TECHNOLOGY

NAAC ACCREDITED 'A' GRADE

April, 2017

Nirma University

Institute of Technology

Certificate

This is to certify that the thesis entitled **Bubble-Induced Vibration in Liquid Nitrogen Cryopump** has been prepared by **Mr. Manoj Kumar Gupta (13EXTPHDE99)** under my supervision and guidance. The thesis is his own original work completed after careful research and investigation. The work of the thesis is of the standard expected of a candidate for Ph.D. Programme in **Mechanical Engineering** and I recommend that it be sent for evaluation.

Date: D. S. Sharma

Signature of Guides

Forwarded through:

(i) Head, Mechanical Engineering Department

(ii) Dean, Faculty of Technology and Engineering

25/4/2017 . (Dr. M. Ghate)

(iii) Dean, Faculty of Doctoral Studies and Research

To:

Executive Registrar

Nirma University

Nirma University
Institute of Technology

Declaration

I, **Manoj Kumar Gupta**, registered as Research Scholar, bearing Registration No. **13EXTPHDE99** for Doctoral Programme under the **Faculty of Technology and Engineering** of Nirma University do hereby declare that I have completed the course work, pre-synopsis seminar, and my research work as prescribed under R. Ph.D. 3.5.

I do hereby declare that the thesis submitted is original and is the outcome of the independent investigations / research carried out by me and contains no plagiarism. The research is leading to the discovery of new facts / techniques / correlation of scientific facts already known. This work has not been submitted to any other University or Body in quest of a degree, diploma or any other kind of academic award.

I do hereby further declare that the text, diagrams or any other material taken from other sources (including but not limited to books, journals, and the web) have been acknowledged, referred and cited to the best of my knowledge and understanding.

Date:

Manoj Kumar Gupta
13EXTPHDE99

I endorse the above declaration made by the student.

D.S.Sharma

Dr D S Sharma		Dr V J Lakhera

Acknowledgment

First of all, I praise Almighty God. Without his blessings and mercy, it was not possible to complete the work successfully. As a part of his tremendous support, I was associated with the people whose names I feel privileged to mention here.

Due to the grace of God, Dr. Dharmendra S Sharma accepted me as a Ph. D. student. I express my deepest sense of gratitude towards him for his constant warm encouragement, motivation, thoughtful guidance and critical comments. His critical thinking developed my overall personality. I thanks to God that I got the opportunity to work under his guidance.

I am very fortunate to have another guide as Dr. V. J. Lakhera. I would like to express my heartly thanks to him for the fruitful discussion, trust, offering valuable advice and support during the entire period of my work. Your key role can't be replaced by anybody else.

I would like to express sincere thanks to Head of the Department Dr. R N Patel and Director Dr. Alka Mahajan for kind support in all the respects during my study.

I would also like to thank my Research Progress committee members, Dr. D. P. Vakharia and Dr. R. N. Patel for their excellent advises and positive comments. Their suggestions provided proper direction to complete the study.

I am grateful to my parents and my family for extending their full support. Without their well wishes, it was looking difficult task.

Last but not the least, I also thank all my colleagues, friends and all well-wishers for their direct or indirect support, made some contributions by the way of discussions, helpful suggestions, etc.

Date: 5 April 2017 Manoj Kumar Gupta (13EXTPHDE99)

Abstract

Gravitational Waves (GW) predicted by Einstein in 1915 were detected by LIGO (Laser Interferometer Gravitational-Wave Observatory) on September 14, 2015. This is the first direct detection of GW and the first observation of a binary black hole merger. The comparative low signal of the GW makes the observation very challenging; however, continuous improvement in detection equipment will open to observe more phenomenon of the universe.

Liquid Nitrogen Cryopump is one of the key components of LIGO system to maintain the UHV and also the main source of noise due to bubbles. The bubble induced noise is one of the noises that could distort the signal. Cryogenic fluids are always in the boiling modes and inducing the bubble noise continuously.

The present work is an attempt to theoretically investigate bubble induced vibration and noise with the help of bubble dynamics. The configuration of LN2 cryopump as circular concentric shell makes the investigation more challenging. The departure force on the liquid nitrogen bubble is of the order of 10^{-5} N, which provides the initial acceleration of ~2g. The bubble moves through the liquid nitrogen and impacts the surface, which produces the vibration and noise. The noise is analyzed in terms of force, acceleration, velocity and the displacement. The induced noises are in the range -16 dB to -146 dB. This work will open the new window for the cryogenic fluid usability for the vibration free environment. Hence it is a new emerging area of investigation.

Keywords: Cryopump, Liquid nitrogen, Vibration, Bubble, Noise

Contents

List of Figures

List of tables

Chapter 1

Introduction

1.1. Preliminary remarks

The novel exploration by research scholars and their innovative attitude towards the development of science and technology has provided a substantive platform for the work of the science edification research community for the past 40 years. Scientific discoveries are being made every day that is changing the material world. Great Scientists such as Einstein, Newton, and others revealed the knowledge of nature in terms of physics creating new avenues for research.

1.2. Gravitational Waves (GW)

The gravitational waves are produced by the interaction between two or more compact massive objects (Fig. (1.1)); such interaction includes rotation, orbiting and spinning i.e. two neutron stars, two black holes, or a neutron star and a black hole etc.

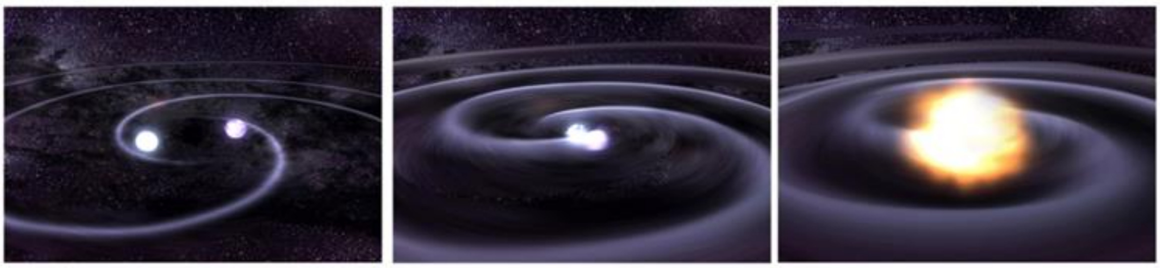

Figure 1.1 Sources of Gravitational Waves due rotation of two massive objects

[Courtesy - LIGO, USA]

These waves produce ripples in space-time fabric (Fig. (1.2)) of the universe thereby changing its dimension as predicted by Einstein.

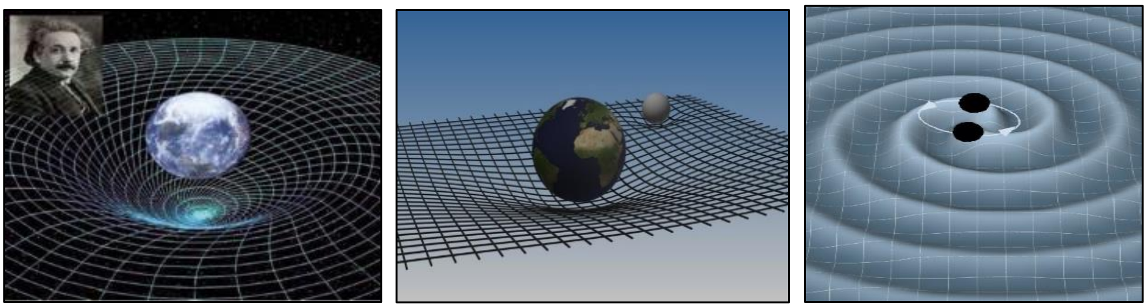

Figure 1.2 Space-Time Fabric of gravity [Courtesy - LIGO, USA]

Hence the space fabric first elongates in one direction (i.e. X-direction) and contracts in the direction perpendicular to it (i.e. Y-direction), then it becomes circular by contracting in X-direction and elongating in Y-direction as shown below (Fig. (1.3)). The continuous cycle of elongation and contraction produces gravitational wave signals in the fabric of space-time.

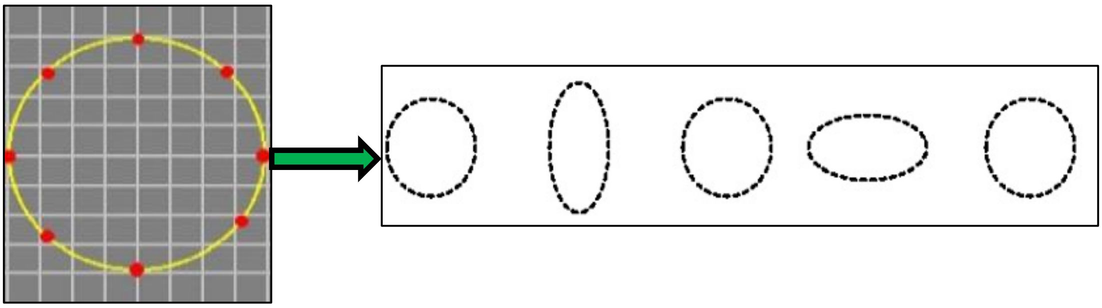

Figure 1.3 Gravitational wave with amplitude h and (+) polarization, propagating perpendicular to the plane of the detector

1.3. Laser Interferometer Gravitational-wave Observatory (LIGO)

The comparative low signal of the gravitational wave makes the observation very challenging; however, continuous improvement in detection equipment has opened up the door to spot gravitational waves. Recently, on September 14, 2015 the two detectors of LIGO observed a transient GW signal [1] as shown in Fig (1.4).

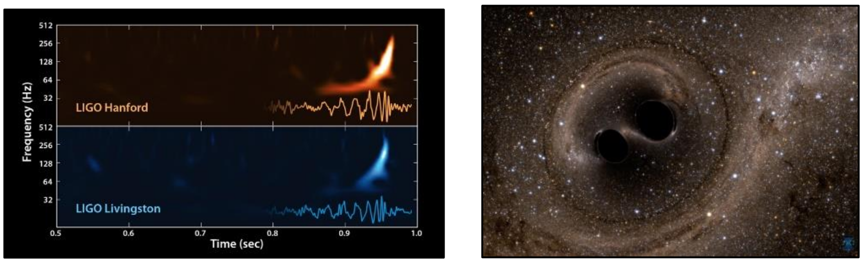

Figure 1.4 Signal detected by LIGO detectors from two black hole merger [1]

The signal sweeps upwards in frequency from 35 to 250 Hz with a peak GW strain of 1.0×10^{-21}. It confirmed the two black hole merger in the space and confirmed the theory of Einstein predicted before 100 years. This is the first direct detection of GW and first observation of a binary black hole merger. Hence, it is a breakthrough in the physics.

In the initial phase, LIGO designed and developed the technologies to be utilized in achieving the target sensitivity curve having a minimum sensitivity of $\sim 1.0 \times 10^{-19}$ meters/$\sqrt{Hz}$ at ~ 150 Hz [2]. Advanced LIGO interferometers was targeted having strain sensitivities on the order of ~ 10^{-24} meters/$\sqrt{Hz}$ between 10 Hz to 10 kHz [2]. The most sensitive strain measurement is provided by the LIGO and VIRGO observatories (Fig. (1.5)).

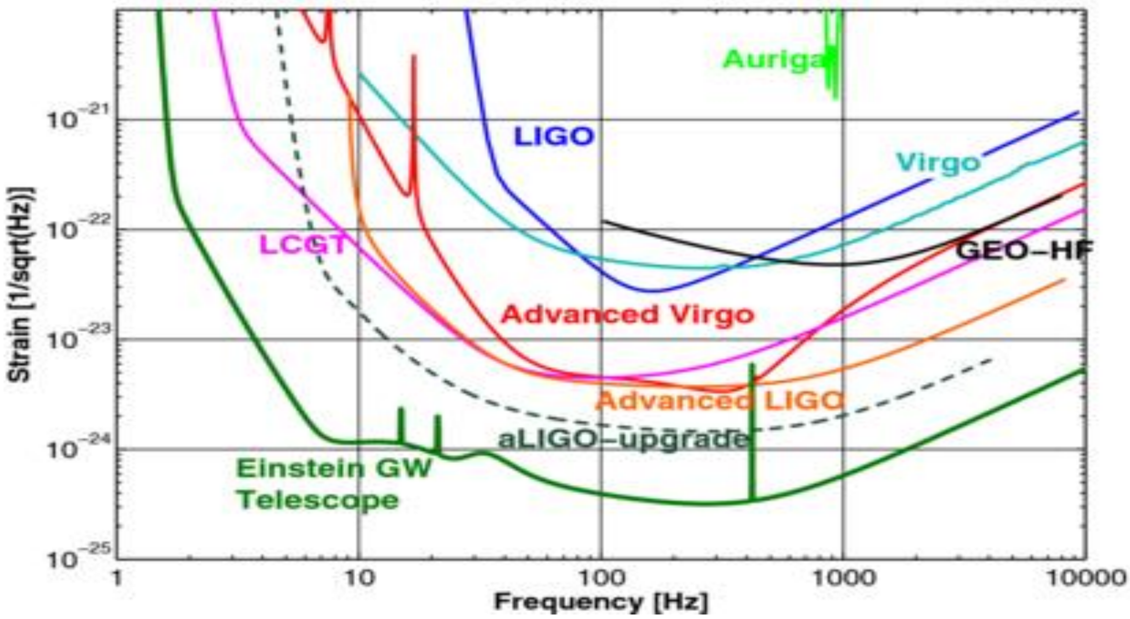

Figure 1.5 Detector Sensitivity of iLIGo, eLIGO and aLIGO [Courtesy - LIGO, USA]

Low sensitivity measurement from the initial LIGO provides detection of few events i.e. ~ 1-2 events per year. Therefore it is very difficult to extract these events. Hence LIGO is continuously improving towards the advanced LIGO called as Adv. LIGO or aLIGO. Increasing the sensitivity by 10 times increases the observable volume of space i.e. the galaxies by 1000 times (Fig. (1.6)). As a result, several events per year would be able to observe.

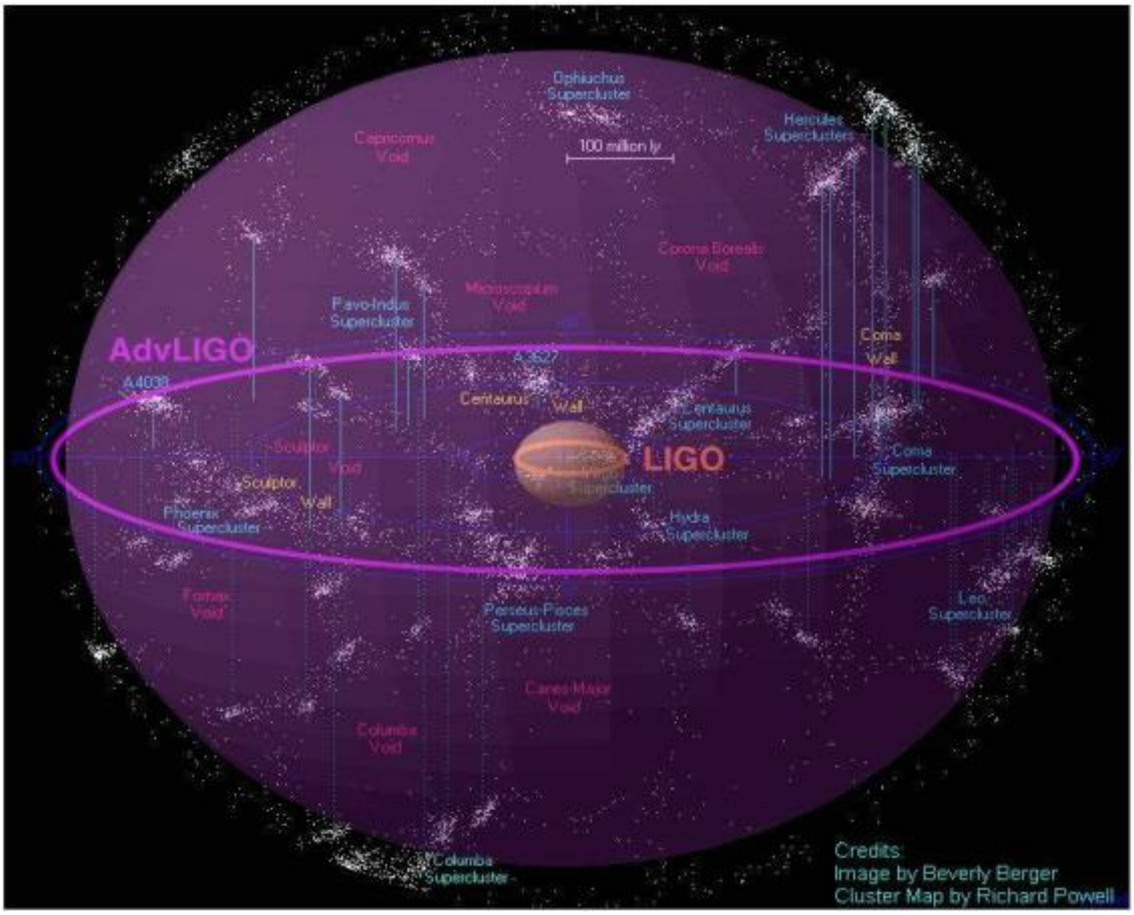

Figure 1.6 Comparison of LIGO and a LIGO [Courtesy - LIGO, USA]

The sensitivity of detectors is usually limited by various sources of noise i.e. Mirror/test mass related noise; Vibration Isolation noise; Michelson interferometer system related noise, Laser related noise etc. Sensing a real GW event requires an isolated region, free from vibrations and noises.

The LIGO System needs to detect the strain sensitivity displacement in two directions as per the changes in the space-time fabric. Hence the system involves the use of various components in X and Y direction as shown in Fig. (1.7);

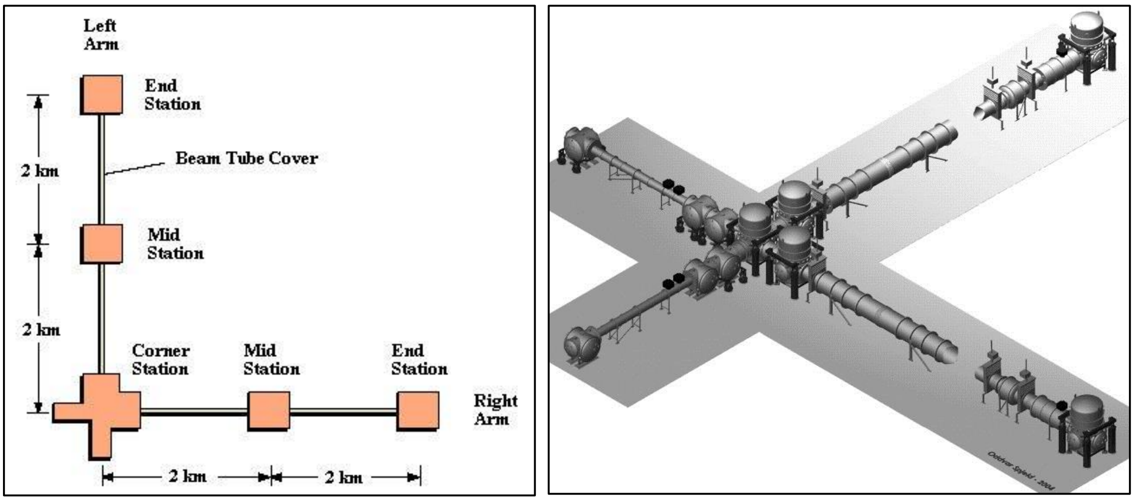

Figure 1.7 Schematic of LIGO and its Components (Courtesy: LIGO-USA)

1.4. Motivation

Recently, Physicists around the world have confirmed that they had detected unambiguous signals of gravitational waves emanating from the collision of two massive black holes 1.5 billion light years away in deep space [1]. The observation of GW marks three milestones for physics: the direct detection of gravitational waves, the first observation of a binary black hole, and the most convincing evidence to-date that nature's black holes are the objects predicted by Einstein's theory. To increase the frequency of observation of different events, the sensitivity should be very high. Any stone towards more sensitive detectors should not left to be unturned.

Liquid Nitrogen Cryopump is one of the key components of LIGO system to maintain the UHV and also the main source of noise due to bubbles. It has been observed at VIRGO that the noise around 50-150 Hz is enhanced by about 5 times by the action of LN2 bubbles [3]. Sensitivity being the major issue, lot of research has been done to create a vibration free environment by eliminating even the minute noises that could distort the signal.

The present work is an attempt to aim theoretically investigate and attenuate the risks linked with the LN2 bubble induced noise that could limit the measurement of the detection. There is no literature available on the bubble induced vibration in cryogenic fluids. Moreover conducting an experiment for LN2 bubble is very difficult and expensive. So an experiment can be performed as the future scope. In this case, the theoretical investigation becomes very-very important to find out the LN2 bubble induced vibration. This work will open the new window for the cryogenic fluid usability towards vibration free environment. Hence it is a new emerging area of investigation.

1.5. Objectives of the present study

The investigations have been carried out with considering following objectives.

- To provide a generalized analytical formulation of bubble-induced vibration and noises (Force, Acceleration, Velocity, and Displacement).
- To study the effect of bubble diameter and cylindrical shell thickness on the noise levels.
- To formulate the bubble dynamics for the bubble motion during nucleate boiling phenomenon.
- To decide the thickness of the cylindrical shells based on the mechanical strength.
- To detect the natural frequencies related to the different mode shapes for the liquid nitrogen cryopump configuration.
- To avoid the low-frequency modes and to match the mode shapes of the outer and inner shell for the low vibration of fluid.

1.6. Aims and scope of the present study

The purpose of the present study is to establish mathematical formulation for the low vibration and low noise liquid nitrogen cryopump. The low natural frequency mode shapes have to be avoided so that the low-frequency GW signals can be detected. The main aim to avoid the natural frequency of vibration below 100 Hz. The configuration is concentric cylindrical shells, which is totally different than any of the configuration studied so far. The general methodology has been developed for the bubble motion, impact on the surface and inducing the noise in the cryopump. The present formulation is studied for the different methods to reduce the noise.

The presented study is based on following assumptions.

- The bubble diameter is assumed constant during the motion within the fluid.
- The shape of the bubble is taken as the spherical in size.
- The material of the liquid nitrogen cryopump is taken as SS304L as per the cryogenics and vacuum consideration.
- The fixed-fixed beam condition is considered for the cryopump due to having supports and end rings at the ends.

1.7. Thesis outline

The thesis consists of six Chapters.

Chapter 1 provides the base for the problem as per application point of view. The introduction of the application, motivation, objectives, aims, and scope of the present study are also presented.

Chapter 2 presents the literature review related to the study. On the basis of a literature survey, research gaps are identified.

Chapter 3 deals with the detailed analytical formulation for the single bubble dynamics. Different forces responsible for the departure of the bubble are studied. Due to the bubble departure force, the bubble acceleration, velocity, and displacement characteristics are also presented.

Chapter 4 provides the formulation of all the mathematical base to find out the bubble induced vibration and noise. The chapter also includes the design, analysis and natural frequency of the cryopump.

Chapter 5 describes all the results in the numerical and graphical form for the cryopump. The parametric optimization of the different parameters for the low vibration and low noise cryopump is also presented.

Chapter 6 summarizes the presented work. The limitations of the present study and future scope of the work are also addressed.

The list of publications and cited references are enumerated at the last.

Chapter 2

Literature Review

2.1. Introduction

The cryogenic 80K pumps consist of exposed surfaces refrigerated to a cryogenic temperature upon which gasses are condensed. The proposed pumps use liquid nitrogen that boils at atmospheric pressure at a temperature of 80K. The boiling action of liquid nitrogen involves cavitation (i.e. vapour bubble formation and collapse) which produces broad spectrum pressure pulses that act on the vessel and liquid/air surfaces to produce noise and vibration. The bubbles generated from the boiling liquid in the reservoir are smaller and generate higher frequencies. These vibrations affect the interferometer data and analysis hence these vibrations have to be investigated.

The present literature review details out the research carried out in the field of vibration produced by the Liquid Nitrogen bubble cavitation in Cryogenic 80K pumps, theories on bubble formation and its dynamics along with the vibration mitigation.

2.2. Major objectives of previous studies

A lot of research and experiments have been performed on the areas of vapour bubble such as bubble growth and its nucleation in superheated liquids, bubble formation mechanism, pool boiling heat transfer, two-phase flow boiling, flow boiling in micro-channels, bubble dynamics, observation and analysis of bubble detachment frequency, kinematic model of bubble motion forces acting on a growing bubble. This section outlines the following major goals of investigations done in these areas.

- Bubble dynamics

- Bubble nucleation and growth
  - Inertial controlled growth and
  - Heat transfer controlled growth
- Bubble departure diameter
- Bubble release / departure frequency
- Boiling phenomenon i.e. heat transfer characteristics
  - Pool boiling
  - Flow boiling
- Forces acting on the departing bubble
  - Horizontal forces
  - Vertical forces

- Bubble-Induced Vibration - Only a few basic studies have been carried out for investigating the induced vibration
  - Subcooled Boiling Induced Vibration (SBIV)
  - Flow Induced Vibration (FIV)

Most of all these works are concerned regarding the behavior and actions of vapour bubble in different environmental and physical conditions. The vibrations produced due to the striking of bubbles on the surface is a new challenging area of investigation. However, the present work is an attempt to investigate the vibration issues that are usually found due to bubble-structure interaction. This bubble structure interaction held in the reservoir part of the Cryopump used for achieving the vacuum. This work would extensively help out in eliminating the vibration concerns required for measuring the gravitational waves of low frequency.

2.3. Bubble dynamics

To investigate the bubble induced vibration, bubble dynamics (i.e. the bubble formation, growth, departure dia etc.) provides crucial parameters for analysis.

2.3.1. Bubble nucleation and growth

The vapour bubble formation process in a liquid is called bubble nucleation. The bubble nucleation takes place due to the dissolved gas in the liquid, pre-existing gas in the surface cracks or imperfect surface, phase transformation i.e. boiling etc. The nucleation can be

- Homogeneous
- Heterogeneous

Bubble nucleation process mainly depends on the magnitude of super-saturation state and the threshold value. The nucleation occurs when the super-saturation value in gas-supersaturated liquids supersedes the threshold value [4]–[7]. In the case of homogeneous nucleation; the value of the threshold is governed by the interactions between the molecules of gas and liquid existing in the fluid medium while for heterogeneous nucleation, its value is additionally governed by the region between solid and liquid [8], [9]. Therefore, nucleation thresholds for homogeneous and heterogeneous conditions tend to vary significantly. Moreover, the magnitude of the threshold for homogeneous nucleation is quite less compared to homogeneous nucleation. The possible significance of these results have not been fully appreciated. Homogeneous nucleation is mostly considered in the theoretical analysis and is quite rarely found in engineering applications [10].

The distinction between Homogeneous and Heterogeneous nucleation has been described in Table (2.1).

Table 2.1 Homogeneous and Heterogeneous nucleation

Homogeneous nucleation	**Heterogeneous nucleation**
Prevails in the liquid in which there is no contact with any other foreign substance or surface.	Prevails due to the presence of super saturated diffused gas on the surface grows spontaneously to form bubbles.
Nucleation begins when a very small volume of liquid molecules (embryo) reaches a vapour state.	Nucleation begins due to imperfectness of the surface and dissolved gas starts expansion
Very large superheat is required for homogeneous nucleation.	Low degree of superheat is needed for the nucleation.

Oxtoby [11] studied the recent improvised form of experimental and theoretical progress in the area of homogeneous classical nucleation highlighting the phase transitions in single component liquid. Jones et al. [12] detailed out the subject of bubble nucleation in the area of non-classical nucleation in a liquid supersaturated with gas and the nucleation that occurs at definite sites.

Gerth and Hemmingsen [13] studied the threshold for bubble nucleation in biological significance such as human and animal tissues. Experiments were performed using the crystallized solids formed from aqueous solutions cooled at pressures up to 240atm. Both the bubble nucleation effect at the solid-liquid region involving Nitrogen, Argon and Methane and the influence of cavitation in supersaturated solutions can be estimated with and without the crystal-like precipitates.

The fundamental mechanism of bubble nucleation in the chamber has merely been considered. However, this mechanism has been extensively used for improving the bubble chambers and carrying out the experiments in areas related to High Energy Physics. Tenner [14] presented a novel approach to generate a bubble in a superheated liquid with the help of high energy charged particles. The potential energy between molecules, i.e. surface energy requirements for the formation of the vapour bubble in gas-liquid phase is limited due to the solute-solvent interaction. Most of the models of bubble nucleation consider the effect of cavity formation under tension. However, Kwak et al. [15] derived a cluster model according to the scaling transformation valid for both gas and vapour bubble formation. While considering the phenomenon of boiling in a superheated liquid, the coupling of energy and momentum equation is highly essential. Moreover, the coupling of equations is also a mandate in the case of gas bubble formation. The areas related to vapour bubble formation and their possible interactions during the boiling phase were not looked upon previously.

As the technological advancement, the high-speed imaging cameras with powerful resolutions and high-end computer processors are in use to detail out the bubble growth and detachment process. S. Siedel et al. [16] experimentally concentrated on a single nucleation site for the various degree of superheats. The growth, detachment and interaction of bubbles has been recorded as shown in Fig. (2.1).

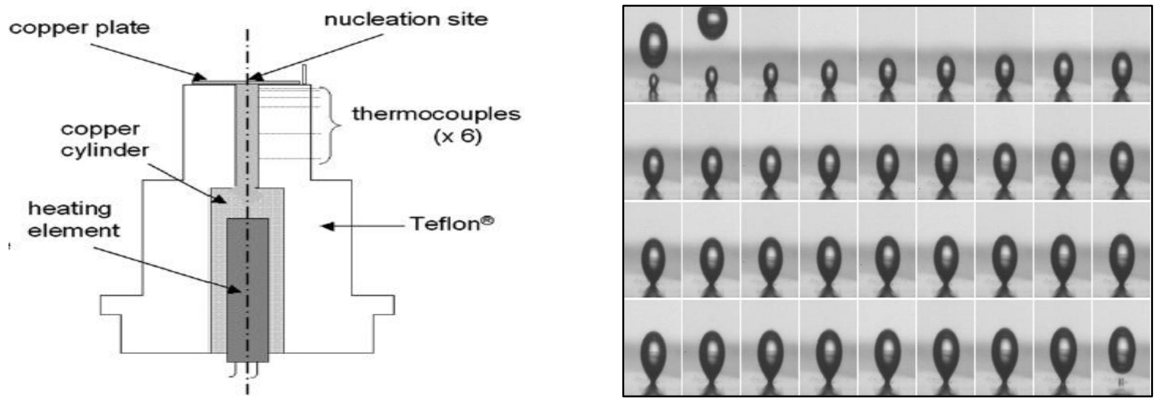

Figure 2.1 Experimental set up with recorded images of bubble growth from single nucleation site (375 frames per sec) [16]

X. Fu et al. [17] visualized and quantitatively investigated the bubble growth, departure, and the following flow pattern evolution during flow boiling in the mini-tube. Fig. (2.2) shows the used test section and a series of visualization images in one typical bubble period, during which bubble growth time and waiting time are about 4 ms and 8 ms, respectively.

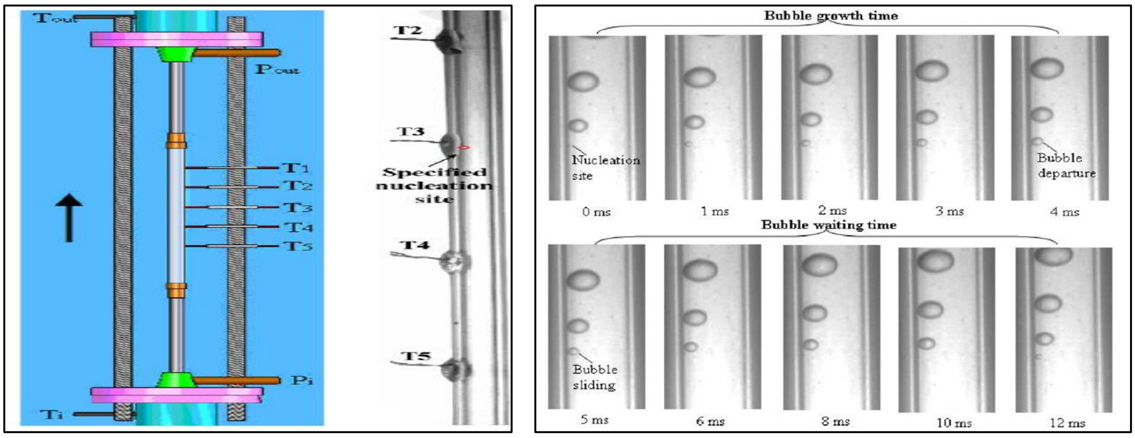

Figure 2.2 The test section: (a) schematic of the test section arrangement and (b) photography image (the specified nucleation site is close to T3) (c) Typical bubble growth and waiting time from a single nucleation site at G = 9.1 kg/m^2 s, P_{in} = 103.1 kPa, T_{in} = 77.5 K, q = 5200 W/m^2, D_i = 1.33 mm [17]

Bradley et al. [18] examined the significance of heat transfer rate on different metallic surfaces (30–365 nm RMS roughness) such as brass, stainless steel (electro-polished and unpolished) under heterogeneous nucleate boiling conditions. The experiment was performed on a pool boiling chamber and the evolution of nucleation site density after incipience of the first bubble for the boiling of pentane was observed shown in Fig. (2.3).

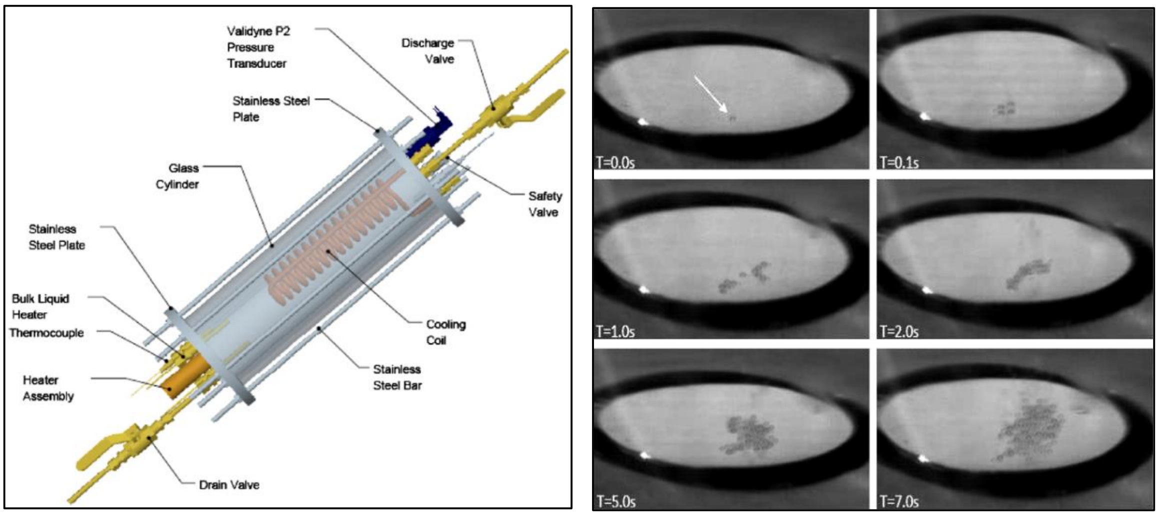

Figure 2.3 Experimental pool boiling facility and Evolution of nucleation site density after incipience of the first bubble for boiling of pentane on the brass surface (ΔT_{sat} = 11.8°C, P = 280 kPa) [18]

It was observed that the rate of heat transfer from a polished stainless steel surface is relatively smaller than the brass surface.

Also, the effect of bubble interaction from the adjacent nucleation sites was investigated in a boiling liquid. Han and Griffith [19] introduced the concept of a gas-filled cavity for the vapour bubble formation. A superheated interface layer of liquid was developed on the contact surface near the cavity, and it was found that surface characteristics, as well as surrounding liquid temperature significantly, affect the temperature needed for bubble formation.

2.3.2. Bubble growth

The bubble growth process begins after the nucleation stage and continues to grow further to the point of detachment from the heated surface. Various properties of the liquid like inertia, surface tension, molecular diffusion, and viscosity are crucial for determining the growth rate. The controlling properties during the early growth period of a bubble are still indistinguishable.

In a subcooled boiling process [20], an active nucleation site produces vapour bubbles which go through a typical periodic cycle of nucleation, growth, departure and collapse (condensation) followed by a waiting period (Fig. (2.4)).

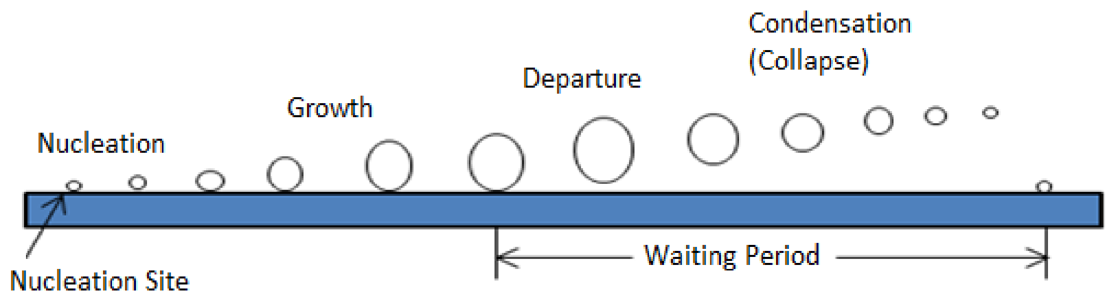

Figure 2.4 Schematic diagram of bubble growth and collapse process

The volume of the bubble also changes accordingly as shown in Fig. (2.5),

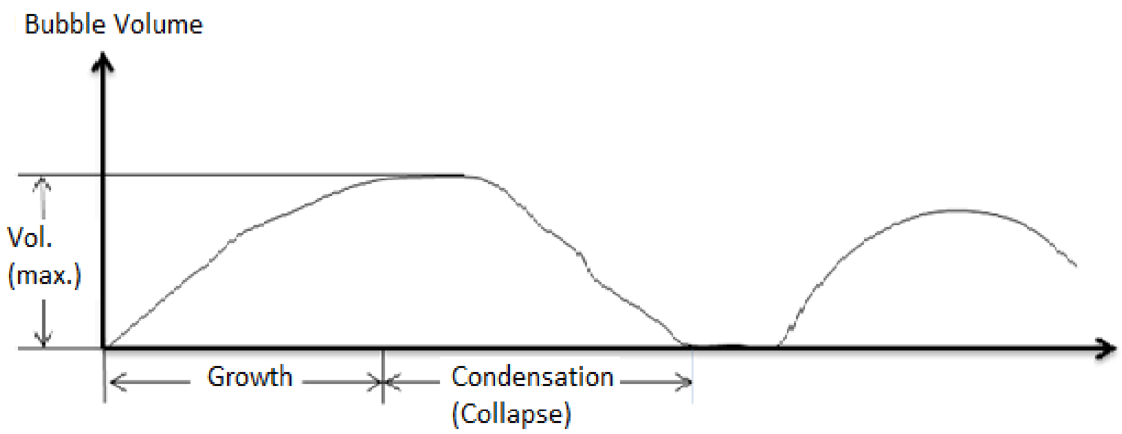

Figure 2.5 Typical bubble growth and collapse curve

In the nucleate boiling process, Hsu et. al [21] examined the bubble growth cycle through various analytical methods and experiments. Then he concluded that this process takes place in four stages as shown in Fig. (2.6),

1. Bubble growth as hemisphere either the nucleation site is of any shape
2. Development of the microlayer nearby boundary of bubble growth
3. Shaping of bubble due to the buoyancy and surface tension force

4. Detachment of the bubble after the net force opposite to solid surface

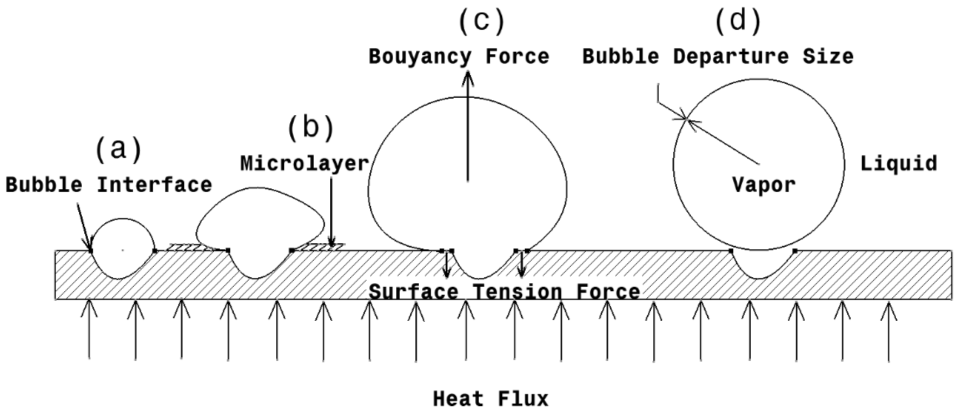

Figure 2.6 Bubble growth and detachment stages

After the growth period, bubble detaches from the heated surface by destroying the thermal boundary layer and allowing colder liquid from the bulk to cover up the space left by a departed bubble. A new cycle begins as the thermal layer starts to recover. The period for recovering the thermal layer is called as the waiting period. It was reported that the bubble waiting period is larger than the growth period and is dependent upon cavity size r_c as well as the local thermal boundary layer thickness δ [22].

Analytical solutions for initial stages of bubble evolution, critical radius, and the governing criteria were not described explicitly. Lee and Merte [23] derived its detailed analytical solutions and conditions by considering a bubble of spherical shape with homogeneous superheated liquid. Due to unavailability of the suitable correlation involving the radius of vapour bubble, ‘R’ and growth time, ‘t’ (i.e. bubble growth rate), various theoretical and experimental studies were carried out. As a result, the relationship was estimated as $R \sim t^a$ [24], [25]. The value of the exponent ‘a’ varies from 0.3-0.75 due to the effect of various governing forces which includes viscous, inertial and differential pressure. Haustein et al. also confirmed the value of a as 0.33 for the condition of medium-high superheat bubble growth [26].

2.3.2.1Inertial controlled bubble growth

The phenomenon of inertia controlled bubble growth and collapse was first established by Rayleigh [27]. The equations of motion were derived by considering a bubble of spherical shape. In an inertia controlled Bubble growth process, a vapour bubble is assumed to be spherical under the uniformly superheated liquid. The radius of the bubble is expanding from Ro (initial) to R in an infinite, incompressible, non-viscous liquid with constant excess pressure as shown in Fig. (2.7).

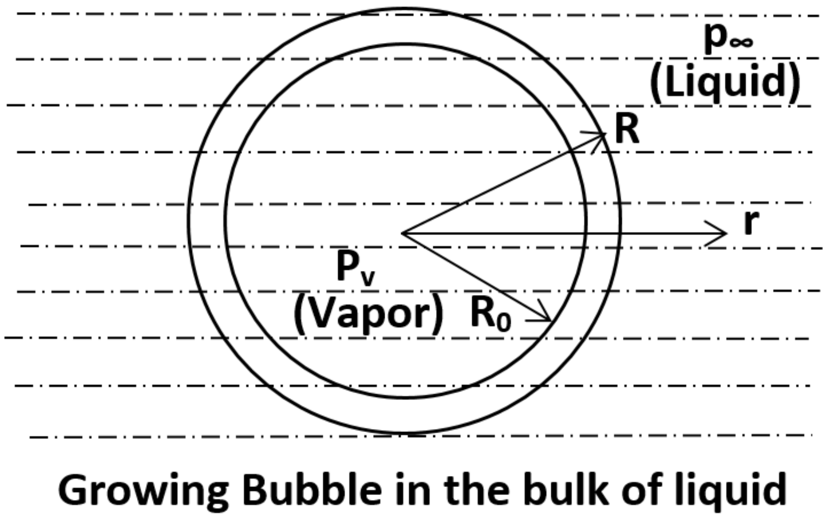

Figure 2.7 Spherical vapour bubble present in the unbounded liquid

The energy conservation with these assumptions yields the following equation [28],

$$\frac{1}{2}\rho_L \int_R^{\infty} 4\pi r^2 \dot{r}^2 dr = \frac{4\pi}{3}(R^3 - R_o^3)\Delta p \qquad (2.1)$$

where $\Delta p = p_V - p_\infty$. This equation combined with the continuity requirement $(r/R)^2 = (\dot{R}/\dot{r})$, results in the inertia controlled bubble growth equation known as the generalized Rayleigh's equation:

$$R\frac{d^2R}{dt^2} + \frac{3}{2}\left(\frac{dR}{dt}\right)^2 = \frac{1}{\rho_L}\left(p_V - p_\infty - \frac{2\sigma}{R}\right) \qquad (2.2)$$

A solution to Eq. (2.2) is given by the following:

$$R(t) = \left\{\frac{2}{3}\left(T_\infty - T_{sat}(P_\infty)\left(\frac{h_{lv}\rho_G}{\rho_L}\right)\right)\right\}^{\frac{1}{2}} t \qquad (2.3)$$

This equation can be further reduced and can be approximated as [29]:

$$R \cong \left(\frac{2\Delta p}{3\rho_L}\right)^{\frac{1}{2}} t \qquad (2.4)$$

The vapour inside the bubble is presumed to be in a saturated state corresponding to the superheated liquid temperature. As long as this assumption holds, the vapour pressure of the bubble will exceed the surrounding bulk liquid pressure and cause the vapour bubble boundary to expand outward.

2.3.2.2Heat transfer controlled bubble growth

Plesset and Zwick [30] neglected the effect of liquid inertia and focused on the heat transfer controlled bubble growth. Also, a zero order asymptotic solution was formulated for spherical bubble radius. To verify these results, different analytical models and experiments were used by several researchers. Dergarabedian [31] also conducted experiments using water with different degrees of superheat for evaluating the bubble radius. The obtained results agreed well with the solutions up to 6°C of superheat. To analytically determine the vapour bubble growth, the acquired solutions for bubble radius can be coupled with equations given by Rayleigh [27]. Forster and Zuber [32] analyzed the heat diffusion controlled bubble growth for the bubble radius in two-time domains. The first domain (early stage) involves the effect hydrodynamic forces while in the second one (later stage), its effect is negligible. Finally, the complete solution was provided for the entire domain of bubble growth. Birkhoff et al. [33] examined the vapour bubble growth by considering the significance of the boundary layer with the asymptotic phase. The results were computed using a different substance such as Water, Hydrogen, Oxygen, and n-pentane. The studies carried out by Scriven [34] neglected the effect of boundary layer for moderate superheats to determine the solutions to the energy equations. Kosky [35] measured the evolution of a vapour bubble in a high superheated water up to 36°C in the pressure range of 0.5 to 1.2 atm. Florschuetz et al. [36] provided the experimental results at low superheat of 4.9°C by taking ethanol, isopropanol, and water under zero order gravity condition. All these studies verified and confirmed with the results given by Plesset and Zwick [30]. Mikic et al. [37] coupled the both phenomena (Heat transfer and Inertia) of bubble growth with the help of Clausius-Clapeyron equation. Lien [38] confirmed that the bubble growth is governed both by liquid inertia and heat diffusion characteristics at different pressures ranges.

The vapour bubble grows because of the vaporization of the liquid-vapour boundary as the results of heat supplied. This heat is transferred from the superheated surface across the

boundary layer due to conduction. In this case, the vapour temperature inside the bubble is considered to be at the saturated state corresponding to the ambient pressure.
Using energy equation in a spherical coordinate system [27]:

$$\frac{\partial T}{\partial t} + \frac{u \partial T}{\partial r} = \frac{\alpha_L}{r^2} \frac{\partial}{\partial r}\left(r^2 \frac{\partial T}{\partial r}\right) \tag{2.5}$$

where the thermal diffusivity of liquid, $\alpha_L = \frac{K_L}{\rho_L C_{pl}}$ and Bubble Interface Velocity, $u = \frac{dR}{dt}\left(\frac{R}{r}\right)^2$.
Initial and final boundary conditions are:

$$\mathrm{T}\,(\mathrm{r}, \mathrm{u}) = T_\infty;\ T(R, t) = T_{sat}(p_V);\ \mathrm{T}\,(\infty, \mathrm{t}) = T_\infty \tag{2.6}$$

From the energy conservation at the boundary:

$$K_L \frac{\partial T}{\partial r}(R, t) = \rho_G h_{lv} \frac{dR}{dt} \tag{2.7}$$

Approximate solution for Large "Jakob No. (Ja)"

$$R(t) = J_a \sqrt{\frac{12 \alpha_L t}{\pi}} \tag{2.8}$$

where

$$J_a = \frac{\rho_1 C_{pl}(T_\infty - T_{sat})}{\rho_G h_{lv}} \tag{2.9}$$

In nucleate pool boiling conditions, heat transfer enhancement issues are still ambiguous. Interaction of convective heat transfer corresponding to enhanced surfaces has been limited due to their complexity leading to false interpretations. Heat transfer coefficients have been determined using heat flux, saturation pressure, and surface roughness [39].

Zijl et al. [40] investigated the combined effect of inertia and heat transfer controlled growth on a spherical bubble in a superheated condition. General solutions have been derived for growth rate, implosion, and frequency of oscillating vapour bubble.

Kim [41] reviewed and presented the latest experimental and analytical results heat transfer characteristics of a vapour bubble for determining the contribution of each mechanism involving microlayer evaporation, enhanced convection, liquid-vapour interface heat transfer and transient conduction in overall heat transfer.

Lord Rayleigh further improvised the model of Rayleigh-Plesset Equation to determine the size of a spherical vapour bubble. This model can be followed extensively for a vapour bubble in an unbounded medium of liquid. Bongu´e-Boma and Brocato [42] recently described this model through a continuum model along with the microstructure. Also, the size variation of bubbles caused by pressure fluctuations in the medium has been included. Lien [38] considered inertia controlled growth conditions by carrying out experiments with water up to the pressure of 0.01 atm. It was found that under low-pressure conditions, liquid inertia controlled growth dominates. As pressure increases, heat diffusion controlled growth dominates the inertial growth provided by the Rayleigh [27] solution.

2.3.3. Bubble departure diameter

A vapour bubble in contact with the heating surface experiences different forces. The inertia and surface tension force keep the bubble attached to a heated surface, whereas the buoyancy force tends to separate it from the wall in contact. As the bubble size increases, the detachment force dominates and leads to separation from the heated surface.

Using a force balance approach on a vapour bubble, its departure size can be obtained accurately. The departure size of a vapour bubble with cavity radius, rc < 10μm is controlled using the equilibrium condition between the inertia and buoyant forces. The rate of growth of a vapour bubble reduces with increase in the cavity size, making the inertial force insignificant and unimportant. Fritz [43] proposed the relationship for determining the vapour bubble diameter by equating the surface tension and buoyancy force that is given by the following equation:

$$d_o = 0.208\theta \left[\frac{\sigma}{g(\rho_L - \rho_G)}\right]^{\frac{1}{2}} \qquad (2.10)$$

where θ is the measure of bubble contact angle.

An enhanced model related to bubble departure diameter was developed by Colombo and Fairweather [44] during the condition of flow boiling. In this model, the equilibrium between the forces acting on a vapour bubble has been considered for a single nucleation site. The solution to the equation governing the bubble growth was successfully confirmed by the experimental data.

Helden et al. [45] investigated the importance of forces and gravity during the bubble detachment from the artificial nucleation sites on a vertical surface at surrounding pressure and 1g conditions.

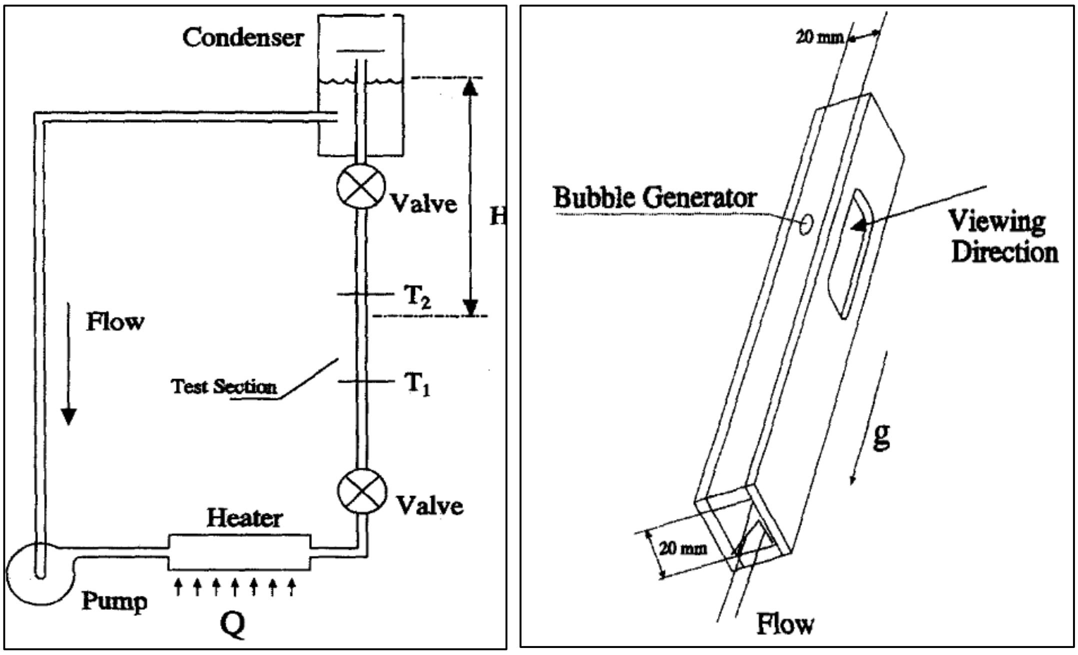

Figure 2.8 (a) Test loop with main components (b) Test section details [45]

The experiment (Fig. (2.8)) revealed the variation in the lift direction between vapour and LN2 bubbles. The obtained results also showed that there is a decrease in detachment radius as the velocity of the bulk liquid increases.

2.3.4. Bubble release / departure frequency

The departure frequency, 'f' of the vapour bubble depends on the

a) Growth time, 't_g' and
b) Waiting time, 't_w'

Efforts to determine the frequency by predicting the growth and waiting period were seldom recognized due to following reasons

(a) This method didn't contemplate the evaporation occurring from the base as well as the bubble surface;

(b) Effect of cavity size, liquid flow variability, and heat transfer on the growth and waiting period; and

(c) Frequent changes in the size of the growing vapour bubble [46].

The departure frequency is influenced by the changes in the departure diameter and is dependent on the cavity size. However, the magnitude of frequency is constant for any single cavity under consideration. The correlation between the frequency and diameter, ‘do’ at the departure point is given as ${fd_o}^n = Const$. The value of ‘n’ as recommended by Ivey [47] is ½ for the heat transfer and 2 for the inertia controlled growth. Malenkov [48] developed another relationship for the departure frequency which is given by:

$$fd_0 = \frac{V_b}{\pi\left(1 - \frac{1}{1 + V_b \rho_G h_{lv}/q''}\right)} \tag{2.11}$$

where V_b refers to the departure velocity that can be estimated from the below relation:

$$V_b = \sqrt{\frac{d_o g(\rho_L - \rho_G)}{2(\rho_L + \rho_G)} + \frac{2\sigma}{d_0(\rho_L + \rho_G)}} \tag{2.12}$$

Quite a lot of works have been attempted for investigating the current relationships in conditions of forced convective subcooled boiling. Situ et al. [49] studied the departure frequency using experimental techniques in a vertical subcooled flow boiling process. As per the developed correlation, it was found that the existing results matched suitably with the data corresponding to low superheat conditions.

In heat transfer modeling for high heat flux boiling, the departure frequency in case of coalesced bubble is also a significant factor under consideration. Though these results have been obtained for ethane, water, and methanol, but investigation of cryogenic liquids are comparatively rare. Jin et al. [50] quantified the departure frequency in LN2 over the plane surface for analyzing its influence on parameters such as heat flux, material, and diameter. McFadden and Grassmann [51] also studied the nucleate boiling of liquid nitrogen and presented a new correlation concerning the frequency and diameter from the dimensional analysis, viz. ${fd_0}^{1/3} = Const$.

2.3.5. Boiling phenomenon

Boiling is a very complex but very common natural phenomenon involving nucleation, growth and intricate dynamics of vapour bubbles. There are generally two types of boiling phenomenon occurring due to heat transfer

a) Nucleate boiling or Pool boiling
b) Flow boiling

Nucleate boiling occurs when the heat transfer is taking place to the liquid in no flow condition. Sakashita and Kumada [52] considered the effect of superheat, nucleation site density, heat flux, and physical properties and proposed new correlation. The different boiling curves were also drawn at saturation boiling conditions. Theofanous et. al [53] conducted an experiment (Fig. (2.9)) to capture the phenomenon of pool boiling under high heat flux.

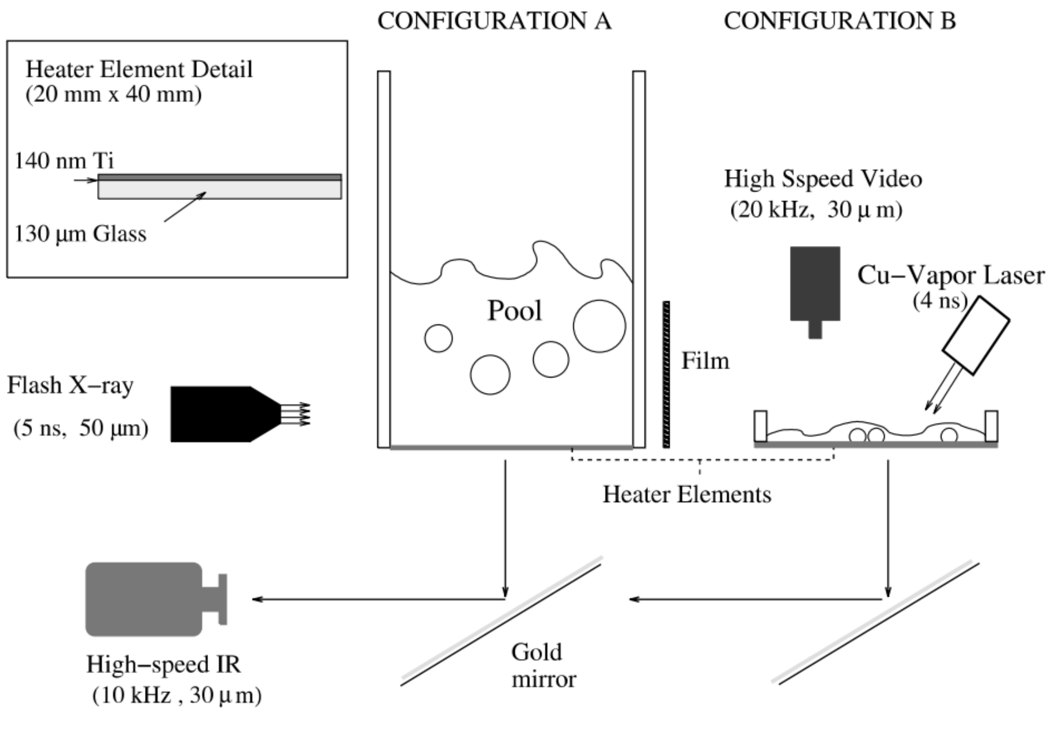

Figure 2.9 Experimental set up for nucleate boiling study [53]

The effect of nucleation site density (NSD), bubble formation, growth was examined. The NSD was different in the fresh heater element and the aged heater element. The NSD was increasing as per the aging of the heater element. The nucleate boiling phenomenon is not common in the industrial application hence a very less work was done.

Flow boiling occurs when the heat transfer is taking place with the forced convection flow which is truly complicated. It depends on numerous parameters i.e. thermo-physical properties of the liquid, channel geometry, interface characteristics, operating conditions, etc. [54]. Despite of its complexity flow boiling is being used in a large number of engineering applications (i.e. steam tube boilers, refrigeration industry, air separation and cryogenics industry, etc.) due to its ability to carry large amount of heat through a limited volume of liquid. Physical characteristics of the flow boiling strongly depend on the size of the channel and equations developed for the conventional channel becomes inapplicable for micro size channel [55]. The flow boiling can be in the sub-cooled flow. The bubble behaviour was observed from the partially developed flow to the fully developed flow by Prodanovic et. al [56]. The bubble in the horizontal surface slides in the flowing direction up to a distance of 1-2 diameters before collapsing.

2.3.6. Forces on the departing bubble

Various forces acts on the departing bubble vertically upward and the downward direction in the case of nucleate boiling.

a) Buoyancy force(Upward)
b) Shear lift force (Upward)
c) Contact pressure force (Upward)
d) Drag force (Downward)
e) Surface tension force (Downward)

All the responsible forces for the bubble detachment from the heating surface, are shown in Fig. (2.10).

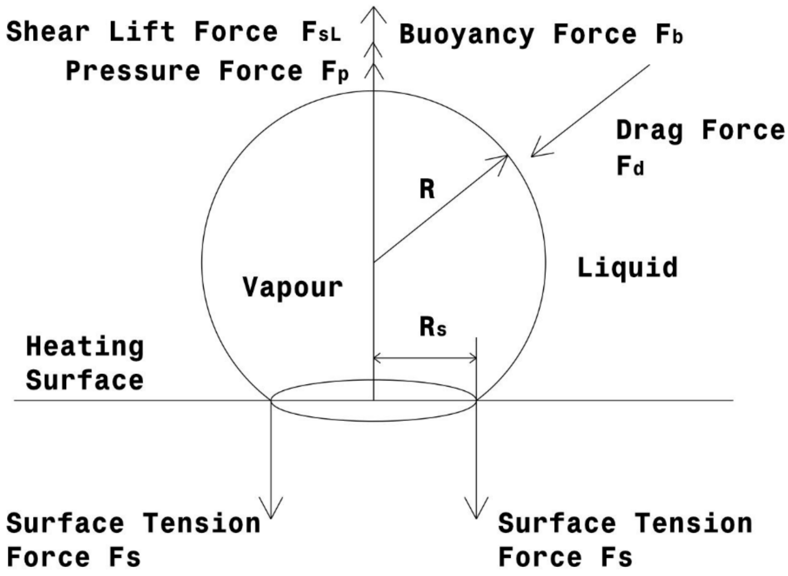

Figure 2.10 Forces on a single spherical bubble

The resultant force acting on a spherical bubble is a vector sum of the forces acting in vertically upward and downward direction. Therefore, the resultant vertical force acting on a single spherical bubble and can be written as:

$$\sum F = F_{b\uparrow} + F_{sL\uparrow} + F_{cp\uparrow} + F_{d\downarrow} + F_{sy\downarrow} \qquad (2.13)$$

↑ shows the upward direction of force while ↓ shows downward direction.

This resultant force, 'F' is responsible for the upward momentum gained by the bubble at the time of departure.

The buoyancy force, 'F_b' acting on a spherical vapour bubble [57] can be calculated using the Archimedes principle and can be estimated by:

$$F_b = \frac{4}{3}\pi R^3(\rho_L - \rho_G)g \qquad (2.14)$$

The equation for the shear lift force, 'F_{sL}' on a vapour bubble [58] is given by:

$$F_{sL} = \frac{1}{2}C_L\rho_L\Delta U^2\pi R^2 \qquad (2.15)$$

where ΔU refers to the velocity difference between the bubble center point and the liquid phase and C_L refers to the shear lift coefficient which is given by:

$$C_L = 3.877 G_s^{1/2} \left[Re^{-m/2} + \left(0.344 G_s^{1/2}\right)^m \right]^{1/m}, m = 4 \qquad (2.16)$$

where $G_{s=} \left|\frac{dU}{dy}\right| \frac{R}{U}$, $Re = \frac{\rho_L.\Delta U.d_o}{\mu_L}$, μ_L corresponds to the dynamic viscosity of the liquid.

As the force acting on the bubble depends on the local flow structure and the bubble sizes, the bubbly flow state is quite complex. Therefore, a more detailed modelling is required to study the two-phase flows. Through experimental and theoretical studies on a single bubble, numerous correlations have been developed that describe the bubble forces. Lucas et al. [59] provided the sets of bubble forces in vertical pipe flow models for poly-disperse flows from the experimental database. It was found that the different models for the bubble forces considering Favre averaged turbulent dispersion force, deformation force, and Tomiyama lift, as well as wall force, provides the best agreement with the experimental data.

Studies were conducted to analyze the lift behaviour between a solid particle and a single bubble. However, the behaviour of a solid particle is quite different from that of vapour bubble, the reason for this difference in lift generation mechanism was not explained. Kurose et al. [60] examined the fluid shear effects for a high particle Reynolds number during the lift of a spherical bubble using a 3-D numerical simulation. The study also intended to explain the variations in the mechanism of lift generation between a bubble and a solid particle.

The contact pressure force, 'Fcp' accounts for the pressure acting on a solid surface rather than the bubble surface surrounded by the liquid. This force can be evaluated as [61]:

$$F_{cp} = \frac{\pi {d_w}^2}{4} \frac{2\sigma}{R_r} \qquad (2.17)$$

where Rr is the curvature radius. For any vapour bubble, this curvature can be accounted by considering the point x = 0 on the contact surface. The value of the curvature radius [61] can be taken as 5 times the radius of the bubble, i.e. Rr ~ 5R.

The drag force, 'Fd' can be defined as the resistance offered by the surrounding liquid in the opposite direction to the motion of the spherical vapour bubble. It can be approximated as [61]:

$$F_d = -\frac{1}{2} C_D \rho_L \Delta U^2 \pi R^2 \tag{2.18}$$

where C_D is the drag coefficient, which can be approximated as,

$$C_D = \frac{24}{Re}\left(1 + \frac{3}{8} Re\right) \tag{2.19}$$

The drag force is quite small in the theoretical modelling by assuming inviscid liquids [62]. Sugioka and Tsukada [63] numerically examined a spherical bubble near the wall surface using a 3-D DNS dependent Marker and Cell (MAC) technique for measuring the lift and drag forces. The results exhibited the rise in the drag force due to the presence of wall surface. Dijkhuizen et al. [64] also investigated the performance of a bubble expanding into pure still water using the DNS techniques. The drag coefficient for a bubble increases with the decrease in the distance between the wall surface and the vapour bubble.

The surface tension force, 'Fsy' acts over the contact line of the triple interface. Surface tension force in the y-direction can be calculated as [61]:

$$F_{sy} = -d_w \sigma \frac{\pi}{(\alpha - \beta)} [\cos\beta - \cos\alpha] \tag{2.20}$$

In this equation, α and β refers to the advancing and receding contact angles respectively, and dw refers to the bubble contact diameter. As suitable models for determining these parameters are comparatively less in the literature; therefore it casts major doubt on the accuracy of the present model [65]. Klausner et al. [61] recommended α = π/4 and β = π/5 from their measurements in R113 for 0.09 mm dw. However, Yun et al. [66] considered a constant ratio of contact diameter to bubble diameter, dw = do/15. Sugrue [67] provided the measurements of contact angles mainly for water, i.e. 90.63° as the advancing angle and 8.03° as the receding contact angle. Moreover, a small contact diameter to bubble diameter ratio was reported to give reasonably good agreement with data [65].

G.H. Yeoh et al. [68] performed the experiment to formulate a model considering the appropriate force balances acting on a bubble under subcooled conditions. The set-up consisted of a vertical concentric annulus with an inner heating rod. Fig. (2.11) shows the schematic drawing of the test channel.

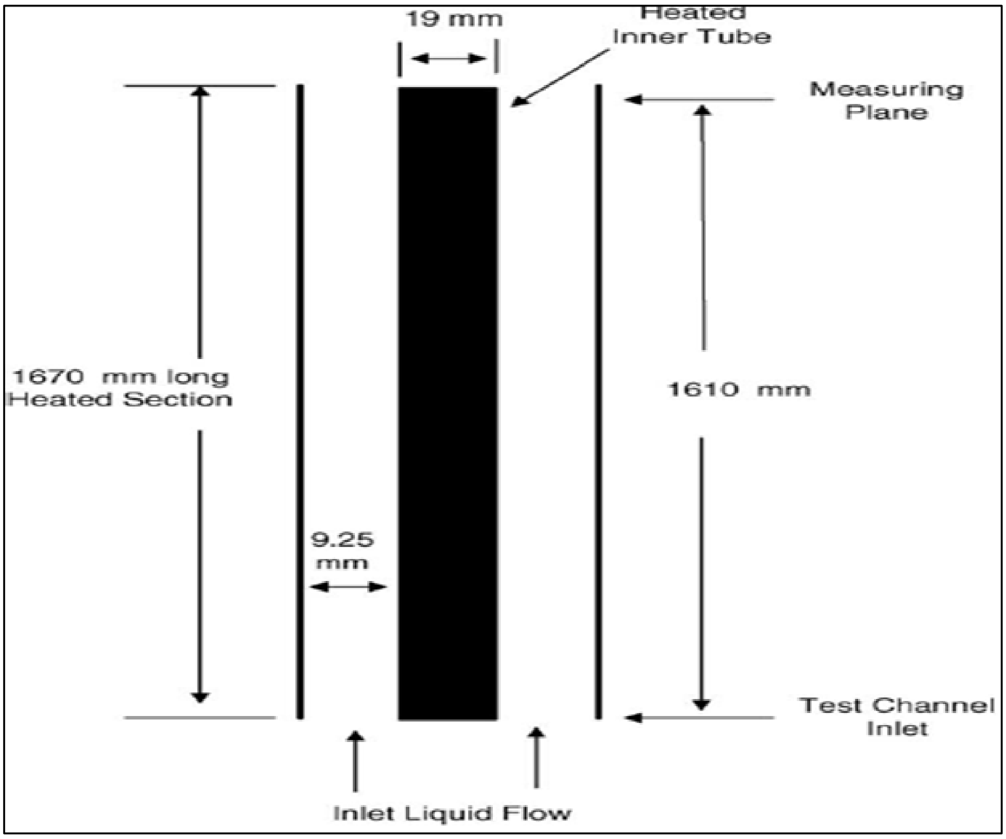

Figure 2.11 Schematic diagram of the test channel [68]

On applying the experimental conditions, the magnitude of respective forces acting on a single bubble in x and y directions are Fsx $\sim 1.13\times10^{-5}$ N; Fdux $\sim 9.39\times10^{-6}$ N; FsL $\sim 8.12\times10^{-5}$ N; Fh $\sim 2.69\times10^{-7}$ N; Fcp $\sim 1.64\times10^{-7}$ N and those in the y-direction are: Fsy $\sim 8.04\times10^{-7}$ N; Fduy $\sim 1.66\times10^{-6}$ N; Fqs $\sim 1.34\times10^{-4}$ N; and Fb $\sim 3.51\times10^{-7}$ N [18].

2.4. Bubble-induced vibration

Bubble motion provides the basis to understand the induced vibration. During the boiling process, the random movements of liquid and generated vapour bubbles lead to instability in the system. When these generated vapour bubbles interact with the surface of the system, induced vibration phenomenon occurs. Induced Vibrations are undesirable in the systems as they influence system safety and control problems affecting the standard process and limiting the operational parameters.

There are two major causes of mechanical vibrations:

a) Subcooled Boiling-Induced Vibration (SBIV)
b) Flow Induced Vibration (FIV).

Researchers have focussed mainly on the effects of FIV's rather than the SBIV, which also contributes significantly to the vibration phenomena.

2.4.1. Subcooled boiling induced vibration (SBIV)

Experimental investigation on SBIV was carried out by the authors [69]–[72] considering different cylindrical configuration, such as mini tubes, cylinders, heating rods, etc. It was reported that both the evolution and implosion of a vapour bubble are very important in distinguishing the key characteristics of subcooled boiling system. Hence, the bubble formation and collapse can affect the excitation force resulting in induced vibration. Nematollahi et al. [71] also concluded that the SBIV vibrations were so strong that it can be measured when there was a flow induced vibrations also. The experimental results show that the rapid growth and collapse of the bubbles generates force and SBIV depend on these forces. Moreover, it was also observed that bubble growth and collapse depends on the sub-cooling temperatures [70]. At higher sub-cooling temperatures, the bubble growth and collapse takes place very rapidly near the heated surface due to less lifetime of the bubble that may result in the higher pressure pulses near the heating surfaces. The force acting at the nucleation site present on the heated wall during the evolution phase is given by [72]:

$$F = \dot{m}\bar{V} = \frac{16\pi^2}{3A_0\,RT}(3p_0R + 4\sigma)R^3\left(\frac{dR}{dt}\right)^2 \qquad (2.21)$$

where, p_0 is the pressure outside the bubble, A_0 corresponds to the cavity surface area hence cavity opening radius can be taken as initial bubble radius, $\bar{R}$ is vapor gas constant, and T is its temperature.

The average force acting on the heated surface is calculated by integrating Eq. (2.21),

$$\bar{F} = \frac{16\pi^2}{3A_0\,\bar{R}T}\left(\frac{dR}{dt}\right)^2_{ave}\left[0.6p_0\frac{(R_{max}^5 - R_0^5)}{(R_{max} - R_0)} + \sigma\frac{(R_{max}^4 - R_0^4)}{(R_{max} - R_0)}\right] \qquad (2.22)$$

where R_o is the initial bubble radius and R_{max} refers to the maximum bubble radius.

The experimental setup is shown in Fig. (2.12) [72].

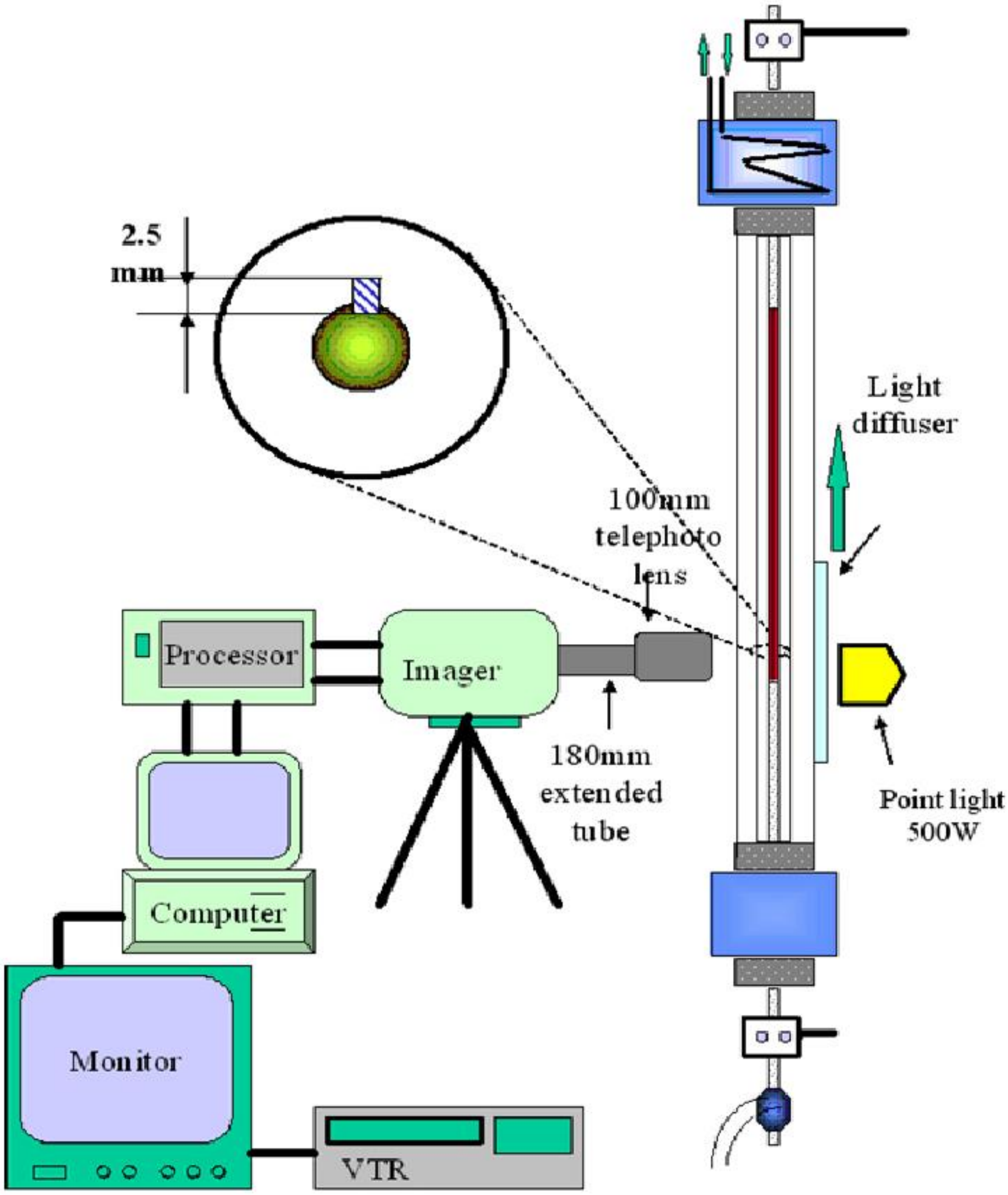

Figure 2.12 Experimental setup to capture high-speed images of bubble [72]

The average force exerted is in the order of 10^{-4} N for water at 1 bar pressure and temperature of 20°C with the surface tension of 0.074 N/m [69]. In this experiment, the relationship between calculated and actual force has not been attempted.

Collier and Thome [28] have expressed the statement related on the SBIV in the literature where it is indicated that “At high loading heat fluxes, the onset of subcooled boiling is encountered at a high degree of sub-cooling, and the vapour bubbles may grow and collapse. However, these processes are sometimes accompanied by the noise and vibration of the heating surface".

In many cases, the sub-cooled liquid boiling is accompanied by the High-Frequency pressure Oscillations (HFO). The frequency of these oscillations is almost in the range of the acoustic frequency. Hence, due to the coincidence of HFO and acoustic frequencies, the thermoacoustic phenomenon occurs. Smirnov et al. [73] correlated the subcooled boiling with the thermoacoustic phenomenon for the liquid flowing in the tube. The pressure oscillation amplitude can be found out as

$$P(x) = \frac{\rho \bar{C} V_{max}\, wZp}{Ks} . F(KX, KL \dots) \qquad (2.23)$$

where ρ = density of the fluid, $\bar{C}$ = pressure wave propagation velocity, V_{max} = maximum vapor bubble volume, w= liquid flow rate, Z= number of vaporization centers, p=heated section perimeter, K=wave number, s=cross-sectional channel area, $F\ (KX, KL \dots)$ =combination of periodic functions.

Thermoacoustic phenomena has also been visualized in the case of film boiling. As superfluid liquid helium (He II) is being extensively utilized in space cryogenic applications such as detector and magnetic cooling systems, the optimum cooling performance output is of prime importance. However, in cases of noisy film boiling, the cooling capability of He II depreciates due to the presence of mechanical and thermal disturbances [74]. To avoid the conditions of induced vibrations due to noisy film boiling, the bath temperature needs to be decreased. As a result, the hydrostatic pressure required for noisy film boiling also diminishes [75]. In addition, the coefficient of heat transfer obtained in the case of noisy film boiling becomes much less as compared to silent film boiling thereby decreasing the cooling performance significantly. Despite various studies conducted on the cooling effects of film boiling [76], [77] several aspects concerning heat flux, bath temperature etc. still needs to be reviewed in detail.

Zhang et al. [74] evaluated the effect of heat flux, bath temperature and heater size for determining the mechanism associated with noisy film boiling. In addition, a thorough study was also carried out for computing the temperature and pressure fluctuations related to the mechanism. Planar heater was utilized for boiling the He II and pressure sensors were deployed to measure the pressure oscillations. It was observed that as the heating duration of He II is increased beyond 1 second at a constant heat flux of 10 W/cm2, the saturation boiling changes to noisy film boiling. This stage is accompanied by the frequent formation of large vapor bubbles which subsequently collapses on the surface of heater leading to large mechanical vibrations and acoustic noise. Zhang et al. [74] provided the evidence that the bubbles expand and collapse repeatedly causing various temperature peaks which make the calibration superconductor temperature sensor quite challenging.

Though the subcooled boiling flow is extensively utilized in systems such as nuclear reactors and steam generators, it is necessary to understand the SBIV. Eisinger et al. [78] formulated the criteria for development of acoustic vibration in steam generators as well as heat exchanger tube banks. Thus, thermos-acoustics has become one of the vital phenomena in the area of subcooled boiling and provides the benchmark for identifying the induced vibration. However, results concerning SBIV are still in abeyance that needs to be analyzed in detail in the near future.

2.4.2. Flow-induced vibration (FIV)

Robert Blevins in 1977 transcribed his first book on the area of Flow-Induced Vibration (FIV). This term became popular after it was used in the textbook title. The studies of Blevins centered on the eigen modes and excitation frequency associated with FIV for structural and hydrodynamic systems respectively [79]. The work done on FIV also provided the direction to look upon the issue related to vibration and noise problems. FIV obstructs the smooth plant operation and in severe cases can lead to significant maintenance and costly losses in productivity. Different kind of vibration issues has been encountered in nuclear power stations that include reactor, associated piping, steam generators, heat exchangers and other such additional equipment involving secondary piping and in-core instrument tubes [80].

Study of FIV in heat exchangers have also become a major area of focus for several researchers. Heat exchangers are a simple engineering device with no moving components. Investigations have been carried out concerning various mechanisms (Surrounding excitation, resonance, Vortex Shedding, Turbulence buffeting, Fluid instability, Multi-phase buffeting, and Hydraulic transients) causing vibration and noise along with mechanical integrity in heat exchanger bundle tubes [81]. However, fluid instability is a very critical source of FIV in heat exchangers. To prevent tube failures in heat exchangers, two phase FIV excitation forces must be examined in detail. Various researchers obtained the different sets of experimental results concerning two-phase flow vibration considering different flow patterns or regimes [82]–[88]. Nevertheless, various effects such as viscosity, density ratio, and surface tension have been neglected. Pettigrew and Knowles [89] conducted the experiment to evaluate the dampening effect in a heat exchanger pipe in two-phase flow condition with a void fraction of about 25%. It was noticed that the vibration effect on the unexpected turbulence in the two-phase mixture is highly dependent on the surface tension.

In the case of two-phase flow, FIV mainly depends on the void fraction, flow rate, direction of flow and velocity [89]–[92]. The principal factor that affects the vibration phenomena is a void fraction. Experimental and analytical studies confirmed that any fluctuation in void fraction can lead to significant variation in the mode shapes and frequency. Based on the flow direction, FIV can be categorized as internal, external, cross and axial. The parameters needed to evaluate the two-phase FIV are homogeneous void fraction (ε), pitch velocity (U_P) and free stream velocity (U_∞) and can be expressed as [82]:

$$\alpha = \frac{Q_a}{Q_a + Q_w}; U_\infty = \frac{Q_a + Q_w}{A_\infty}; U_P = U_\infty \left(\frac{P}{P - D}\right) \qquad (2.24)$$

where Q_a is the volumetric flow rate of air and Q_w is the volumetric flow rate of water, A_∞ refers to the free flow area, P corresponds to the center distance between the tubes (pitch) and D is the tube diameter.

Zhang et al. [93] confirmed that the variation in the void fraction plays a significant role in defining the vibration spectrum. The results revealed that the effect of void faction was dominant in the low-frequency range, i.e. 4 Hz to 11 Hz, with pitch velocity of 5 m/s and void fraction of 80%. To analyze the dynamic vibration characteristics due to force excitation in a rotated cylinder bundle of the two-phase flow, semi-analytical mathematical models were formulated [94]. It was found that the momentum flux fluctuations are linked to the drag forces in the flow regime between the cylinders.

Zhang et al. [94] developed the semi-analytical models for correlating and recognizing the characteristics of excitation forces in response to the dynamic vibration characteristics in a rotated cylinder bundle of the two-phase flow. It was found that in the main flow region in-between the two cylinders, the quasi-steady drag forces are linked with the momentum flux fluctuations. Miwa et al. [95] in his critical reviews on the FIV mentioned about the trends in the two-phase internal flows and found out that the momentum flux contribution was very significant in the low-frequency zone that is less than 50 Hz. Also, it has been reported that the natural frequency corresponding to the FIV experiment is required to be greater than 50 Hz to avoid the resonance. Liu [91] revealed with the increase in gas velocity from the bubbly to slug flow, the peak frequency of void fraction, momentum flux, and force fluctuations become maximum corresponding to the liquid velocity. The primary assumption considered for this study was based on the smooth flow of liquid-vapor mixture inside the pipe.

The excitation mechanism of two-phase flow induced vibration over a straight horizontal pipe has been investigated by Hara [90]. The experimental study disclosed a significant relation between the piping's system fundamental natural frequency and dominant frequency of water slug arrival in the two-phase flow with ratios of ½, 1/1, and 3/2 where intense vibration occurs. The primary focus of the early research was to determine the force intensity and the associated frequency level in different two-phase flow systems. Takashi [96] analyzed the motion of one phase with respect to the other phases in a dispersed two-phase flow system by considering the drag, gravitational forces, the effect of pressure gradient due to shear stresses and using a similar hypothesis based on the Reynolds number and drag coefficient. Recently, C. Charreton et al. [97] experimented to find out the damping effects of the two-phase flow, which is very crucial parameter in the study of the FIV. The simple analytical mode was also derived to get information about the physical dissipative mechanism. It was concluded that two-phase flow damping can be treated as viscous damping and it depends on the void fraction.

Min An et al. [98] investigated vibrations induced due to the flow boiling of internal vapor-liquid-solid phase through a graphite tube of the evaporator. It was concluded that addition of solid particle in the two-phase flow boiling process increases vibration greatly. The vibrations in the graphite tube can be decomposed into three frequency regimes based on the phenomenon. The frequency regime from 0-500 Hz, 500-3000 Hz, and 3000-9000 Hz can be categorized as macro-scale, meso-scale and micro scale sub signal respectively. These three frequency regimes exist due to liquid flow, vapor bubble behavior and collisions among the solid particle and between solid particle and the tube wall.

Study of FIV in heat exchangers have also become a major area of focus for several researchers. Heat exchangers are a simple engineering device with no moving components. Investigations have been carried out concerning various mechanisms (Surrounding excitation, resonance, Vortex Shedding, Turbulence buffeting, Fluid instability, Multi-phase buffeting, and Hydraulic transients) causing vibration and noise along with mechanical integrity in heat exchanger bundle tubes [81]. However, fluid instability is a very critical source of FIV in heat exchangers. To prevent tube failures in heat exchangers, two phase FIV excitation forces must be examined in detail. Various researchers obtained the different sets of experimental results concerning two-phase flow vibration considering different flow patterns or regimes [82],[84],[93]. Nevertheless, various effects such as viscosity, density ratio, and surface tension have been neglected. Pettigrew and Knowles [89] conducted the experiment to evaluate the dampening effect in a heat exchanger pipe in two-phase flow condition with a void fraction of about 25%. It was noticed that the vibration effect on the unexpected turbulence in the two-phase mixture is highly dependent on the surface tension.

Vortex Shedding is also a significant mechanism for FIV, which arises due to various forces that act on a tube (circular cylinders) during shell-side cross flows of heat exchangers [81]. These forces cause external pressure fluctuations or vibrations resulting in Vortex-induced vibration (VIV). The condition of Synchronization in VIV is reached when the body's natural frequency is close to vortex formation frequency, and the response amplitude increases significantly with the phase transition in-cylinder motion and pressure fluctuation [99]. As the Reynolds number increases to a threshold value, there is a loss in flow stability. Eventually, the vortices coming off during wake involve the well-known phenomenon of Von Karman vortex street [100]. The Strouhal number is mostly associated with reduced frequency of VIV. It varies in accordance with the value of the Reynolds number [101]. Lienhard [102] experimentally determined the relationship between the Strouhal and Reynolds number with an accuracy of 5 to 10% using isolated static cylinders as shown in Fig. (2.13).

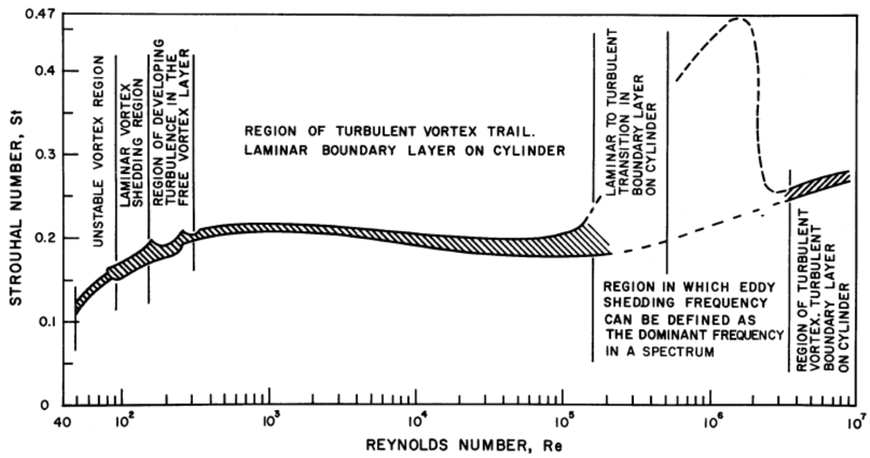

Figure 2.13 Envelop of Strouhal-Reynolds number relationship for circular cylinders [102]

Tube arrays may also be subjected to self-induced vibrations during cross flows leading to fluid elastic instabilities. To determine the critical flow velocity needed to actuate the fluid elastic instability, Robert [103], [104] formulated the criteria for the proposed mechanism. It was found that the instability can happen provided that:

$$\frac{U}{f_n D} > 12 \tag{2.25}$$

where U is the flow velocity of the fluid, D is tube's natural frequency and D is the outer diameter of the tube array.

Moreover, the flow pattern can seriously affect the fluid elastic instability of the system. The use of turbulators can also cause instabilities if its axis becomes normal to the tube's axis [105]. Therefore, it is very much necessary to have the information regarding fluid flows and its possible interaction with the structure/component.

2.5. Summary

Different works have been carried on the various aspects related to Boiling Heat transfer, Bubble growth and nucleation, Bubble motion and its dynamics involving departure diameter, frequency, and acting forces.

Fully quantitative predictive models are still under development since they require information about heat transfer mechanisms derived from theoretical models and from detailed experiments on bubble dynamics.

The bubble shape or bubble departure diameter has been considered for describing the dynamic process of bubble growth. The distinct feature of bubble dynamics is that contact angle deviates from the static value due to the rapidity of the growth.

Investigation of forces on bubbles growing under subcooled flow boiling provides a basis for developing models to predict forces under pseudo-static conditions and these forces can be suitably modified for more complex analyses of bubble growth and departure. The force on the bubbles is totally different from the forces due to bubbles but as per literature review, the forces due to bubbles will be in the order of 10^{-5} to 10^{-7} N.

2.6. Gaps identified from literature survey

No experiment or theoretical investigation has been performed on the vibration and noise due to bubbles of the air-water mixture or liquid nitrogen. Hence no data or literature is available on the bubble induced vibration to design the cryopump for the gravitational wave astronomy. Hence this is a new most important area of investigation for the astronomy point of view.

Bubble motion parameters are not formulated which provides the base for the bubble induced vibrations in the nucleate / pool boiling.

Theoretical investigation for the bubble induced vibrations and its different modes are also not available. Hence it is very challenging to find out through different generated codes, for liquid nitrogen fluid.

There are no such available works done in this regard, only the case study of the LIGO report has been described.

2.7. Closing remarks

The detailed literature review on bubble dynamics, induced vibration due to sub-cooled and flow has been discussed in this Chapter. Out of the literature survey, research gaps have been identified.

Therefore, an attempt is made to obtain the generalized formulation for the bubble induced vibration and noise in case of nucleate or pool boiling. The bubble dynamics and bubble motion parameters are also to be developed.

Chapter 3

Bubble Dynamics

The dynamics part is intended to supplement the extensive literature on bubble migrations and its effects. The bubble departure diameter is one of the important parameter, which plays a key role in the bubble dynamics. The bubble dynamics shows the various forces acting on the bubble during the bubble departure. The net vertical force will tend to lift the bubble from the heated surface. After departing from the surface the bubble moves in the liquid medium. During the movement, only certain forces will dominate the motion of the bubble. These forces will decide the displacement, velocity and the acceleration of the bubble considering the bubble as sphere. For a sphereiod bubble, the ratio of displaced liquid mass is twice the entrained mass. Therefore, the initial bubble acceleration (independent of size) will be 2g. The bubble is striking on the surface with certain velocity and acceleration. This will exert an impact force on the surface. This impact force is formulated in terms of semi-sinusoidal function and maximum force is evaluated.

3.1. Bubble departure models

The bubble nucleation takes place in any liquid from the nucleation sites present on the surface due to heat transfer. After the nucleation stage, the bubble growth process begins and continues to grow further to the point of detachment from the heated surface. Various properties of the liquid like inertia, surface tension, molecular diffusion, and viscosity are crucial for determining the growth rate. The diameter attained by bubble at the time of detachment from surface is called as bubble departure diameter.

Bubble diameter (d_b) has been investigated over the last few decades. Experimental relationships have mostly been developed from empirical data as a function of the non-dimensional numbers, bubble contact angle, or other thermo-hydraulic parameters. Moreover, systematic models have been formulated from the force balance equation that prescribes the bubble's departure from the heated surface. The various models are applicable to the water and liquid nitrogen fluid as given.

3.1.1. W. Fritz model

In 1935, Fritz [43] predicted the bubble departure diameter (d_b) by equating the buoyancy and adhesive force.

$$d_b = 0.208\theta \left[\frac{\sigma}{g(\rho_L - \rho_G)}\right]^{\frac{1}{2}} \tag{3.1}$$

where θ is the contact angle, ρ_L and ρ_G are the density of liquid and gas phase of the fluid respectively, σ is the surface tension of the liquid.

This model is one of the most reliable models for the prediction of bubble departure diameter for the boiling of pure liquids and also liquid mixtures. This model is independent from the heat transfer and considers only the liquid properties.

3.1.2. N. Zuber model

Zuber [106] derived a correlation of the bubble departure diameter by assuming that bubble growth occurs in a superheated and thin thermal layer near the surface.

$$d_b = \left[\frac{6\sigma}{g(\rho_L - \rho_G)}\frac{k\Delta T}{q}\right]^{1/3} \tag{3.2}$$

where k is the thermal conductivity of liquid, q is the heat flux supplied to the liquid for the nucleate boiling, ΔT is the difference between the wall temperature and the saturation temperature of the liquid i.e. $T_w - T_{sat}$.

3.1.3. Cole and Shulman model

Cole and Shulman [107] reported that the bubble departure diameter is proportional to the inverse of the absolute pressure. One year later, Cole [108] summarized the existing studies on the bubble departure diameter and departure frequency and proposed a correlation.

$$d_b = 0.04Ja\sqrt{\frac{2\sigma}{g(\rho_L - \rho_G)}} \tag{3.3}$$

$$J_a = \frac{\rho_L C_{pl} T_{sat}}{\rho_G h_{lv}} \tag{3.4}$$

where J_a is the non dimensional Jakob number, C_{pl} *and* h_{lv} are the specific heat and the latent heat of liquid respectively.

In 1969, Cole and Rohsenow [109] proposed much better correlations for the bubble diameter at departure:

$$d_b = 1.5 \times 10^{-4}\sqrt{\frac{2\sigma}{g(\rho_L - \rho_G)}}(Ja)^{\frac{5}{4}} \tag{3.5}$$

Cole and Rohsenow also proposed the relation for the liquid nitrogen fluid

$$d_b = 1.31\sqrt{\frac{\sigma}{g(\rho_L - \rho_G)}} \tag{3.6}$$

The relation is just like as given by the Fritz. It does not involve any heat criteria.

3.1.4. Ruckenstein model

Ruckenstein [110] modified Fritz model by involving the heat flux through the surface temperature. The surface temperature is a part of the Jakob number.

$$d_b = \left[\frac{3\pi^2\rho_L^2\alpha_L^2 g^{0.5}(\rho_L - \rho_G)^{0.5}}{\sigma^{1.5}}\right]Ja^{\frac{4}{3}}\sqrt{\frac{2\sigma}{g(\rho_L - \rho_G)}} \tag{3.7}$$

where α_L is the thermal diffisivity of the liquid.

3.1.5. Van Stralen and Zijl model

Van Stralen and Zijl [111] proposed an empirical model for nucleate boiling by considering bubble growth mechanisms. This model includes the Jakob number and thermal diffusivity of the solution.

$$d_b = 2.63\left[\frac{Ja^2\alpha_L^2}{g}\right]^{\frac{1}{3}}\left[1+\left(\frac{2\pi}{3Ja}\right)^{\frac{1}{2}}\right]^{\frac{1}{4}} \tag{3.8}$$

3.1.6. Stephan Wenzel model

According to Stephan Wenzel [112] has modified the Fritz model by involving three dimensionless numbers (Jakob, Prandtl, and Archimedes).

$$d_b = 0.25\left[1+\left(\frac{Ja}{Pr}\right)^2\frac{100000}{Ar}\right]^{0.5}\sqrt{\frac{2\sigma}{g(\rho_L-\rho_G)}} \tag{3.9}$$

$$Ar = \frac{g\rho_L\Delta\rho}{\mu_L^2}\left(\frac{\sigma}{g\Delta\rho}\right)^{\frac{3}{2}} \tag{3.10}$$

$$Pr = \frac{\mu C_{pl}}{k} \tag{3.11}$$

where Ar is the Archimedes, Pr is the Prandtl number, $\Delta\rho$ is the difference between the densities difference between liquid and gas, μ_L is the dynamic viscosity of the liquid.

3.1.7. Jeongbae Kim and Moo Hwan Kim model

Kim et al. [113] obtained the relation of bubble departure diameter of bubbles during nucleate pool boiling under a range of conditions, including constant heat flux and temperature pool conditions, subcooled, saturated and superheated thermodynamic conditions, and atmospheric and sub-atmospheric pressure conditions. The relation was proposed using the relationship between the Jakob and Bond Number

$$Bo^{1/2} = 0.1649Ja^{0.7} \tag{3.12}$$

where Bo is the non dimensional Bond number and can be expressed as

$$B_o = \frac{g(\rho_L-\rho_G)(d_b)^2}{\sigma} \tag{3.13}$$

The equation for the bubble departure diameter can be calculated as

$$d_b = \frac{0.1649 Ja^{0.7}}{\sqrt{\frac{(\rho_L - \rho_G)}{\sigma}}} \tag{3.14}$$

3.1.8. Han Choon Lee et al. model

Han Choon Lee et al. [114] estimated the bubble diameter by relating it to pressure difference condition using static equilibrium and expressed the diameter as:

$$d_b = 8437.5 \frac{\alpha_L^2 \rho_L}{\sigma} Ja^2 \tag{3.15}$$

After comparing the various models of bubble departure diameter, it can be concluded that the best suitable model is given by W. Fritz. This model gives the best result for the pure liquid. Though Stephan Wenzal improved the Fritz's model by involving the dimensionless factors, this model is best suited for the liquid mixtures. Moreover, other models mostly consider the heat transfer phenomenon in the bubble growth.

For liquid nitrogen, Jeongbae Kim and Moo Hwan Kim [113] provided the correlation for determining the bubble departure diameter, and it was proposed by the following equation;

$$d_b = \frac{0.1649 Ja^{0.7}}{\sqrt{\frac{(\rho_L - \rho_G)}{\sigma}}} \tag{3.16}$$

where

$$Ja = \frac{\rho_1 C_{pl}(T_w - T_{sat})}{\rho_v h_{lv}} \tag{3.17}$$

The departure model given by Jeongbae Kim and Moo Hwan Kim is related with the liquid nitrogen fluid. Hence, it provides more accurate bubble departure diameter for the Liquid Nitrogen bubble. The bubble dynamics for liquid nitrogen is based on the bubble diameter obtained from the Jeongbae equation.

3.2. Forces acting on a detaching vapour bubble

The bubble growth takes place if the temperature of the liquid-vapour interface is more than the saturation temperature corresponding to the interfacial liquid pressure. The rate of bubble growth depends on the superheat and on the liquid temperature distribution at the nucleation site. The degree of superheat is the difference between the wall temperature and liquid saturation temperature. The internal vapour bubble pressure is governed by the interfacial liquid superheat, which causes to move the bulk liquid away from the vicinity of the heated surface. This internal vapour pressure is balanced by the different forces e.g. liquid inertia, liquid viscosity, buoyancy and surface tensions [115] etc. These forces can be combined using the vector addition as per the magnitude and directions. The net resultant force is responsible for the detachment and motion of the bubble from the heated surface.

The various forces acting during the bubble detachment condition are as follows:

(1) Surface tension force (F_{st})
(2) Shear lift force (F_{sL})
(3) Buoyancy force (F_b)
(4) Hydrodynamic force (F_h)
(5) Quasi-steady drag force (F_{qs})
(6) Contact pressure force (F_{cp})
(7) Unsteady drag force (F_{du})

Various forces acting during bubble detachment are shown in Fig. (3.1), in the directions parallel and normal to a horizontal heating surface.

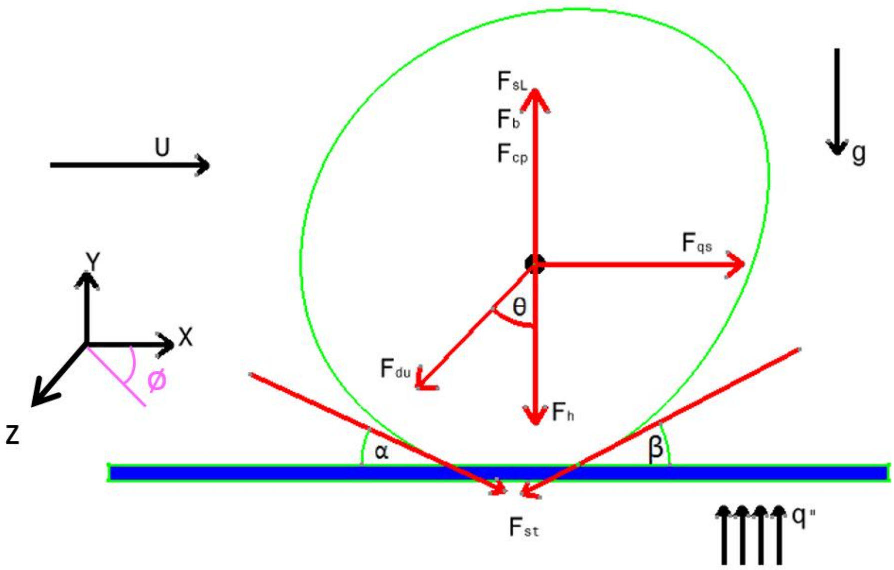

Figure 3.1 Forces on the vapor bubble during detachment from heating surface

3.2.1. Surface tension force (Fs)

This force generally occurs at the liquid-solid-vapour interline at a certain advancing (α) and receding (β) contact angle. During the bubble growth process, the bubble is not perfectly sphered, hence the contact angles differs on the advancing and receding side. Due to the difference in the contact angles, there is a net surface tension force component in x and y directions.

In order to determine F_{sx} (x-component of surface tension force) and F_{sy} (y-component of surface tension force), the effect of contact angles should be taken into consideration in the plane parallel and normal to the heating surface as shown in Fig. (3.1). The relation between the two contact angles can be generalized with the help of a third order polynomial. This general contact angle [71] is assumed as γ

$$\gamma(\emptyset) = \beta + (\alpha - \beta)\left[3\left(\frac{\emptyset}{\pi}\right)^2 - 2\left(\frac{\emptyset}{\pi}\right)^3\right], \qquad 0 \le \emptyset \le \pi \tag{3.18}$$

$$\gamma'(\emptyset) = \frac{6(\alpha - \beta)}{\pi}\left[\left(\frac{\emptyset}{\pi}\right) - \left(\frac{\emptyset}{\pi}\right)^2\right] \tag{3.19}$$

where ϕ is the polar angle around the bubble in the x-z plane. It satisfies γ(0) = β and γ(π) = α and the symmetry conditions γ'(0) = γ'(π) = 0. This is a good representation when the difference in α and β is not large.

Eq. (3.18) can be approximated as

$$\gamma(\emptyset) \approx \beta + (\alpha - \beta)\frac{\emptyset}{\pi} \tag{3.20}$$

The surface tension forces at x- and y- directions were given by Klausner et al. [61] as

$$F_{sx} = -\int_0^{\pi} d_w \sigma \cos\gamma \cos\emptyset d\emptyset \tag{3.21}$$

$$F_{sy} = -\int_0^{\pi} d_w \sigma \sin\gamma d\emptyset \tag{3.22}$$

where d_w and σ are the bubble contact diameter on the heater surface and surface tension respectively.

F_{sx} and F_{sy} equations are further simplified to

$$F_{sx} = -d_w.\sigma.\frac{\pi(\alpha - \beta)}{\pi^2 - (\alpha - \beta)^2}[sin\,\alpha + sin\,\beta] \tag{3.23}$$

$$F_{sy} = -d_w.\sigma.\frac{\pi}{(\alpha - \beta)}[cos\,\beta - cos\,\alpha] \tag{3.24}$$

The magnitude of the surface tension force can be calculated by using Eq. (3.23) and Eq. (3.24) in x and y directions. These forces will act in the negative x and negative y directions.

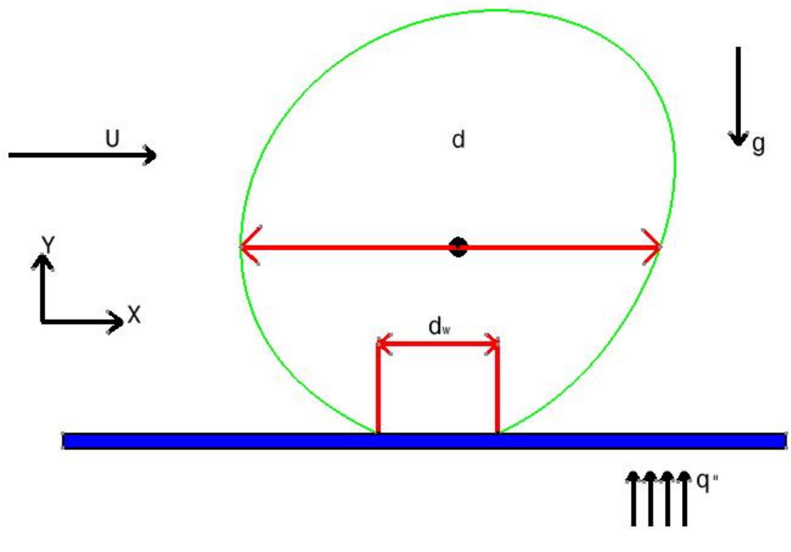

Figure 3.2 Vapour bubble representation showing departure ‘d’ and contact diameter ‘d_w’

Fig. (3.2) shows the wetted diameter dw and bubble diameter d.

3.2.2. Shear lift force (F_{sL})

Saffman [116] derived the shear lift force on a solid sphere at low Reynolds number. Auton [117] derived an expression for the shear lift force on a sphere in an inviscid shear flow. Mei and Klausner [118] modified Saffman's model to suit for a bubble and interpolated with Auton's equations to derive an expression for shear lift force over wide range of Reynolds number as

$$F_{sL} = \frac{1}{2} C_L \rho_L U^2 \pi r^2 \tag{3.25}$$

where r is the bubble radius, U is the uniform flow velocity, C_L is the shear lift coefficient given by:

$$C_L = 3.877 G_s^{1/2} \times \left[Re^{-m/2} + \left(0.344 G_s^{1/2}\right)^m \right]^{1/m}, m = 4 \tag{3.26}$$

$$G_{s=} \left|\frac{dU}{dy}\right| \frac{r}{U} \tag{3.27}$$

where G_s is the shear rate constant.

Here, Reynolds number, Re, is defined as $Re = \frac{\rho_L . U . d_o}{\mu_L}$, where d_o and μ_L are the hydraulic equivalent diameter and the dynamic viscosity of liquid, respectively.

For low heat flux and low-velocity flow, Cho et. al [58] developed a new relation for shear lift coefficient (C_L) as:

$$C_L = \frac{1}{2} \left[\frac{\left(1 + \frac{16}{Re}\right)}{\left(1 + \frac{29}{Re}\right)} \right] \tag{3.28}$$

The value of C_L varies with the change in Reynolds number. Tomiyama [119] reported that the value of shear lift coefficient becomes 0.3 and constant with the increase in the value of Reynolds number.

Tomiyama et al. [120] provided an estimate of shear lift coefficient using a curve of C_L vs. bubble departure diameter.

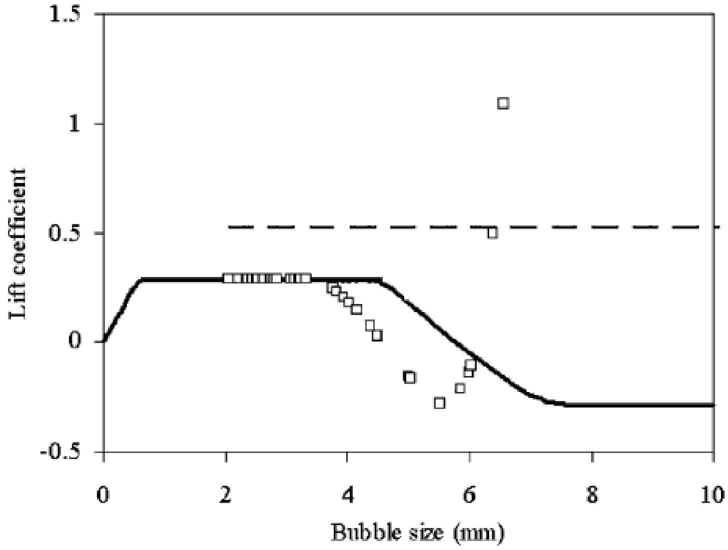

Figure 3.3 Lift coefficient according to the bubble size

It has been reported that the lift coefficient has a constant value of 0.28 with bubble diameters up to 5.8 mm and becomes negative with further increase in the diameter value as shown in Fig. (3.3).

Cho et. al [58] modified the relation as

$$F_{sL} = \frac{1}{2} C_L \rho_L \Delta U^2 \pi r^2 \tag{3.29}$$

where ΔU is the relative velocity between the liquid phase and bubble center of mass as shown in Fig. (3.4).

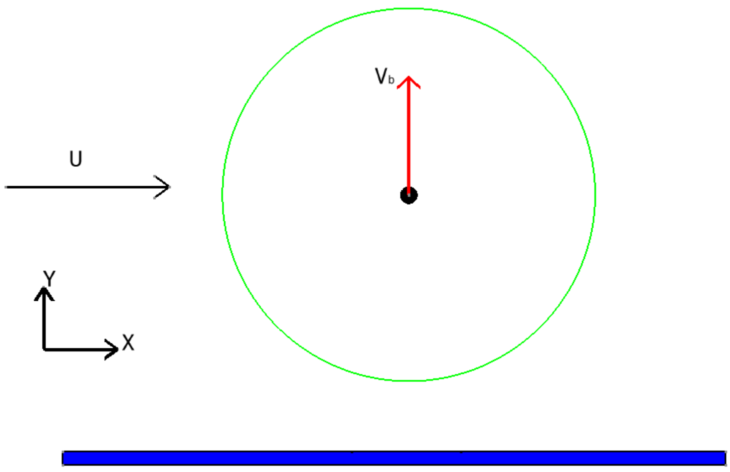

Figure 3.4 Relative velocity between bulk fluid velocity and bubble velocity

ΔU can be mathematically written as:

$$\Delta U = \sqrt{{V_b}^2 + U^2} \tag{3.30}$$

where V_b is the bubble departure velocity. In case of nucleate pool boiling ($U \approx 0$), hence the relative velocity becomes equal to the bubble departure velocity i.e. $\Delta U \approx V_b$. The bubble departure velocity is calculated as [121]:

$$V_b = \sqrt{\left(\frac{d_b g(\rho_L - \rho_G)}{2(\rho_L + \rho_G)} + \frac{2\sigma}{d_b(\rho_L + \rho_G)}\right)} \tag{3.31}$$

The relation given by Cho et. al [58] is suitable in case of pool boiling because of very low Reynold's number.

3.2.3. Buoyancy force (F_b)

The buoyancy force occurs due to the pressure differences associated with the liquid-vapour density in a body. Moreover, the natural convection current affects the liquid temperature distribution around the body. This buoyancy force acts on the bubble surface in contact with liquid and wall. This force can be corrected with the help of contact pressure force acting in the z-direction on the bubble surface in contact with the wall only.

The buoyancy force, F_b is obtained by integrating the hydrostatic component of the liquid pressure over the bubble [61]:

$$F_b = -\int_{s_1+s_2} (\Gamma_r - \rho_L g y - P_v) n_y dA \tag{3.32}$$

$$F_b = \frac{4}{3}\pi r^3 (\rho_L - \rho_G) g \tag{3.33}$$

where s_1 and s_2 denote the bubble surfaces in contact with the liquid and the wall, P_v is the vapour pressure inside the bubble, n_y is the y component of outward normal of bubble surface, Γ_r is the reference pressure at y=0, ρ_L and ρ_G are the liquid and vapour density respectively, g is the acceleration due to gravity.

3.2.4. Hydrodynamic force (F_h)

The hydrodynamic force acts on the contact area of the bubble with the solid surface. The hydrodynamic force F_h, may be estimated by considering an inviscid flow over a sphere in an unbounded flow field. Due to the symmetry over the majority of the bubble surface, the contribution to F_h is from the pressure on the top of the bubble over an area $\pi d_w^2/4$ [61]:

$$F_h = \frac{1}{2}\left(\frac{9}{4}\rho_L U^2\right)\frac{\pi {d_w}^2}{4} \tag{3.34}$$

3.2.5. Quasi-steady drag force (F_{qs})

The constant drag force acting in the direction of the flow field is known as quasi-steady drag force. Since the flow velocity of the fluid is very less, this force acts symmetrically on the vapour bubble. This force can be estimated only for a pure-spherical bubble. This component of drag force arises when the bubble is considered stationary in a uniform viscous flow. Klausner et al. [61] considered the effect of heated surface and modified the equation of force given by Mei and Klausner [118]. Hence this force can be determined by the Eq. (3.35).

$$F_{qs} = 6\pi\rho_L \nu U r\left[\frac{2}{3} + \left\{\left(\frac{12}{Re}\right)^n + 0.796^n\right\}^{-1/n}\right] \tag{3.35}$$

where n is 0.65.

3.2.6. Contact pressure force (F_{cp})

The contact pressure force at the reference point over the contact area is due to the pressure difference between inside and outside surface of a vapour bubble. This force is obtained by integrating the pressure difference along the bubble base and is sometimes referred to as a buoyancy correction force. Due to the axis-symmetry of the bubble, only the y direction is considered yielding a contact pressure of

$$F_{cp} = -\int_{S_2} (\Gamma_r - \rho_L g y - P_v) n_y dA \tag{3.36}$$

$$F_{cp} = \frac{\pi {d_w}^2}{4}\frac{2\sigma}{R_r} \tag{3.37}$$

where R_r is the radius of curvature of the bubble at the reference point on the surface x = 0, which is $R_r \sim 5r$ [61].

3.2.7. Unsteady drag force (F_{du})

The bubble growth occurs either in a uniform unbounded inviscid liquid on the spherical bubble or in a hemispherical bubble attached to the heated surface. In general, asymmetric bubble growth will result in the unsteady drag force. This force depends mostly on the bubble shape. The growth force, F_{du}, is modelled by considering a hemispherical bubble expanding in an inviscid liquid, which is given by Zheng et al. [75]:

$$F_{du} = \rho_L \pi r^2 \left(\frac{3}{2} C_s \dot{r}^2 + r\ddot{r}\right) \tag{3.38}$$

where $(\cdot)$ indicates differentiation with respect to time. The constant C_s and θ is taken to be 20/3 and π/18 according to Zeng et al. [122].

The unsteady drag force due to the asymmetrical growth of the bubble in x and y directions are:

$$F_{dux} = F_{du} \sin\theta \tag{3.39}$$

$$F_{duy} = F_{du} \cos\theta \tag{3.40}$$

For vertical direction, F_{duy} is considered for the bubble departure force.

3.2.8. Forces in vertical direction

The net force can be calculated by summing all the upward and downward forces acting on the bubble. The upward forces acting on the bubble are buoyancy force (F_b), shear lift force (F_{sL}), and contact pressure force (F_{cp}). The downward forces acting on the bubble are the hydrodynamic (F_h), the capillary or surface tension force (F_{sy}) and unsteady drag force (F_{duy}). Hence the net force acting on the detaching bubble in vertical direction can be written as:

$$\sum F = F_b + F_{sL} + F_{cp} + F_h + F_{sy} + F_{duy} \tag{3.41}$$

The bubble will not depart from the surface till $\sum F < 0$ and as soon as $\sum F > 0$, the bubble will depart from the surface.

3.3. Acceleration of bubble

This unbalanced net force $(\sum F)$ in the y-direction is responsible to produce an initial acceleration in the bubble. This initial acceleration is calculated using Newton's second law,

$$a = \frac{\sum F}{M_e} \tag{3.42}$$

where the M_e is the entrained mass of the bubble. The mass of bubble is always calculated as an entrained mass, which is carried along with the bubble during its motion within the fluid. When the bubble (spherical vapour body) moves through the liquid, the density of the bubble is much lighter than the liquid density. Hence, the entrained mass of the bubble is much larger than the mass of vapour content in the bubble and so subsequently entrained mass dominates. The entrained mass of bubble [123] is considered as half of this displaced mass of liquid. The entrained mass can be written as

$$M_e = \rho_L \left(\frac{2}{3}\pi r^3\right) \tag{3.43}$$

As per the Leighton [123] also, the ratio of displaced mass is the twice of the entrained mass, which provides the initial bubble size-independent acceleration as 2g.

3.4. Forces acting during bubble motion

The bubble translation comes into play after the vapour bubble departs from the heated wall with an unbalanced force acting in the y-direction i.e. opposite to the gravitational field. The motion of the bubble is described in terms of displacement, velocity, and acceleration arising from the net force.

As reported by Klausner et al. [61], the order of magnitude of the sum of bubble detachment forces acting in the x-direction is of the order of 10^{-9} N. However, the summation of the forces acting along y-direction is 10^3 times greater than the summation of forces in the x-direction. Moreover, the major forces (Fig. (3.5)) which affect the motion of the vapour bubble are as follows:

1) Inertia force (F_i)
2) Buoyancy force (F_b)
3) Drag force (F_d)

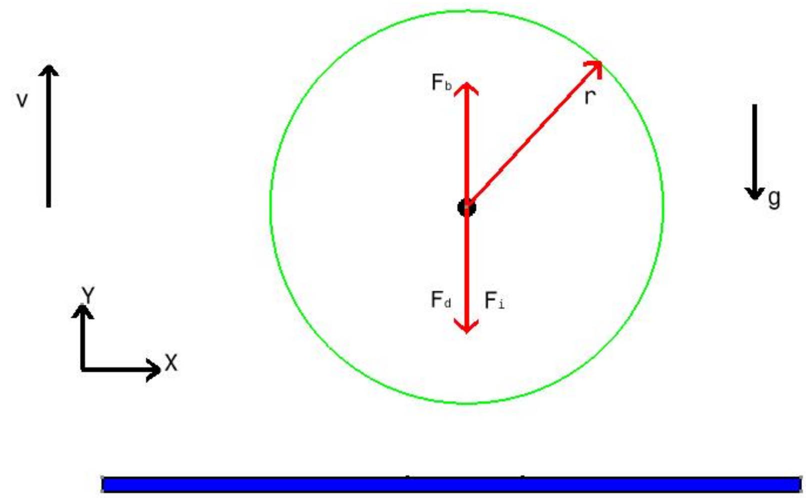

Figure 3.5 Forces acting on a vapour bubble during its motion

3.4.1. Vapour bubble motion criteria

a) The departed vapour bubble has been considered to be purely spherical. Because at low mass flux, the shape of the bubble is almost spherical.
b) For a sphere, the ratio of the displaced liquid mass is twice the entrained mass "M" [124].
c) The radius of the bubble is assumed to be constant during its motion. Because as per the bubble growth studies, the variation in radius is very negligible w.r.to the bubble departure radius at low mass and heat flux.
d) For the motion analysis of the vapour bubble, a single spherical bubble has been considered for this purpose.

3.4.2. Inertia force (F_i)

As the vapour bubble departs from the heated surface, it gains an initial acceleration from the unbalanced net force in the y-direction. Due to this acceleration, the bubble attains certain momentum which causes the liquid field to impart inertia. This inertia for the liquid surrounding the bubble needs to be accounted. Due to this inertia, the acceleration of the bubble tends to decrease from initial acceleration making the velocity component to reach its asymptotic value. This asymptotic value of velocity is termed as the Terminal velocity.

The inertia force is dependent on the mass of surrounding liquid displaced by the bubble during its motion. Half of this displaced mass is considered as the entrained mass of bubble [124]. This entrained mass is also referred as the added mass with the bubble. The bubble's motion is resisted by this added mass imposing as inertia force F_i, which is calculated as:

$$F_i = Ma \tag{3.44}$$

where a is the initial acceleration of the bubble and M is the mass of the bubble which is equal to the entrained mass of bubble Me. Hence the inertia force is written as

$$F_i = \rho_L \left(\frac{2}{3}\pi r^3\right) a \tag{3.45}$$

3.4.3. Buoyancy force (F_b)

This force is the outcome of pressure exerted on the vapour bubble by the surrounding liquid. Bubble's upward motion is driven by its buoyancy, i.e. by the weight of displaced liquid:

$$F_b = \rho_L V g \tag{3.46}$$

$$V = \frac{4}{3}\pi r^3 \tag{3.47}$$

where V and r are the volume and radius of the bubble respectively.

3.4.4. Drag force (F_d)

The drag force is exerted on the bubble due to the viscosity of water during the motion of bubble. The direction of drag force is always be opposite to the flow direction. After the bubble departs from the heating surface, it gains some initial velocity. This velocity imparts motion to the vapour bubble, which eventually gives rise to the drag force. This drag will be approximated by Stokes's expression [125].

$$F_d = 6\pi\rho_L \nu r v \tag{3.48}$$

where ν is the kinematic viscocity of the fluid and v is the bubble velocity within the fluid.

This expression is strictly valid for a sphere moving at constant velocity. This approximation is selected because the resulting simple solution provides ready insight to the physics of bubble dynamics. The error is negligible at early times (i.e. before reaching to its terminal velocity), where drag force is overshadowed by the inertia force, and at late times (i.e. at asymptotic constant terminal velocity v_T), the drag force dominates over the inertia force during its motion. The value of time scale is defined in the bubble migration (Section 3.5.3).

3.4.5. Equation of motion

Applying Newton's second law, viz. setting buoyancy force F_b equal to the sum of the liquid generated forces F_i *and* F_d, the equation of motion is.

$$F_b - (F_i + F_d) = 0 \tag{3.49}$$

$$\rho V g - \frac{\rho V a}{2} - 6\pi\rho\nu r v = 0 \tag{3.50}$$

or

$$\frac{\rho V a}{2} + 6\pi\rho\nu r v - \rho V g = 0 \tag{3.51}$$

Dividing all terms by $\frac{\rho V}{2} = \frac{2}{3}\pi r^3 \rho$, the equation is

$$a + \left(\frac{9\nu}{r^2}\right) v - 2g = 0 \tag{3.52}$$

The radius of the bubble is taken to be constant as per the bubble motion criteria. The resulting error is insignificant at early times, where inertia predominates over drag. Even at late times, the error is unimportant at a low depth where the hydrostatic pressure is dominated by atmospheric pressure. Due to this, the bubble size becomes relatively independent of the vertical distance‘s’ migrated by the bubble.

3.4.6. Bubble migration

The analogous equation of motion for the Eq. (3.52) is,

$$a + \frac{v}{t} - 2g = 0 \tag{3.53}$$

Comparing the Eq. (3.52) and Eq. (3.53), the migration time ‘t’ for the spherical bubble is obtained as,

$$t = \frac{r^2}{9\nu} \tag{3.54}$$

During migration of bubble, two conditions exists with respect to time

(1) Early time zone $\left(t \ll \frac{r^2}{9\nu}\right)$

(2) Late time zone $\left(t \gg \frac{r^2}{9\nu}\right)$

The migration conditions in terms of acceleration, velocity, and displacement are different for both the conditions.

3.4.6.1Early time zone

As soon as bubble departs from the heated surface, the inertia forces will dominate over the drag force. So drag force will be negligible w.r.to inertia force. Therefore buoyancy force and inertia force will act on the spherical bubble. For a bubble migration initiated at time zero or early time, it has initial acceleration. Hence,

$$a \approx 2g \tag{3.55}$$

The bubble velocity and displaced can be found out by integrating the Eq. (3.55),

$$v = 2gt \tag{3.56}$$

$$s = gt^2 \tag{3.57}$$

The large acceleration is due to the fact that the entrained mass is half the displaced mass of liquid. This acceleration is independent of bubble size, but it is a function of the buoyant body's aspect ratio. The aspect ratio for any body is defined as the ratio of length to its diameter. If spherical bubble elongates in the vertical direction and takes the shape of a ellipsoid, then it experiences even larger acceleration in spite of smaller entrained mass. In the present case, the bubble is considered as spherical, hence the acceleration will be almost equal to the entrained mass.

3.4.6.2Late time zone

As the bubble translates further within the liquid and enters into the late time zone, drag force dominates over the inertia force. So inertia force is negligible w.r.to drag force. Therefore buoyancy force and drag force will act on the spherical bubble. Hence, the asymptotic terminal velocity can be determined as,

$$v = v_T = \frac{2gr^2}{9\nu} \tag{3.58}$$

From the Eq. (3.58), it is evident that the asymptotic terminal velocity (v_T) is a function of square of bubble radius i.e. with the increase in size of the bubble, the late time velocity tends to increase in the parabolic fashion.

$$\frac{9\nu}{r^2} = \frac{2g}{v_T} \tag{3.59}$$

The equation of motion is conveniently formulated in terms of this asymptotic velocity;

$$a + \frac{2g}{v_T} v - 2g = 0 \tag{3.60}$$

It is known that

$$a = \frac{d^2s}{dt^2}; \quad v = \frac{ds}{dt} \tag{3.61}$$

The above Eq. (3.60) is;

$$\frac{d^2s}{dt^2} + \left(\frac{2g}{v_T}\right)\frac{ds}{dt} - 2g = 0 \tag{3.62}$$

$$\frac{d^2s}{dt^2} - \left(-\frac{2g}{v_T}\right)\frac{ds}{dt} = 2g \tag{3.63}$$

The Eq. (3.63) is a second order inhomogeneous equation with determined constant. The solution is obtained using the addition of complementary function (CF) and particular solution (PS).

The solution of this differential equation will provide the displacement of bubble migration w.r.to time scale function and is obtained as

$$s(t) = v_T t - \left(\frac{v_T^2}{2g}\right)\left[1 - e^{\left(\frac{-2gt}{v_T}\right)}\right] \tag{3.64}$$

Differentiating Eq. (3.64), the bubble velocity function w.r.to time is

$$v(t) = v_T \left[1 - e^{\left(\frac{-2gt}{v_T}\right)}\right] \tag{3.65}$$

Differentiating Eq. (3.65), the bubble acceleration function w.r.to time is

$$a(t) = 2g\, e^{\left(\frac{-2gt}{v_T}\right)} \tag{3.66}$$

These kinematic equations obtained are the exponential function of the time scale factor. Moreover, the bubble displacement and velocity are directly proportional to the terminal velocity gained at the later stage of its motion.

3.5. Bubble impact force

The vapour bubble will attain certain velocity and acceleration after traversing a finite distance. During its motion, if a vapour bubble encounters any structural component within the system then it will collide with the surface of the system with a certain momentum. This collision of the bubble will exert a force on the surface. If any force acts on the body for the short duration, an impulse is generated on the body. This impulsive force is called as impact force. The impact force is defined in terms of change in momentum before and after the impact / collision. This impulsive force is not constant during the collision time and it varies in semi-sinusoidal fashion as shown in Fig. (3.6).

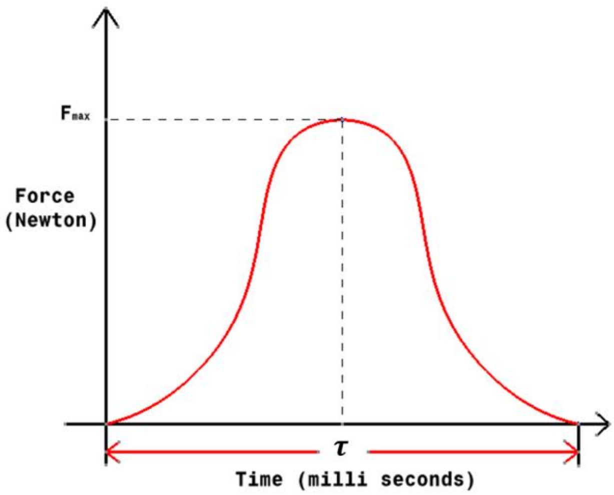

Figure 3.6 Impact force variation with respect to collision time

where τ is the impact or collision time period. Mostly the impact time period is quite less i.e. in milli seconds. The total impact force is the area under the force versus time curve.

The generated impact force is the time dependent function which gives rise to the time-dependent deceleration. Hence the impact force generated by bubble will depend on the deceleration magnitude at the time of the collision. The impact force can be obtained by considering the area under the force-time curve.

For the present study, this time interval has been taken as the ratio of bubble diameter to the bubble velocity. The minimum distance travelled by the bubble between the two successive impacts on the surface of the system is equal to the bubble diameter.

$$\tau = \frac{2r}{v(t)} \tag{3.67}$$

where $v(t)$ is the bubble velocity at the time of impact.

3.5.1. Mathematical formulation of impact force exerted by a bubble on a surface

Using the Newton's law of motion, the bubble impact force on the surface will be directly proportional to the bubble deceleration. The magnitude of the bubble deceleration will depend on the traversing time before colliding the surface.

$$F = Ma_D(t) \tag{3.68}$$

where M is the mass of the bubble and $a_D(t)$ is the bubble's deceleration sensed by the bubble during migration time (t). To get this deceleration function w.r.to time scale factor, a semi sinusoidal function as $\emptyset(t)$ has been considered. Hence the deceleration function $a_D(t)$ will be directly proportional to the $\emptyset(t)$.

$$a_D(t) \propto \emptyset(t) \tag{3.69}$$

$$a_D(t) = K_D \emptyset(t) \tag{3.70}$$

where K_D is a bubble deceleration constant and

$$\emptyset(t) = \sin\left(\frac{\pi t}{\tau}\right), \;\; 0 \leq t \leq \tau \tag{3.71}$$

Therefore deceleration function becomes

$$a_D(t) = K_D \sin\left(\frac{\pi t}{\tau}\right), \quad 0 \leq t \leq \tau \tag{3.72}$$

The value of bubble deceleration constant is determined by considering that the bubble will come to halt during the impact time period [126].

$$v(t) = \int_0^\tau a_D(t)\, dt, \quad 0 \leq t \leq \tau \tag{3.73}$$

$$v(t) = K_D \int_0^\tau \sin\left(\frac{\pi t}{\tau}\right) dt \tag{3.74}$$

$$v(t) = K_D \left[-cos\left(\frac{\pi t}{\tau}\right)\right]_0^\tau \tag{3.75}$$

$$v(t) = K_D \left(\frac{2\tau}{\pi}\right) \tag{3.76}$$

$$K_D = v(t) \left(\frac{\pi}{2\tau}\right) \tag{3.77}$$

Substituting the value of τ in Eq. (3.77), Therefore, deceleration constant is

$$K_D = [v(t)]^2 \left(\frac{\pi}{4r}\right) \tag{3.78}$$

Hence the acceleration $a_D(t)$ can be written as

$$a_D(t) = [v(t)]^2 \left(\frac{\pi}{4r}\right) \sin\left(\frac{\pi t}{\tau}\right), \quad 0 \leq t \leq \tau \tag{3.79}$$

Replacing the value of M and $a_D(t)$ in Eq. (3.68), the impact force is

$$F(t) = \rho_L \left(\frac{2}{3}\pi r^3\right) [v(t)]^2 \left(\frac{\pi}{4r}\right) \sin\left(\frac{\pi t}{\tau}\right), \quad 0 \leq t \leq \tau \tag{3.80}$$

$$F(t) = \frac{\rho_L [\pi r v(t)]^2}{6} \sin\left(\frac{\pi t}{\tau}\right), \quad\quad 0 \leq t \leq \tau \tag{3.81}$$

3.5.2. Maximum impact force exerted by a bubble on a surface

From the bubble impact force formulation, the impulsive force exerted by a bubble on the subsequent surface at the time of the collision is obtained explicitly. According to Eq. (3.81), it is evident that the impact force is varying in a sinusoidal manner. Moreover, the force is largely dependent on the bubble radius and its velocity during a collision. The maximum force is determined by substituting the value of 't' as τ/2 in the above equation. The maximum exerted force F_{max} is obtained as:

$$F(t)_{max} = \frac{\rho_L[\pi r v(t)]^2}{6}, \qquad t = \frac{\tau}{2} \tag{3.82}$$

This maximum force is dependent on bubble velocity during the collision which varies significantly with migration time-scale function. The impact velocity is a constant for a particular dimension of bubble flow field. It, however, increases with increase in bubble migration period which is decided by the field dimension. The impact velocity becomes equal the bubble terminal velocity at a very later stage of motion i.e. when $t \gg \frac{r^2}{9\nu}$. At the point when bubble reaches its terminal velocity, the exerted impact force becomes a constant and becomes independent of impact velocity. The maximum constant force is calculated by replacing the value of v(t) by V_T in Eq. (3.82) and is given as follows:

$$F_{max} = \frac{\rho_L[\pi r v_T]^2}{6} \tag{3.83}$$

$$F_{max} = \frac{2}{243}\rho_L\left[\frac{\pi r^3 g}{\nu}\right]^2 \tag{3.84}$$

At late time conditions, the maximum impact force becomes constant for a particular bubble radius.

3.6. Closing remarks

In this Chapter, the bubble departure diameter according to different models is presented. The best model for the liquid nitrogen bubble is Jaongbae model. The bubble departure diameter provides the base for the departure forces. The net departure force gives the value of initial acceleration for the bubble.

The bubble motion parameters help to formulate the impact velocity and acceleration on the surface by the bubble. This impact velocity is the base for the impact force on the structure. The generalized formulation of the induced impact force by the single bubble is presented. This formulation presented in this chapter provides a basis for the study of bubble-induced vibration and noise, which is presented in the next Chapter.

Chapter 4

Bubble-Induced Vibration and Noise

4.1. Introduction

There have been several studies carried out on the behaviour of vapour bubbles in the past decades using different techniques such as high-speed photography and acoustic measurement in order to determine the vapour bubble evolution by considering aspects such as formation, detachment and its motion in the fluid field. Bubble-induced vibration and noise in a pool boiling leads to account for the phenomenon known as ‘Vibroacoustics’ (also called as ‘Structural Acoustics’). A structure such as thin flat plates or thin curved shells (i.e. the thickness dimension is very much less than those defining the exterior surface) tend to vibrate in a manner in which the predominant motion occurs in a direction normal to the surface. The vibration displaces and compresses the fluid, which results into producing the sound or noise by the structure [127].

For evaluating the acoustic effect of the sound radiated from such structures, it is crucial to study the dynamic response parameters such as Frequency Response Function (FRF), Mechanical mobility and Admittance. In addition, the response of fluid movement on the mechanical structure also needs to be studied thoroughly for determining the wave phenomena and their associated natural frequencies. At last, the vibration spectrum formation due to force, displacement, velocity, and acceleration needs to be analyzed for finding the noise level occurring from bubble induced vibration.

4.2. Dynamic response characteristics

The dynamic response of any mechanical structure (cylindrical shell) due to harmonic excitation is expressed in the terms of its mechanical mobility [128]. The excitation will induce the mechanical vibrations in the structure. For the analysis of these vibrations, Frequency Response Function (FRF) is one of the most commonly used tools [129].

4.2.1. Frequency response function (FRF)

FRF is defined as the structural response to an applied force as a function of frequency [130]. The response may be given in terms of displacement, velocity, or acceleration. The schematic for FRF is shown in Fig. (4.1).

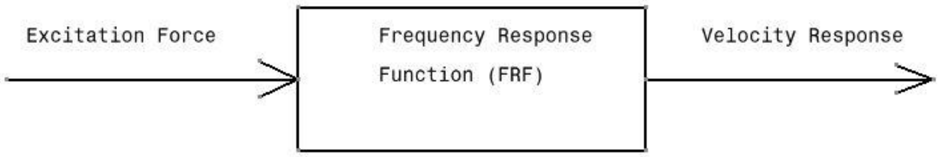

Figure 4.1 Input and output response due to Frequency Response Function (FRF)

There are different FRF’s or transfer functions. These FRF’s are defined as per the input and output parameters. FRF is expressed as the ratio of output response to the input parameter. If the output response is velocity and input parameter is the force then FRF can be termed as mobility. Using the mechanical mobility, the acceleration spectrum of the outer shell can be determined.

4.2.2. Mechanical admittance

Mechanical admittance is realized using the concept of mechanical mobility. Mechanical mobility measures the ability to allow the motion of structural unit when subjected to a harmonic force. Mechanical mobility is the inverse function of mechanical impedance. Mechanical impedance depends on the excitation frequency (ω). At resonance frequency, mechanical impedance is lower i.e. less force is required to move the structural element with a certain velocity. Hence, at the resonance frequency, mechanical mobility is high.

The generalized mechanical mobility is defined as the ratio between the complex amplitudes of the velocity and force field at the excitation frequency (ω) [130]. This complex mobility (y) is also expressed as

$$y = Y + iB \tag{4.1}$$

where Y is the real part of the mechanical mobility function and is also called as mechanical admittance and B is the imaginary part of the mobility function and is called as susceptance [131].

Mechanical mobility can be either transfer mobility function or direct / driving point mobility function. According to ISO 7626-1 [130], Transfer mechanical mobility function is defined as the frequency response function formed by the ratio of velocity response phasor at point 'i' to the excitation force phasor at the point 'j' (as shown in Fig. (4.2)). In order to measure the frequency response function of the structure, all the measuring points are allowed to respond freely without any constraints except the normal support points.

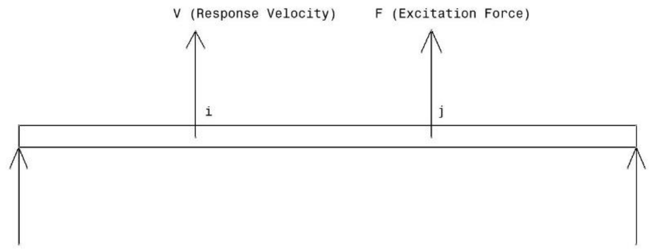

Figure 4.2 Transfer Mobility Function of the System

The definition is given mathematically as:

$$y_{ij} = {}^{v_i}\!/_{F_j} \tag{4.2}$$

where v_i is the velocity-response phasor at point i and F_j the force phasor at point j.

If the frequency response function is formed by the velocity response and excitation force at the same point i, it is known as direct / driving point mechanical mobility function [130].

$$y_{ii} = {}^{v_i}\!/_{F_i} \tag{4.3}$$

Driving point admittance (Y_{ii}) of any point in the mechanical structure is defined as the mechanical noise induced at the same point in the structure. For an accurate analysis of the noise performance, it is necessary to calculate the correlation between those two points (same or different) in the mechanical structure. Mechanical admittance of a linear mechanical structure is found by considering the real part of the mechanical mobility function. In the case of direct admittance, the complex mobility function (y_{ii}) can be made equivalent to its real part i.e. the driving point admittance (Y_{ii}). The velocity response can be either translational or rotational, and the excitation can be either rectilinear force or a moment.

4.2.2.1Mechanical-Electrical system analogy

To evaluate the admittances of different mechanical components, understanding of electrical impedances is important. There are two kinds of mechanical-electrical analogies that can be used to represent the mechanical system in the electrical domain. First one is the mobility analogy and the other one is the impedance analogy [132]. In the case of mobility analogy, electrical impedance is considered equivalent to the inverse mechanical impedance (also known mechanical admittance). Here, a damper is analogous to a resistor, mass is analogous to a capacitor and the spring is analogous to an inductor. The Table (4.1) shows the relationship of the mechanical system and electrical system through the mobility analogy.

Table 4.1 Mobility analogy for conversion from mechanical system to electrical system

Mechanical system	Electrical circuit
Force (F)	Current (I)
Velocity (v_s)	Voltage (V)
Mass (M_s)	Capacitance (C)
Spring ($1/k_s$)	Inductance (Li)
Damper (1/c)	Resistance (R)

In mobility analogy 'compliance of the spring (inverse of stiffness i.e. $1/k_s$)' is considered equivalent to the 'inductance of an inductor', 'damping of the shock absorber (inverse of the conductance i.e. 1/c)' is considered equivalent to the electrical resistance of a resistor and 'mass of the object' is considered equivalent to the capacitance of the capacitor. The relation between electrical impedance and mechanical admittances of different lumped components through mobility analogy [133] is shown in the Table (4.2).

Table 4.2 Admittance and impedance relation for electrical and mechanical components

Electrical System		Mechanical System		
Components	Electrical Impedance (Z)	Components	Mechanical Admittance (Y)	$\|Y\|$
Capacitor	$Z_C = \frac{1}{i\omega C}$	Mass	$Y_m = \frac{1}{i\omega M_s}$	$\|Y_m\| = \frac{1}{\omega M_s}$
Inductor	$Z_L = i\omega L_i$	Spring	$Y_k = \frac{i\omega}{k_s}$	$\|Y_k\| = \frac{\omega}{k_s}$
Resistor	$Z_C = R$	Damper	$Y_c = \frac{1}{c}$	$\|Y_c\| = \frac{1}{c}$

4.2.2.2Electrical analogy for spring-mass system

Any linear spring mass mechanical structure can be represented in an electrical circuit as shown in Fig. (4.3).

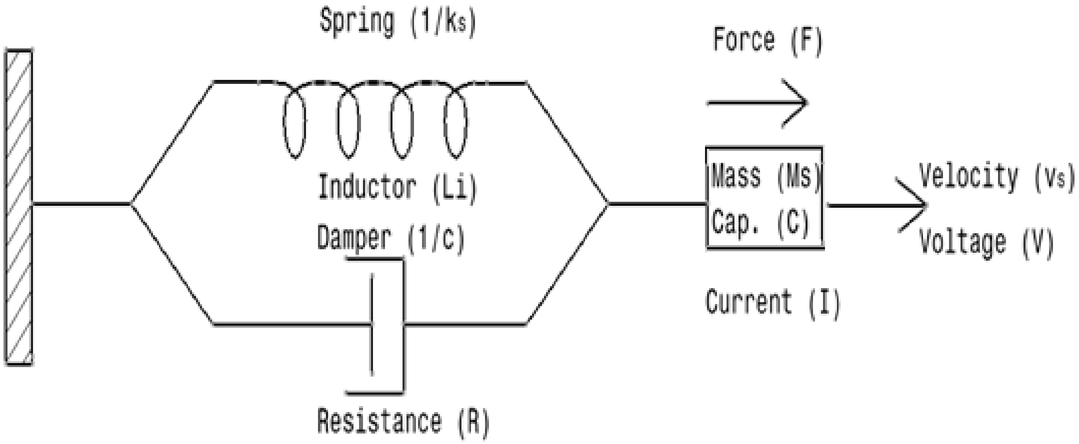

Figure 4.3 Representation of the spring mass mechanical system in an electric Circuit

The admittance dependence as a function of the frequency of these idealized mechanical elements is presented in Fig. (4.4). For analyzing different structural dynamics and their vibration characteristics in a defined low-frequency bandwidth, mechanical admittance plays a crucial role. For characterizing the response of any mechanical structure, it is a mandate to divide the whole system into different lumped elements such as mass, spring, and damper.

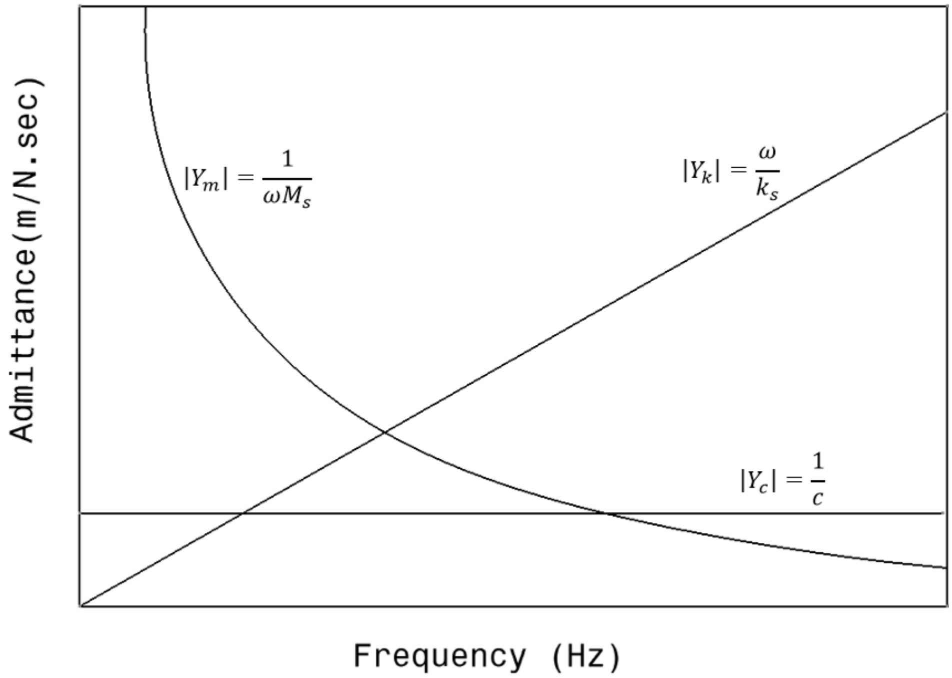

Figure 4.4 The mobility magnitudes of an idealized mechanical resistance$|Y_c|$, spring $|Y_k|$ and mass $|Y_m|$ as a function of frequency

These sub-elements can be used either in a solitary or in a group (i.e. series or parallel connection) to determine their resultant admittance. The use of the mechanical elements depends totally on the structural constraints and frequency range [134]. The magnitude of mechanical admittance helps in calculating the structure-borne noise level of the presumed elements under consideration.

4.3. Bubble–structure interaction

When any kind of disturbance induces within the fluid i.e. either to due fluid flow boiling or nucleate boiling (bubble-structure collision), the solid structure in contact with the fluid experiences vibrational instabilities [135]–[137]. These vibrational instabilities tends to generate a sound field which can be controlled using:

a) the longitudinal distribution of the vibrational acceleration component normal to the solid structure surface,
b) the geometry of the vibrating surface,
c) acoustic features of the surface surrounding the fluid, and
d) fluid properties

Vibrations resulting from fluid-structure interaction are basically acoustic wave phenomena. These wave fields are generated from any point considered within the interface of the fluid-structure medium. Moreover, these generated waves extend further and are influenced by the various other points in the medium making the vibration study and calculation rather complex. Also, there is a lack of general analytical models to evaluate this complexity. Therefore only numerical solution to the equations governing the induced vibration from the fluid-structure interaction is a feasible choice. Nevertheless, the effect of induced vibration varies according to the structural configuration. In most of the cases, the complex structural geometry and material properties make the analysis cumbersome. In recent years, circular cylinder shells of different configuration have found potential applications such as fluid storage tanks, aircraft fuselages, fluid tubes etc. and a lot of research has been done to analyze its behaviour in response to the vibrational disturbances. These vibrations can lead to a response in displacements that may occur in three directions i.e. radial, axial and circumferential. Due to coupling between these directions and induced stresses from the flexural surface, makes the vibration waves complex.

Usually, the configuration of cryopump is thin circular cylindrical shell i.e. its thickness is less than $1/10^{th}$ of the outer diameter. Accordingly, a thin closed circular shell has been taken into consideration with following assumptions:

1. The presence of residual stress has been neglected.
2. The structure of cylindrical shell is homogenous as well as isotropic.
3. The cylindrical shell considered is of uniform thickness throughout its length.

Parameters associated with the cylindrical shell such as thickness to radius ratio, Poisson's ratio, and wave number is varied during the study.

4.3.1. Wave parameters

As the acoustic wave generated from structure-fluid interaction, the disturbance at any point in space will vary sinusoidally in time at the same frequency as that of the generator, provided the medium responds linearly to the disturbance. The spatial period of a simple harmonic wave is commonly described by its wavelength λ. However, the spatial variation is better described by an associated quantity that represents phase change per unit distance and is equal to ω/c_{ph}, where, ω is the circular frequency and c_{ph} is the phase velocity of the wave. This is termed 'wavenumber' and is generally symbolized by k. One wavelength clearly corresponds to an x-dependent phase difference of 2π, hence $\omega\lambda/c_{ph} = k\lambda = 2\pi$.

Wavenumber 'k' is actually the magnitude of a vector quantity that indicates the direction of propagation as well as the spatial phase variation. This quantity is of vital importance to the mathematical representation of two and three-dimensional wave fields.

For a cylindrical shell, there are three mode shapes that are considered for the vibration analysis. They are:

1. Radial (Flexural)
2. Longitudinal (axial)
3. Circumferential (torsional)

In any cylindrical shell, there are three separate natural frequency for every mode shape (i.e. flexural, axial and circumferential). In most of the cases, the lowest natural frequency is associated with the motion that is primary radial. However, according to the shell size, the low-frequency modes are recognized as axial or circumferential rather than radial. For estimating the natural frequencies, the parameters such as wavenumber in axial direction 'k_m' and the circumferential mode number 'n' is obligatory. The value of 'n' should be in integers and independent of the imposed boundary conditions.

4.3.2. Vibration mode shapes

Any complex body (i.e. more complicated than a single mass on a simple spring) can vibrate in many different ways. Each of these vibrating ways will have their own frequency. The initial displacements of any mechanical systems that cause it to vibrate harmonically are called as mode shapes.

Depending upon the value of n, different mode shapes can occur corresponding to the circumferential wavenumber (Fig. (4.5)). The modes can be categorized as follows:

1. If n = 0, it corresponds to breathing, torsional and axial mode where any point on the cross section of cylinder vibrates harmonically in a radial, circumferential and axial direction respectively.
2. If n = 1, it corresponds to bending and axial shear modes the cross section of the cylinder remains the same.
3. If n > 1, it corresponds to lobar modes where the number of lobes formed depends on the value of n.

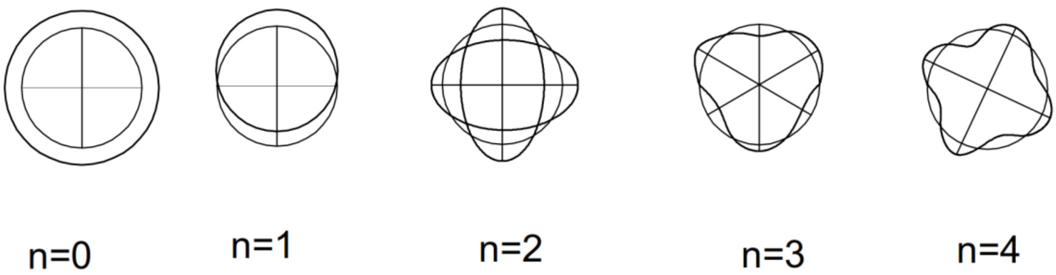

Figure 4.5 Circumferential mode shapes of a cylindrical shell [88]

Different axial wavenumbers 'k_m' in the longitudinal direction of the thin cylindrical shell exists corresponding to the applied boundary conditions. For determining the mode shape of a thin circular cylinder, mode parameters such as circumferential mode parameter 'n' and axial mode parameter 'm' are essential.

As the flexural mode shapes of cylindrical shells in the axial direction are assumed to be of the same form as a transversely vibrating beam, with the same boundary conditions, the axial wavenumber, 'k_m' can be evaluated by using beam function in case of flexural vibrations as shown in Table (4.3).

Table 4.3 Wavenumbers for different boundary conditions [138]

Boundary conditions	**Wave numbers (k_m)**
Clamped-free	$(2m-1)\pi/2L$
Free-simply supported	$(4m-1)\pi/4L$
Simply supported-simply supported	$m\pi/L$
Clamped-simply supported	$(4m+1)\pi/4L$
Clamped-clamped	$(2m+1)\pi/2L$
Sliding-simply supported	$(2m-1)\pi/2L$
Free-free	$(2m+1)\pi/2L$

4.4. Nonplanar vibrations of a cylindrical shell

A concentric cylindrical shell with thickness 't', radius 'R_o' and coordinate system r, ψ, z in reference to the Cartesian coordinate has been considered for the vibration analysis as shown in Fig. (4.6). In a wave propagation approach, the solution to the equations of motion is estimated using three displacement components, 'u', 'v', 'w' in an axial, tangential, and radial direction respectively. When the response displays axial dependence, the motion of an infinite or simply supported shell is described by the displacement components as:

$$\mathrm{u} = \sum_{m,n} U_{mn} \cos n\psi \cos k_m z \cos \omega t \tag{4.4}$$

$$v = \sum_{m,n} V_{mn} \sin n\psi \sin k_m z \cos \omega t \tag{4.5}$$

$$\mathrm{w} = \sum_{m,n} W_{mn} \cos n\psi \sin k_m z \cos \omega t \tag{4.6}$$

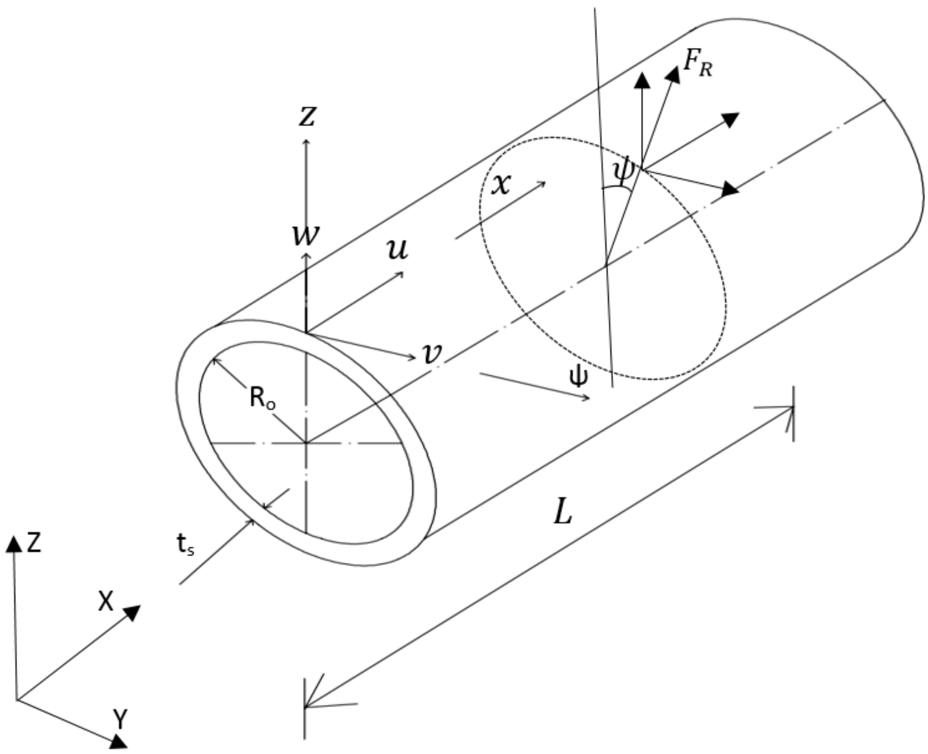

Figure 4.6 Circular cylindrical shell: Coordinate system and dimensions

where U_{mn}, V_{mn}, and W_{mn} represents the displacement amplitudes of the three components.

The motion so described consists of standing waves in both the circumferential and axial directions.

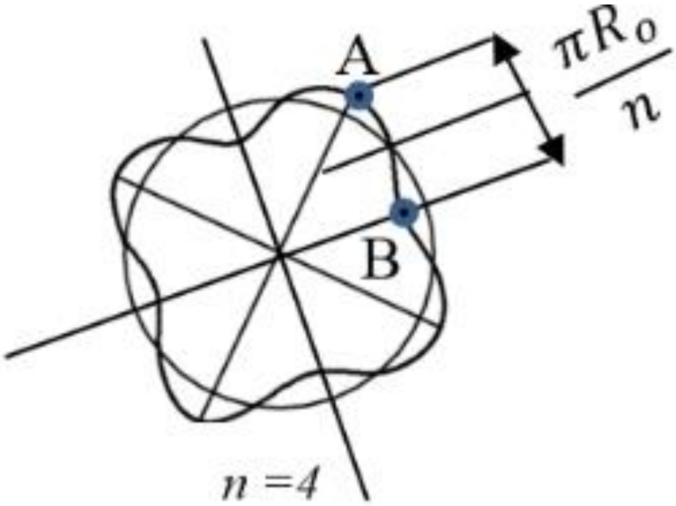

Figure 4.7 Representation of distance between the radial displacement nodal lines in the circumferential direction of the cylindrical Shell

The Fig. (4.7) denotes the lobar modes for n = 4, where point 'A' refers to the maximum radial distance from the center along the circumference and point 'B' refers to the minimum distance from the center along the circumference. The separation between the two points A and B along the circumference direction of the cylindrical shell is calculated by using the equation $2\pi R_o/2n$ i.e. $\pi R_o/n$. The radial displacement of the cylindrical shell along the axial direction is evaluated by considering axial wavelength of $2\pi/k_m$.

4.4.1. Generalized equations of motion

The generalized equations of motion for the cylindrical shell are formulated by Donnell [139] with the following assumptions:

1. The change in the twist and curvature of the cylindrical shell is same as that of the flat plate.
2. There is a negligible effect of transverse shearing-stress resultant force along the circumferential direction.

These equations can be written as [139]:

$$\frac{\partial^2 u}{\partial z^2}+\left(\frac{1-\nu}{2{R_o}^2}\right)\frac{\partial^2 u}{\partial \psi^2}+\left(\frac{\nu}{R_o}\right)\frac{\partial w}{\partial z}+\left(\frac{1+\nu}{2R_o}\right)\frac{\partial^2 v}{\partial z \partial \psi}=\frac{\partial^2 u}{\partial t^2}\left(\frac{1}{c_p^2}\right) \tag{4.7}$$

$$\left(\frac{1-\nu}{2}\right)\frac{\partial^2 v}{\partial z^2}+\left(\frac{1}{{R_o}^2}\right)\frac{\partial^2 v}{\partial \psi^2}+\left(\frac{1}{{R_o}^2}\right)\frac{\partial w}{\partial \psi}+\left(\frac{1+\nu}{2R_o}\right)\frac{\partial^2 u}{\partial z \partial \psi}=\frac{\partial^2 v}{\partial t^2}\left(\frac{1}{c_p^2}\right) \tag{4.8}$$

$$-\left\{\left(\frac{\nu}{R_o}\right)\frac{\partial u}{\partial z}+\left(\frac{1}{{R_o}^2}\right)\frac{\partial u}{\partial \psi}+\left(\frac{1}{{R_o}^2}\right)w\right\}-\frac{t}{12}^2\left\{\frac{\partial^4 w}{\partial z^4}+\left(\frac{2}{{R_o}^2}\right)\frac{\partial^4 w}{\partial z^2\partial\psi^2}+\left(\frac{1}{{R_o}^4}\right)\frac{\partial^4 w}{\partial\psi^4}\right\} = \frac{(1-\nu^2)\rho}{E}\frac{\partial^2 w}{\partial t^2} \tag{4.9}$$

where c_p refers to the dilatational plate velocity. Dilatational velocity refers to the propagation speed of a disturbed wave. It is evaluated using the equation

$$c_p = \sqrt{\frac{\mu}{\rho}\left(\frac{k+1}{k-1}\right)} \tag{4.10}$$

where k is given by $\frac{3-\upsilon}{1+\upsilon}$, μ is given by $\frac{E}{2(1+\upsilon)}$ and 'ρ' is the density of the thin plate. Substituting the values of 'k' and 'μ', the value of $c_p = \sqrt{\frac{E}{(1-\upsilon^2)\rho}}$. This dilatational plate velocity depends on the material properties such as elastic modulus, Poisson's ratio and the density of the material.

In order to find out a non-trivial solution of these equations of motion, the determinant of the coefficients must vanish:

$$\begin{vmatrix} -\Omega^2+k_m^2{R_o}^2+\frac{1}{2}(1-\nu)n^2 & \frac{1}{2}(1+\nu)nk_mR_o & \nu k_mR_o \\ \frac{1}{2}(1+\nu)nk_mR_o & -\Omega^2+\frac{1}{2}(1-\nu)k_m^2{R_o}^2+n^2 & n \\ \nu k_mR_o & n & -\Omega^2+1+\left\{\frac{t^2}{12}\left(k_m^2+\frac{n^2}{{R_o}^2}\right)^2\right\} \end{vmatrix} = 0 \tag{4.11}$$

where $\Omega = \frac{\omega R_o}{c_p}$

Solving the determinant, the equation is formulated as

$$\begin{aligned}(\Omega^2)^3 &- \left\{1+\left(\frac{3-\nu}{2}\right)\left(k_m^2{R_o}^2+n^2\right)+\beta^2\left(k_m^2{R_o}^2+n^2\right)^2\right\}(\Omega^2)^2 \\ &+\left\{\left(\frac{1-\nu}{2}\right)\left[\left(k_m^2{R_o}^2+n^2\right)^2+n^2+(3+2\nu)k_m^2{R_o}^2\right]\right. \\ &\left.+\beta^2\left(\frac{3-\nu}{2}\right)\left(k_m^2{R_o}^2+n^2\right)^3\right\}(\Omega^2) \\ &-\left\{\left(\frac{1-\nu}{2}\right)\left[(1-\nu^2)k_m^4{R_o}^4+\beta^2\left(k_m^2{R_o}^2+n^2\right)^4\right]\right\}=0\end{aligned} \tag{4.12}$$

where $\beta^2 = {t_s}^2 / 12{R_o}^2$

The equation is in the form of a cubic equation in Ω^2

$$(\Omega^2)^3 - A_2(\Omega^2)^2 + A_1(\Omega^2) - A_o = 0, \tag{4.13}$$

where the coefficients A_o, A_1, and A_2 are:

$$A_o = \left(\frac{1-\nu}{2}\right)\left[(1-\nu^2)k_m^4 {R_o}^4 + \beta^2\left(k_m^2 {R_o}^2 + n^2\right)^4\right], \tag{4.14}$$

$$A_1 = \left(\frac{1-\nu}{2}\right)\left[\left(k_m^2 {R_o}^2 + n^2\right)^2 + n^2 + (3+2\nu)k_m^2 {R_o}^2\right] + \beta^2\left(\frac{3-\nu}{2}\right)\left(k_m^2 {R_o}^2 + n^2\right)^3 \tag{4.15}$$

$$A_2 = 1 + \left(\frac{3-\nu}{2}\right)\left(k_m^2 {R_o}^2 + n^2\right) + \beta^2\left(k_m^2 {R_o}^2 + n^2\right)^2. \tag{4.16}$$

For $n > 0$, the solution of Eq. (4.13) thus gives us a set of three natural frequencies corresponding to each modal configuration.

4.4.2. Cylindrical shell with a simply supported boundary conditions

Consider a cylinder shell of length L that is simply supported at its ends, $z = \pm L$. For the modes whose radial displacement w is symmetric with respect to z and ψ, the modal configuration is given by Eq. (4.7), Eq. (4.8), and Eq. (4.9) with:

$$k_m = (2m+1)\frac{\pi}{2L}, \quad m = 0,1,2, \dots \dots \tag{4.17}$$

The variation of three real and positive natural frequencies obtained using Eq. (4.13) can be plotted w.r.t. circumferential mode number (n) as shown in Fig. (4.8).

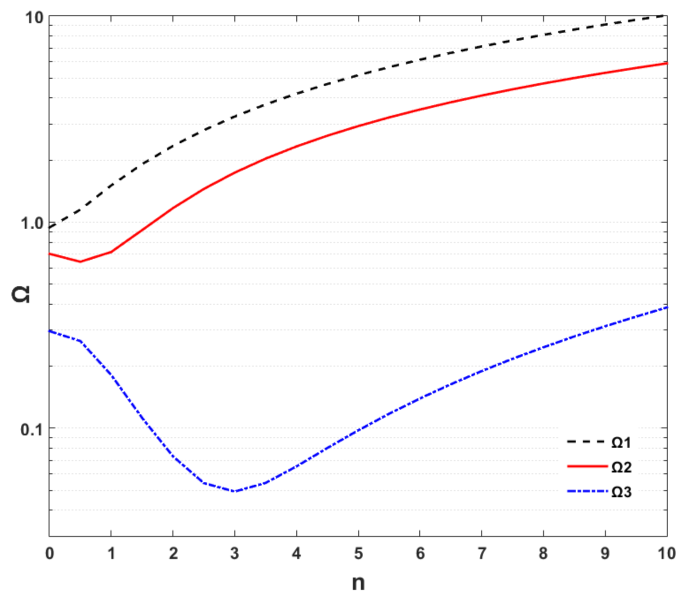

Figure 4.8 Non-dimensional frequency parameter as a function of circumferential mode number

The above curve shows the non-dimensional frequency parameter of a finite cylindrical shell with simply supported ends with respect to the circumferential mode number. The two upper branch frequencies increase monotonically with n, while the lower branch, which corresponds to predominantly radial modes, shows the somewhat unexpected result of the frequency initially decreasing with n and then increasing.

The location of the natural-frequency minimum can be identified analytically by means of an approximated expressions constructed by Heckl [140], which ignores the tangential inertial forces. The approximate expressions for the natural frequencies of predominantly radial modes becomes

$$\Omega_{mn} \approx \left[(1-\nu^2)\frac{k_m^4}{k_h^4} + \beta^2 k_h^4 R_o^4\right]^{\frac{1}{2}} (1+n^{-2})^{-\frac{1}{2}}, \qquad n > 0 \tag{4.18}$$

where k_h is the helical wave number

$$k_h = \left(k_m^2 + \frac{n^2}{{R_o}^2}\right)^{1/2} \tag{4.19}$$

Setting the derivative of Eq. (4.18) with respect to n equal to zero, one can solve for:

$$n_{min} \cong \left(\frac{k_m R_o}{\beta^{1/2}} - k_m^2 R_o^2\right)^{1/2} \tag{4.20}$$

The radial drive point admittance 'Y_s' is the series of modal admittance which peaks at the lower natural frequencies of the predominantly radial family of the three families of modes of a cylindrical shell. These resonances are identified by the circumferential wavenumber (k_c) given by, $k_c = \frac{n}{R_o}$ where n is the mode number ($1 \leq n \leq 5$) and R_o is the radius of the outer cylindrical shell. The corresponding frequencies are in the mid-frequency range. Vibrations in cylindrical shell are compared with that of a flat plate i.e. if the edges of the plate are wrapped around a circle to form a cylinder, the travelling flexural waves in the plate shall resemble with the waves travelling along the axis of a cylindrical shell. Moreover, at the low frequency response, the pipe mobility can be approximated with infinite beam mobility. As the frequency parameter further increases, the cylindrical shell mobility approaches that of a flat plate without curvature. Therefore, in order to evaluate the dynamic response of a cylindrical shell in terms of noise factor, the admittance of an infinite flat plate structure (Y_p) is considered as the reference point [141]. The approximate calculation of the driving point admittance 'Y_s' is quite cumbersome. The drive-point admittance for a finite shell can be computed as:

$$\mathrm{Re}\{Y_s\} = \left[4\pi R_o \rho_s t_s \sqrt{\frac{\Omega c_p^2}{\sqrt{2}}}\right]^{-1}, for\ \Omega < 0.77\frac{t_s}{R_o}, \tag{4.21}$$

$$\mathrm{Re}\{Y_s\} = \frac{0.66}{2.3 c_p \rho_s {t_s}^2}\sqrt{\Omega}, for\ 0.77\frac{t_s}{R_o} < \Omega < 0.6 \tag{4.22}$$

4.5. Sound spectrum for a concentric cylindrical shell

Since both vibration and sound measurements go from extremely low levels to extremely high levels, a logarithmic scale is often a logical choice for the representation of the amplitude of the power quantities. To this end, the decibel for a power quantity has been devised [142]. The decibel is defined as:

$$\mathrm{dB} = 10\log\left[\frac{Power\ Quantity}{Reference\ Power\ Quantity}\right] \tag{4.23}$$

It is necessary to have reference amplitude because of the nature of logarithms. The logarithmic scale for evaluating the decibel level depends on whether the measured parameter is power quantity or a field quantity.

For a field quantity, the ratio of the parameter should be expressed as the square of the measured field quantity. Hence, the decibel level can be written as:

$$\mathrm{dB} = 10\log\left[\frac{Field\ quantity^2}{Reference\ Field\ Quantity^2}\right] = 20\log\left[\frac{Field\ Quantity}{Reference\ Field\ Quantity}\right] \tag{4.24}$$

4.5.1. Force spectrum for the shell

The impact force calculated on the shell is a periodic function which repeats itself every 'τ' seconds. In order to determine the frequency of the function, the time domain force function has been converted into frequency domain function using Fourier transformation equation. The general Fourier transformation equation [143] is given as

$$\emptyset(\omega) = \int_{-\infty}^{\infty} g(t) e^{At} dt \tag{4.25}$$

where

$$g(t) = \sin\left(\frac{\pi t}{\tau}\right); A = i\omega \tag{4.26}$$

The $\sin\left(\frac{\pi t}{\tau}\right)$ is a semi-sinusoidal time dependent deceleration during the time interval [0,τ]. ω denotes the vibration frequency of the system and is evaluated by considering the excitation time period of 1 second. The Fourier transform of the normalized deceleration is:

$$\emptyset(\omega) = \int_0^\tau \sin\left(\frac{\pi t}{\tau}\right) e^{i\omega t} dt \tag{4.27}$$

The solution to the Eq. (4.27) is given as [126]

$$\emptyset(\omega) = \frac{e^{i\omega t}(i\omega \sin\left(\frac{\pi t}{\tau}\right) - \frac{\pi}{\tau}\cos\left(\frac{\pi t}{\tau}\right))}{\frac{\pi^2}{\tau^2} + (i\omega)^2} \tag{4.28}$$

Taking the definite integral of the Eq. (4.28) from 0 to τ, the formulation is

$$\Rightarrow \emptyset(\omega) = \left[\frac{e^{i\omega t}(i\omega \sin\left(\frac{\pi t}{\tau}\right) - \frac{\pi}{\tau}\cos\left(\frac{\pi t}{\tau}\right))}{\frac{\pi^2}{\tau^2} + (i\omega)^2}\right]_0^\tau \tag{4.29}$$

$$\emptyset(\omega) = \frac{2\pi\tau\cos(\frac{\omega\tau}{2})}{\pi^2 - \omega^2\tau^2} e^{i\omega\tau/2} \tag{4.30}$$

Taking the absolute value of the Eq. (4.30),

$$|\emptyset(\omega)| = \frac{2\pi\tau\left|\cos(\frac{\omega\tau}{2})\right|}{|\pi^2 - \omega^2\tau^2|} \tag{4.31}$$

$$\cong \frac{2\tau}{\pi}; \left(\frac{\omega\tau}{\pi}\right)^2 \ll 1 \tag{4.32}$$

In the concentric cylindrical shell, there are two shells one around the other. Outer concentric shell is referred as Outer Shell while the inner concentric shell is referred as Inner Shell.

4.5.1.1Outer shell

The force is applied in the vertical direction due to impact on the cylindrical surface. This force is resolved into two components, radial force (F_R) and tangential force (F_T). The components of forces are shown in Fig. (4.9).

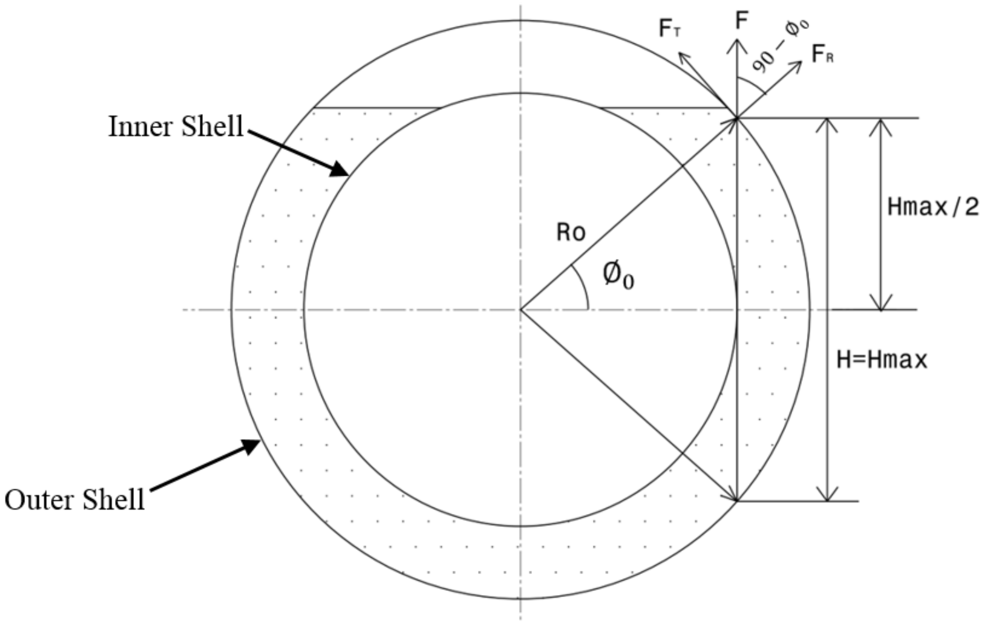

Figure 4.9 Radial force on the outer shell

For computing the force spectrum of the generated force on the cylindrical shell it is necessary to determine the radial force which is given by:

$$F_R = Fsin\emptyset_0 \tag{4.33}$$

Substituting the value of F (Section 3.6), the radial force is

$$F_R = MK_D\emptyset(t)sin\emptyset_0 \tag{4.34}$$

Eq. (4.34) is written in a frequency domain function as:

$$F_R = MK_D\emptyset(\omega)sin\emptyset_0 \tag{4.35}$$

Substituting the value of φ(ω) from Eq. (4.32) to the Eq. (4.35) gives:

$$F_R = MK_D\left(\frac{2\tau}{\pi}\right)sin\emptyset_0 \tag{4.36}$$

Replacing the value of K_D from Eq. (3.77) in the Eq. (4.36), the equation is

$$F_R = Mv(t)\left(\frac{\pi}{2\tau}\right)\left(\frac{2\tau}{\pi}\right)sin\emptyset_0 \tag{4.37}$$

$$F_R = Mv(t)sin\emptyset_0 \tag{4.38}$$

For outer shell,

$$sin\emptyset_0 = \frac{H_{max}}{2R_0} \tag{4.39}$$

The value of radial force in frequency domain for the outer shell is

$$|F_R(\omega)| = \frac{Mv(t)H_{max}}{2R_0}, \qquad \omega^2\tau^2 \ll \pi^2 \tag{4.40}$$

The maximum radial force is shown but this force changes with respect to the height. The height travelled by the bubble is maximum for the outer shell.

4.5.1.2Inner shell

For the inner shell, the radial force is shown in the Fig. (4.10).

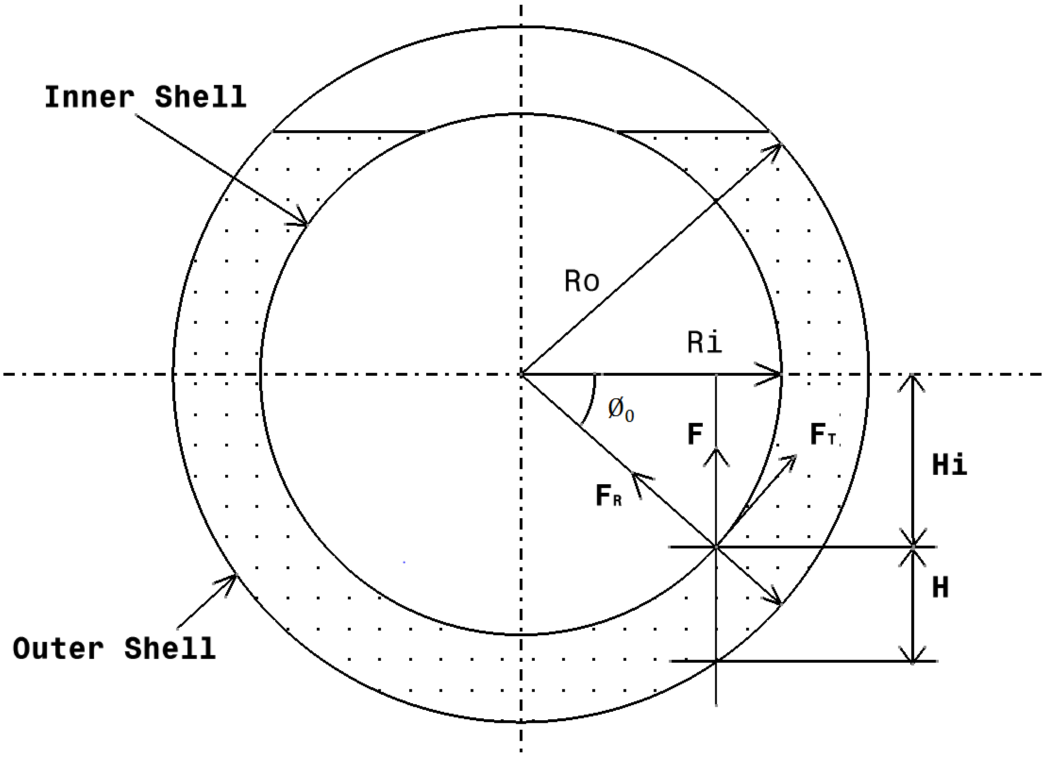

Figure 4.10 Radial force on the inner shell

The value of the angle is obtained as

$$sin\emptyset_0 = \frac{H_i}{R_i} \tag{4.41}$$

where Hi is the height from the impact point to the center of the cylinder, H is the height travelled by the bubble before striking. Hence the radial force on the inner cylinder is

$$|F_R(\omega)| = \frac{Mv(t)H_i}{R_i}, \qquad \omega^2\tau^2 \ll \pi^2 \tag{4.42}$$

4.5.2. Acceleration spectrum for the shell

The induced radial force on account of the bubble impact on the cylindrical shell has a major effect in determining the acceleration spectrum. Using the concept of mechanical admittance [81], the shell admittance can be appropriately formulated in terms of radial drive point velocity and the radial harmonic force. The equation for the shell admittance (Y_s) is given by:

$$Y_s(\omega) = \frac{\dot{w}(\omega)}{F_R(\omega)}, \tag{4.43}$$

$$\dot{w}(\omega) = Y_s(\omega)F_R(\omega) \tag{4.44}$$

where $\dot{w}(\omega)$ is the radial drive point velocity and $F_R(\omega)$ is the radial harmonic force.

The angular frequency of any object is evaluated by taking its absolute value of the angular velocity. Therefore the radial acceleration can be written as the product of radial velocity and the angular frequency.

Hence the corresponding radial acceleration becomes:

$$|\ddot{w}(\omega)| = \omega|Y_s(\omega)F_R(\omega)| \tag{4.45}$$

On plotting the curve between $20\ log\left|\frac{Y_s}{Y_p}\right|$ and Ω, an approximate expression is obtained for evaluating the admittance in the low frequency range at a particular value of t/R_o and $L/2R_o$. The curve corresponds to the relation between the admittance of a pipe of finite length and admittance of an infinite flexural thin plate. The equation for the approximate curve in Fig. (4.11) can be written as:

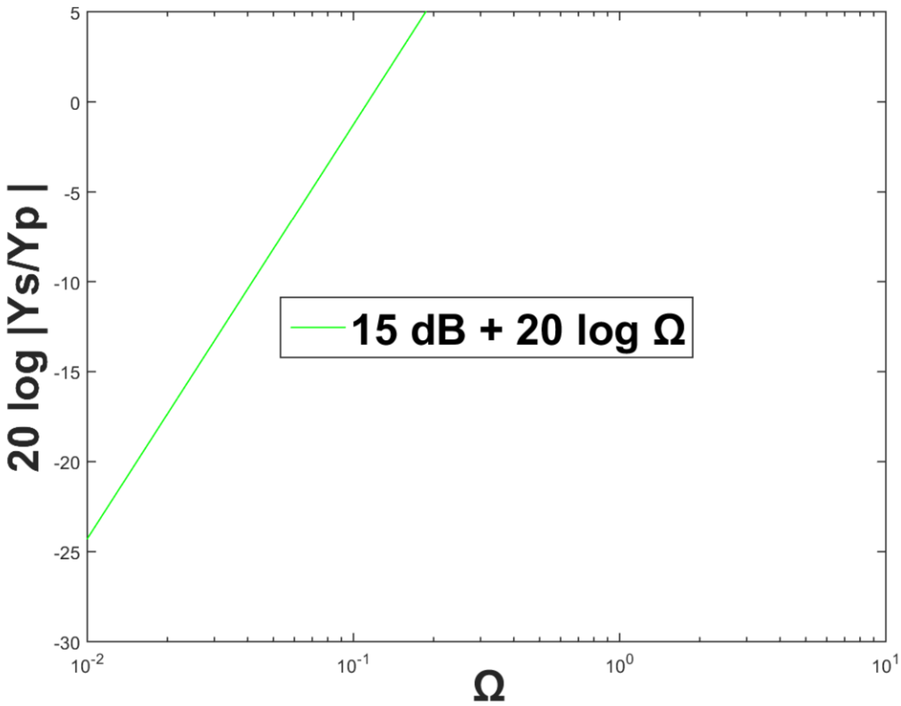

Figure 4.11 Approximate curve for the relation between the ratio of dynamic response and the frequency parameter in low-frequency region

The non-dimensional frequency parameter (Ω) is formulated in terms of the dilatational plate velocity (c_p = 5.4 x 10^5 cm/s for steel and aluminum). Here, Y_p is the admittance of an infinite plate of the same material and thickness as the shell. Driving point mobility for an infinite flexural thin plate with wave motion and force excitation is given by:

$$Y_p = \frac{1}{8\sqrt{B_p \rho_s t_s}} \tag{4.46}$$

where ρ_s is the density of the plate material, B_p is the bending stiffness of the flexural plate which is calculated as:

$$B_p = \frac{E {t_s}^3}{12(1-\upsilon^2)} \tag{4.47}$$

where E is Young's Modulus of the plate material and υ is the Poisson's ratio. Substituting the value of B_p from Eq. (4.47) in Eq. (4.46), we get:

$$Y_p = \frac{\sqrt{3}}{4{t_s}^2\sqrt{\frac{E}{(1-\upsilon^2)}\rho_s}} \tag{4.48}$$

The dilatational plate/wave velocity is:

$$c_p = \sqrt{\frac{k+1}{k-1}}c_s \tag{4.49}$$

where $c_s = \sqrt{\frac{\mu}{\rho_s}}$, and $k = \frac{3-\upsilon}{1+\upsilon}$, putting the value of k and Cs in the Eq. (4.49), the equation is:

$$c_p\sqrt{\rho_s} = \sqrt{\frac{E}{(1-\upsilon^2)}} \tag{4.50}$$

Substituting the Eq. (4.50) in Eq. (4.48), the value of plate admittance is,

$$Y_p = \frac{\sqrt{3}}{4\rho_s c_p {t_s}^2} \tag{4.51}$$

In the low-frequency range, the simply supported shell can, therefore, be modelled as a spring of stiffness:

$$k_s = \frac{\omega}{|Y_s|} \tag{4.52}$$

The acceleration spectrum level (L_{acc}) of the cylindrical shell is formulated using convolution theorem. From Eq. (4.45), the spectrum level generated by N bubble per second colliding with the shell is:

$$|\ddot{w}(\omega)| = \omega|Y_s(\omega)F_R(\omega)|N \tag{4.53}$$

By applying convolution theorem, the R.H.S. term of Eq. (4.53) is written as:

$$|\ddot{w}(\omega)| = 2\pi\omega|Y_s(\omega)F_R(\omega)|N \tag{4.54}$$

To determine the acceleration spectrum level in terms of a sound parameter, the logarithmic scale is applied on both sides of the Eq. (4.54). Therefore the spectrum level is expressed as:

$$L_{acc} dB\ re\ (cm/s^2)^2/Hz = 20\log 2\pi\omega|Y_s(\omega)F_R(\omega)| + 10\log N \tag{4.55}$$

4.5.3. Velocity spectrum for the shell

For estimating the velocity spectrum level (L_{vel}), the radial drive point velocity is written as:

$$|\dot{w}(\omega)| = |Y_s(\omega)F_R(\omega)| \tag{4.56}$$

Therefore on applying convolution theorem and logarithmic scale to the Eq. (4.56), the sound level (in dB) is expressed as:

$$L_{vel} dB\ re\ (cm/s)^2/Hz = 20\log 2\pi|Y_s(\omega)F_R(\omega)| + 10\log N \tag{4.57}$$

4.5.4. Displacement spectrum for the shell

To compute the displacement spectrum level (L_{disp}), the radial displacement is written as:

$$|w(\omega)| = \frac{\omega|Y_s(\omega)F_R(\omega)|}{\omega^2} \tag{4.58}$$

Applying convolution theorem and logarithmic scale to the Eq. (4.58), the sound level (in dB) is expressed as:

$$L_{disp} dB\ re(cm)^2/Hz = 20\log 2\pi\omega|Y_s(\omega)F_R(\omega)| - 40\log\omega + 10\log N \tag{4.59}$$

The value of N can be determined using the time scale factor and the time taken for one bubble to reach and collide with the outer shell.

4.6. Summary

The force, acceleration, velocity and displacement spectrum in the terms of dB is generalized for any type of the configuration. The force spectrum for the cylindrical shells is considered for both outer and inner shell. The acceleration, velocity and displacement spectrum will change as per the force spectrum. Noise is directly proportional to the vibrational amplitude. Noise is dependent on the number of bubbles striking. The general formulation has been derived.

Chapter 5

LN2 Cryopump Vibration and Noise

This chapter describes the circular concentric shell arrangement of LN_2 cryopump similar to actual cryopump and the necessary theoretical analysis for the involved dynamics and the bubble impact force and induced noises. The liquid nitrogen is taken as the working fluid. The bubble structure interaction has been analysed in detail. Also, a comparison chart has been drawn for the values obtained for the motion and bubble dynamics such as bubble terminal velocity, displacement, acceleration, departure diameter, bubble growth, generated forces and induced noise.

5.1. Cryopump configuration

The liquid nitrogen cryopump has many components. Reservoir is the main key component of the cryopump and it contains the liquid nitrogen fluid. LN_2 is a cryogenic fluid having boiling point of 80K and has violent behaviours at room temperature. As the fluid is exposed to the outer environment through the shell, abrupt boiling occurs due which various LN_2 bubble rise and collapse after the interaction with the surrounding surface. Due to the continuous rise and collapse, the cylindrical shells start experiencing random vibration/noise which is quiet detrimental to the data obtained from Gravitational Waves.

The issue of bubble-induced vibration necessitates the analysis of cryopump reservoir and the required dimensional requirements for its low vibration and noise working environment. However, this analysis is quiet cumbersome to carry out in an actual cryopump due to issues involving space, cost etc.

Therefore, the present chapter deals with the design and analysis of the actual reservoir configuration of an LN_2 cryopump for studying the effects of bubble dynamics in the resulting noise/vibration. The reservoir is surrounded by the cryostat to maintain the vacuum around the reservoir as shown in Fig. (5.15.2).

Figure 5.1 Liquid Nitrogen cryopump (Courtesy-LIGO-USA)

The reservoir of actual cryopump design consists of two concentric hollow steel cylinders with a specific annular gap between them. The ends of the cylinders are connected and covered with a steel cap which has a provision for the liquid nitrogen (LN_2) inlet and outlet as shown in Fig. (5.2).

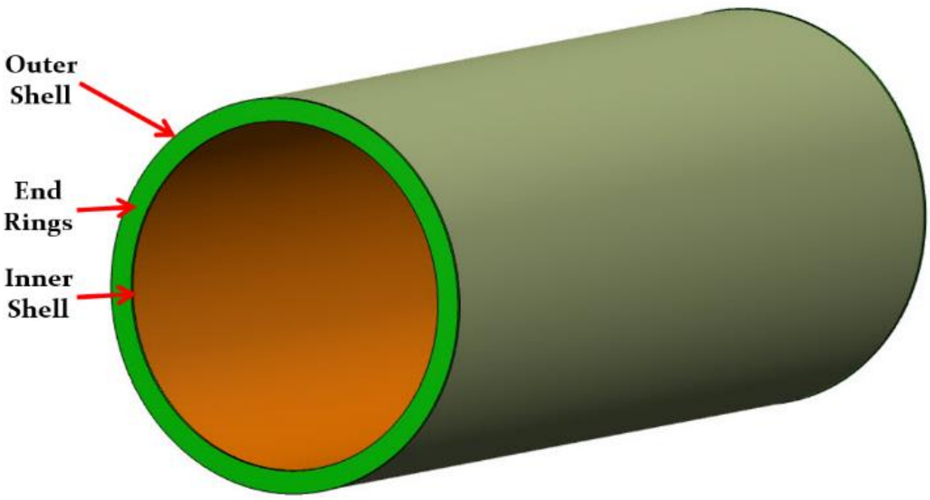

Figure 5.2 Isometric view of liquid nitrogen cryopump

Due to the concentric circular design of the cryopump, the bubble travelling distance 'H' varies before striking the inner shell or outer shell. This variation in the travelling distance effects the dynamics, induced forces, vibration and noise parameters in a significant manner. Other factors are also important for the bubble induced vibration and noise like thickness of shell, number of bubble striking etc.

The important parameters for the cryopump configuration are described in the Fig. (5.3).

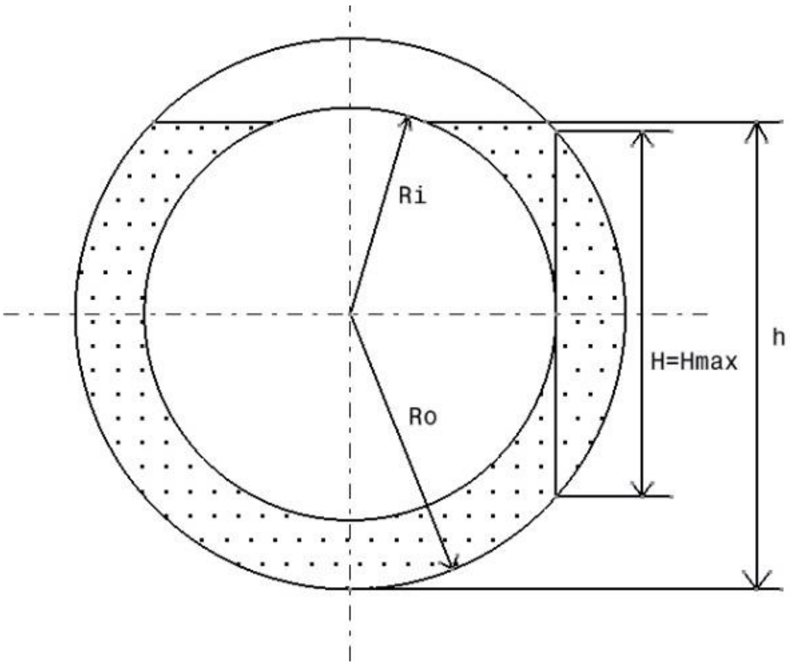

Figure 5.3 Front view of the LN2 cryopump with important parameters

where Ri and Ro are the outer radius of the inner shell and inner radius of the outer shell respectively, h is the fluid level inside the cryopump, H is the height travelled by the bubble before striking to the outer shell, Hmax is the maximum height travelled by the bubble within the cryopump.

5.2. Parameters of the cryopump

The liquid nitrogen pump is made up of the SS material (SA-240) due to cryogenic and vacuum requirements. The fluid is liquid nitrogen for the cryo pumping purpose to maintain the Ultra High Vacuum (UHV). The cryopump works at 77.3 K due to the boiling point of liquid nitrogen at atmospheric pressure.

The different parameters for the fluid, material etc. are shown in the Table (5.1), Table (5.2), Table (5.3) and Table (5.4):

Table 5.1 Fluid (LN2) properties

S. No.	Properties	Magnitude	Units
1	Density of fluid (ρ_L)	806.6	kg/m^3
2	Density of gas (ρ_G)	4.624	kg/m^3
3	Dynamic viscosity of fluid (μ_L)	0.0001579	N.sec/m^2
4	Surface tension of fluid (σ)	0.008823	N/m
5	Latent heat of fluid (h_{lv})	198800	J/kg
6	Specific heat of fluid (c_{pl})	2042	J/kg.K
7	Thermal conductivity @ b.p (K)	0.1375	W/m.K
8	Temperature difference (ΔT=Tw-Tsat)	5	K
9	Saturation Temperature (T_{sat})	77.3	K
10	Thermal diffusivity (α_L)	8.34 x 10^{-8}	m^2/sec

Table 5.2 Material (SS 304L) properties

Sr. No.	Properties	Magnitude	Units
1	Density	7952	Kg/m3
2	Yield Strength	240	MPa
3	Ultimate Tensile Strength	620	MPa
4	Young’s Modulus	200	GPa
5	Poisson ratio	0.27	-

Table 5.3 Dimensional (cryopump) parameters

S. No.	Parameter	Magnitude	Units
1	Length of the Cylindrical Shells	2.000	m
2	Inner Radius of the Outer Shell (Ro)	0.550	m
3	Outer Radius of the Inner Shell (Ri)	0.500	m
4	Annular Gap between Cylindrical Shells	0.050	m

Table 5.4 Buble (spherical) parameters

S. No.	Parameter	Magnitude	Units
1	Bubble contact angle (γ)	45	degree
2	Advancing angle (α)	55	degree
3	Receding angle (β)	35	degree
4	Surface Bubble contact Diameter	0.09	mm
5	Inclination Angle (θ_i)	π/18	radian

These parameters are used for the theoretical investigation and analysis of cryopump.

5.3. Bubble departure diameter

In order to analyze the bubble dynamics, the liquid nitrogen vapour bubble diameter is found out by the Jeongbae Kim and Moo Hwan Kim [113] correlation. This correlation is related with the liquid nitrogen, hence the bubble departure diameter (d_b):

$$\mathrm{d}_b = \frac{0.1649 Ja^{0.7}}{\sqrt{\frac{(\rho_L - \rho_G)}{\sigma}}} \tag{5.1}$$

$$and\ Ja = \frac{\rho_L C_{pl}(T_w - T_{sat})}{\rho_G h_{lv}} \tag{5.2}$$

Using the fluid parameters for the liquid nitrogen as stated in Table (5.1), the bubble departure diameter for the liquid nitrogen is 2.5 mm. This diameter is used in all the subsequent analysis.

5.4. Bubble dynamics

Bubble dynamics provides the bubble departure force responsible to detach from the surface and the initial acceleration of bubble.

5.4.1. Forces during bubble departure

In the case of nucleate boiling, the forces in the vertical direction are responsible for bubble departure because the flow of the liquid nitrogen in the cryopump is quasi-static. These vertical direction forces are shown in the Fig. (5.4).

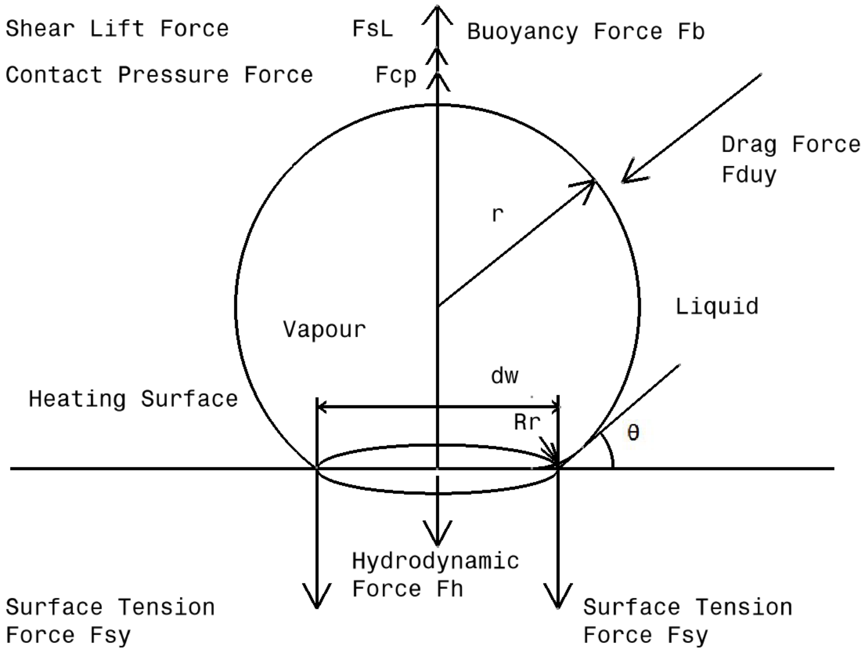

Figure 5.4 Forces acting on a single spherical bubble in vertical direction

The net force acting on the detaching bubble in the vertical direction is:

$$\sum F = F_b + F_{sL} + F_{cp} + F_h + F_{sy} + F_{duy} \tag{5.3}$$

The bubble force is the function of bubble radius. Hence for the analysis purpose, the variation of different forces as per the bubble departure radius of the bubble are plotted.

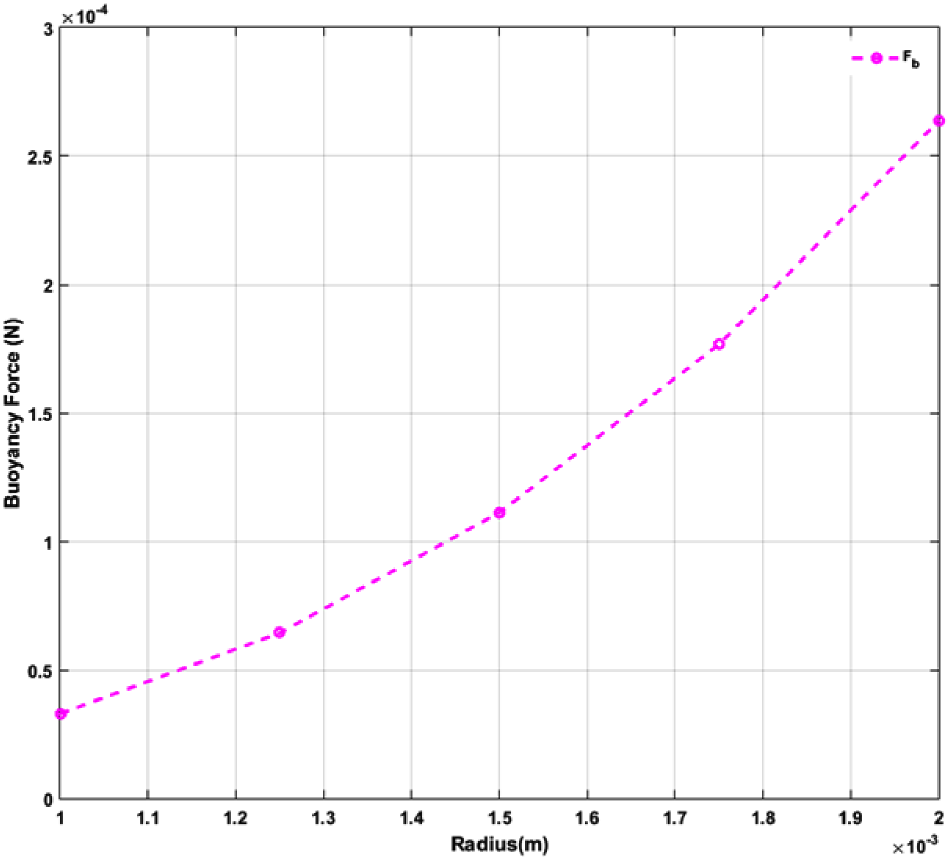

Figure 5.5 Buoyancy force with variation in bubble radius

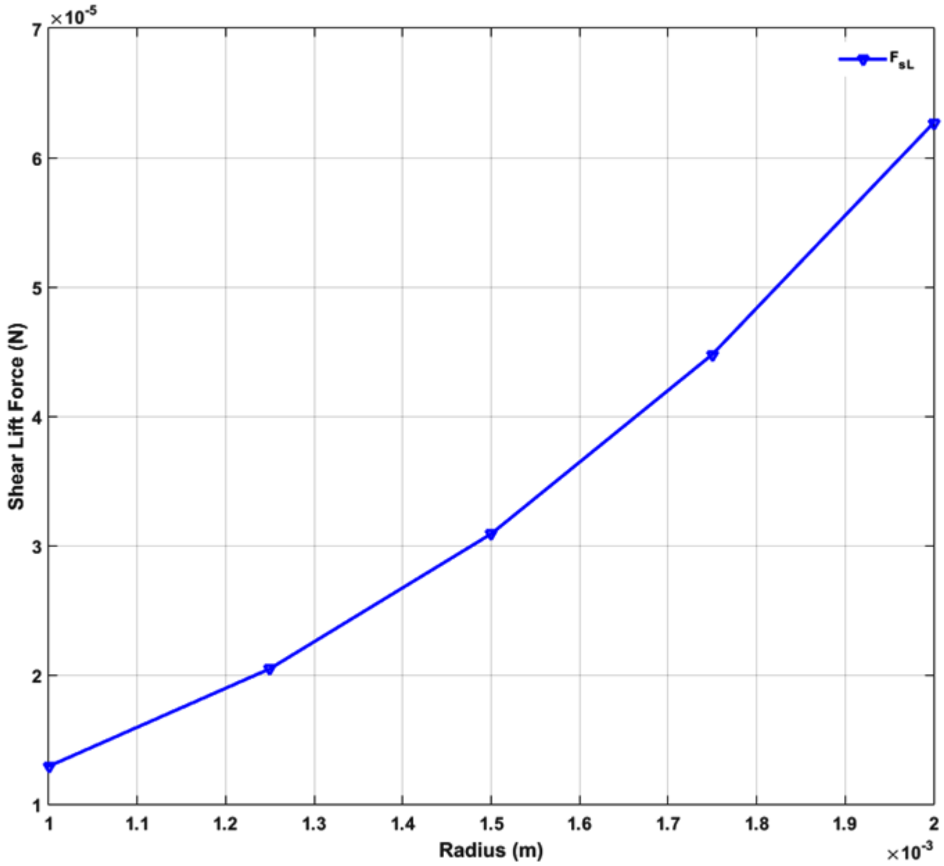

Figure 5.6 Shear Lift force with variation in bubble radius

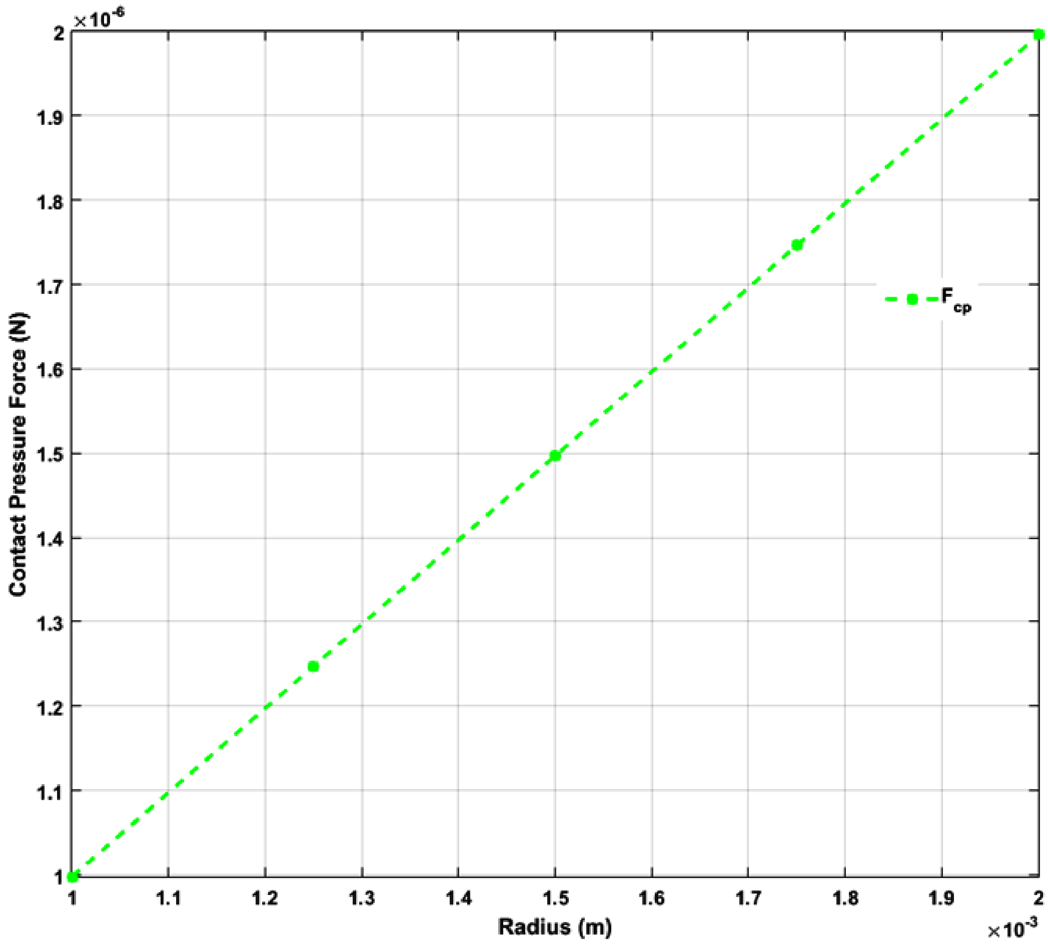

Figure 5.7 Contact pressure force with variation in bubble radius

The buoyancy force (Fig. (5.5)) varies as cubic power of bubble radius, shear lift force (Fig. (5.6)) varies as quadratic power of bubble radius and contact pressure force (Fig. (5.7)) varies proportional to the bubble radius. Buoyancy force varies from 0.35×10^{-4} to 2.6×10^{-4} N. The shear lift force varies from 1.2×10^{-5} to 7×10^{-5} N. The magnitude range for the contact pressure force is from 1×10^{-6} to 2×10^{-6} N for the bubble radius of 1 to 2 mm. The shear lift force is ~10 order less than the buoyancy force similarly contact pressure force is ~10 order less than the shear lift force.

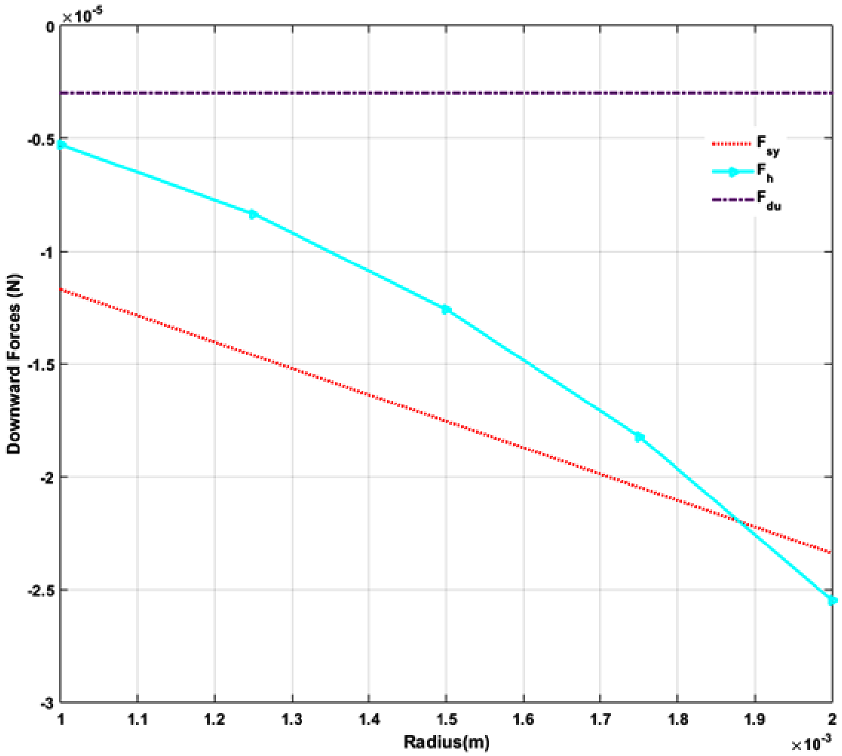

Figure 5.8 Surface tension, Hydrodynamic and Drag force with variation in bubble radius

All the downward forces (Surface tension, Hydrodynamic, and Unsteady drag force) are in the range of 10^{-5} N (Fig. (5.8)). The forces increase in the negative direction with the increase of bubble radius while the drag force remains almost constant.

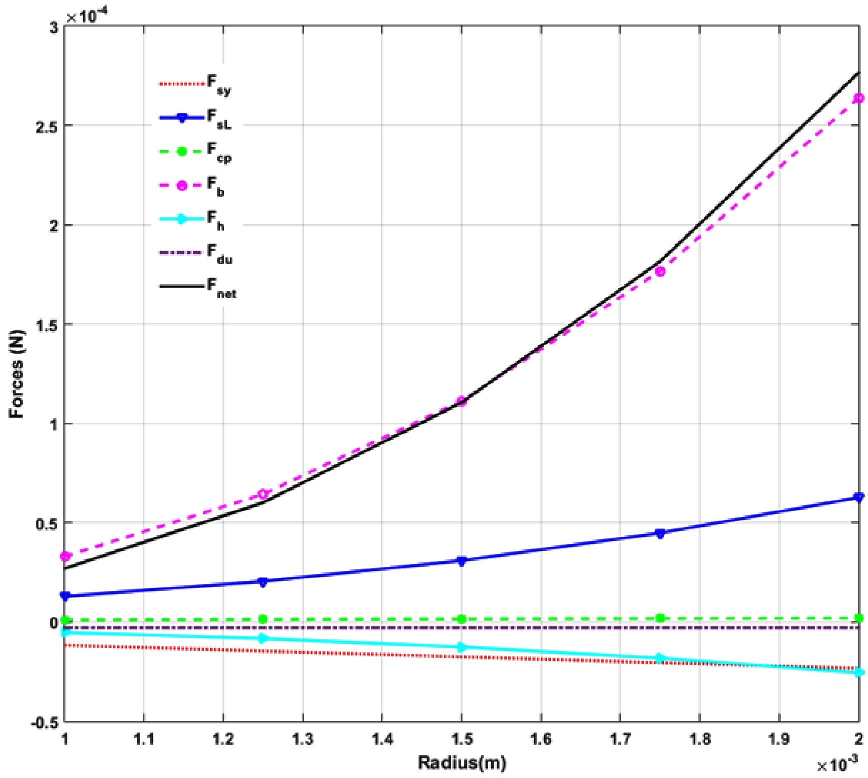

Figure 5.9 Net force (F_{net}) with variation in bubble radius

Net departure force (Fig. (5.9)) is almost equal to the buoyancy force and increases with the increase of bubble radius. The buoyancy force is dominating till the bubble radius of 1.5 mm. After that, the downward forces comes into effect and decreases the net force by a small magnitude.

The bubble of spherical in shape and of diameter 2.5 mm is considered for evaluating all the forces. The magnitude of all the forces along the vertical direction is shown in the Table (5.5):

Table 5.5 Forces in the vertical direction (upward and downward)

Sr. No.	Type of force	Force (N)
1	Buoyancy force (F_b)	6.432 x 10^{-5}
2	Shear lift force (F_{sL})	2.046 x 10^{-5}
3	Contact pressure force (F_{cp})	0.125 x 10^{-5}
4	Hydrodynamic force (F_h)	- 0.835 x 10^{-5}
5	Surface tension force (F_{sy})	-1.462 x 10^{-5}
6	Unsteady drag force (F_{du})	- 0.299 x 10^{-5}
	Total force	6.007 x 10^{-5}

The net force for the 2.5 mm bubble diameter is 6.01×10^{-5} N.

5.4.2. Initial acceleration of bubble

The unbalanced net force ($\sum F$) in the y-direction of 6.01×10^{-5} N is responsible to produce the initial acceleration in the bubble. The mass of the bubble is the entrained mass with the bubble and can be written as

$$M_e = \rho_L \left(\frac{2}{3}\pi r^3\right) \tag{5.4}$$

The entrained mass of the liquid nitrogen bubble is calculated as $3.29 \times 10^{-6}\ kg$. The intitial acceleration of the bubble is also function of bubble radius and varies as per the Fig. (5.10).

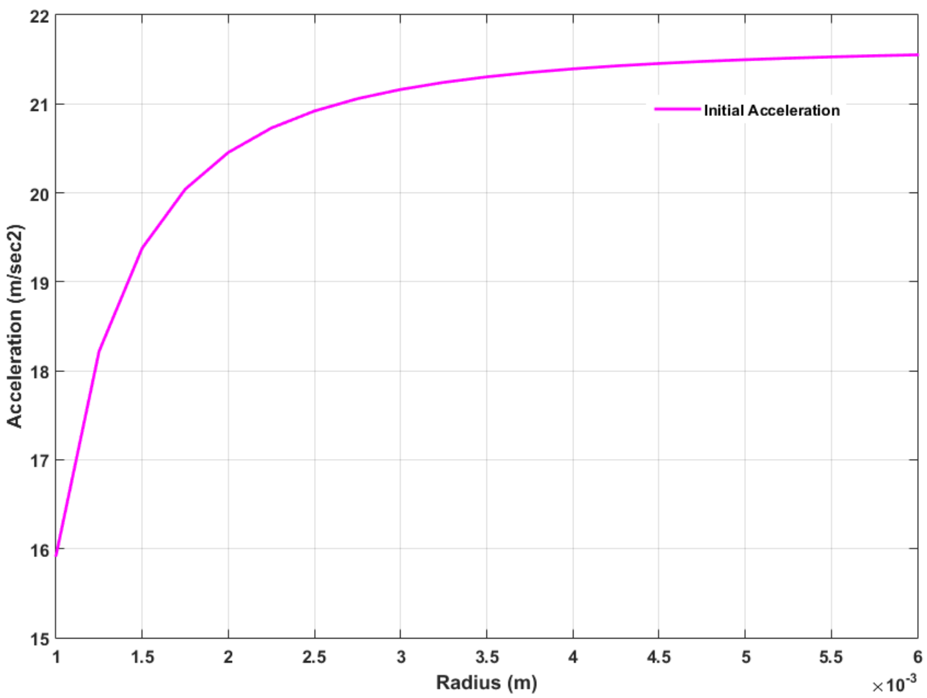

Figure 5.10 Initial acceleration of bubble with respect to bubble radius

From the Fig. (5.10), it is clearly stated that with the increase in bubble radius the entrained mass increases. Since acceleration is dependent on the bubble radius, hence the bubble acceleration also increases with increase in bubble radius. For the bubble radius from 1 to 6 mm, the acceleration varies from 1.64 g to 2.14 g. For the bubble radius of 1.25 mm, the initial acceleration is found to be 2g.

As per the Leighton [123] also, the ratio of displaced mass is the twice of the entrained mass, which provides the initial bubble size-independent acceleration as 2g.

5.5. Bubble acceleration, velocity, and displacement with time

The spherical bubble starts moving within the fluid with the initial acceleration of 2g for the liquid nitrogen fluid. This is the general bubble acceleration (Section 3.5.6) without having any geometrical constraints. The acceleration decreases due to the resistance provided by the fluid. The bubble acceleration with respect to time is shown in the Fig. (5.11).

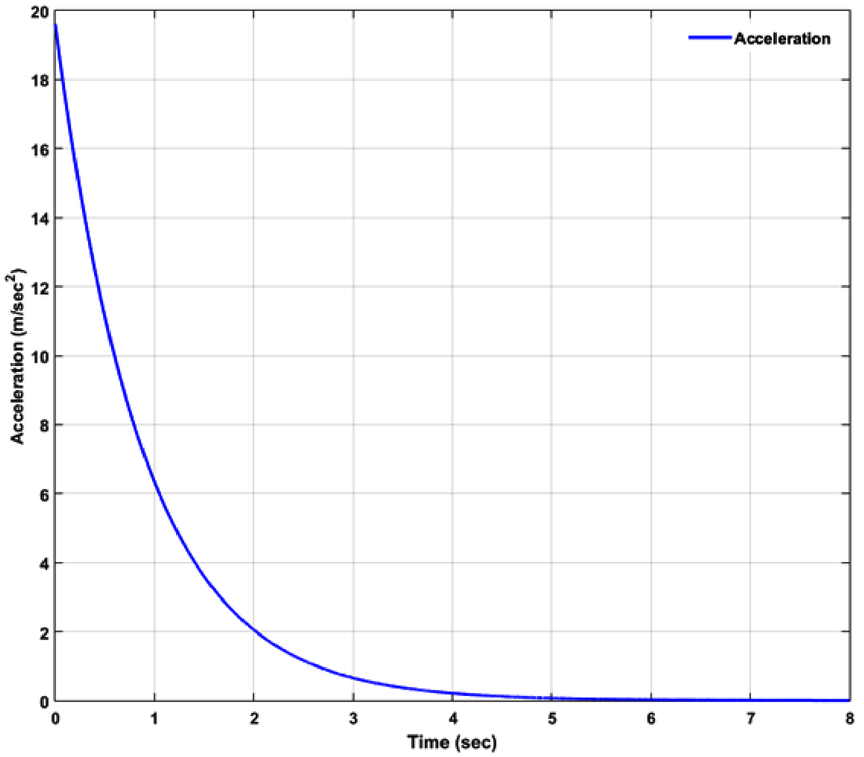

Figure 5.11 Acceleration of bubble with respect to time during the motion within the fluid

The Fig. (5.11) shows that the acceleration is continuously decreasing and becomes almost zero after 5 sec. The velocity variation is shown in Fig. (5.12):

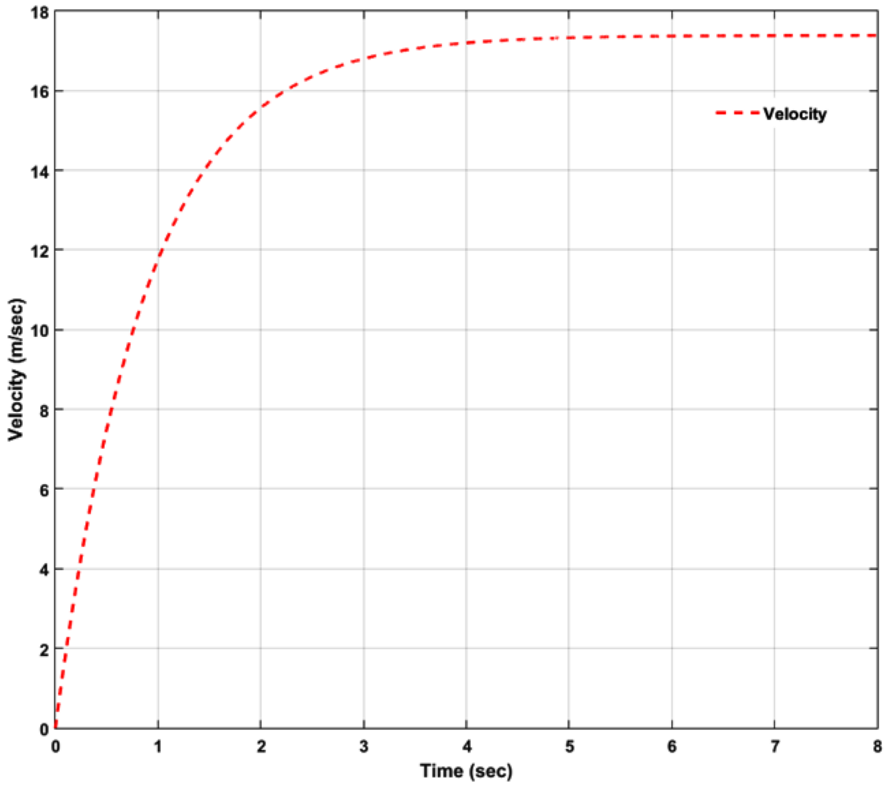

Figure 5.12 Velocity of bubble with respect to time during the motion within the fluid

As the velocity reaches its terminal velocity then it becomes almost constant for the further motion. The liquid nitrogen bubble reaches the terminal velocity of 17.2 m/sec after 5 sec. The bubble motion parameters with the displacement is shown in the Fig. (5.13).

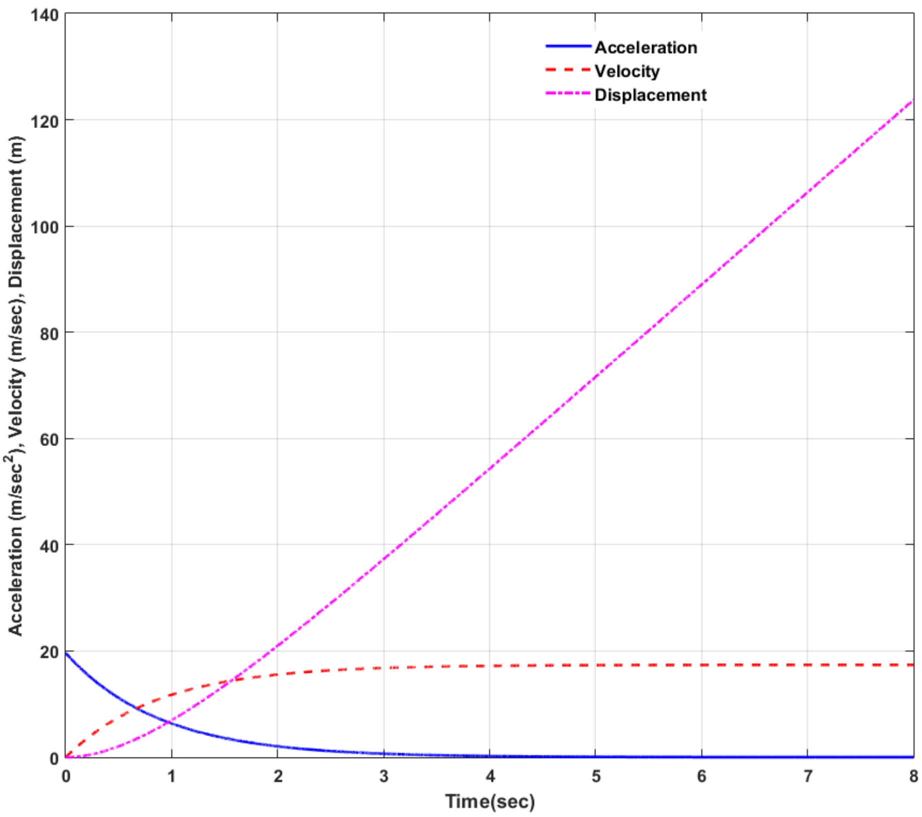

Figure 5.13 Bubble motion parameters with respect to time during the motion within the fluid

According to the Fig. (5.13) , the displacement required (80m) is too high to reach its terminal velocity. Hence in the case of liquid nitrogen cryopump, the bubble will not impact the cylindrical shell with the terminal or maximum velocity.

5.5.1. Migration time and maximum height travel by LN2 bubble

The bubble motion characteristics changes as the bubble migrates from early time zone to late time zone. Migration time is the time at which the bubble enters into the late time zone from early time zone. This migration time decides the bubble motion in the early time zone or the late time zone. The migration time for the liquid nitrogen bubble is calculated as 0.89 sec. The maximum height (Hmax, Fig. (4.9)), which a liquid nitrogen bubble can travel in the cryopump, is calculated as 0.5123 m. The travel time corresponding to the max. height travel is 0.24 sec. The travel time is quite less than the migration time. Hence the liquid nitrogen bubble will remain in the early time zone only.

5.5.2. Bubble velocity and displacement with time for LN2 cryopump

The bubble velocity and displacement will vary during the travel time of 0.24 sec, the variation is shown in the Fig. (5.14).

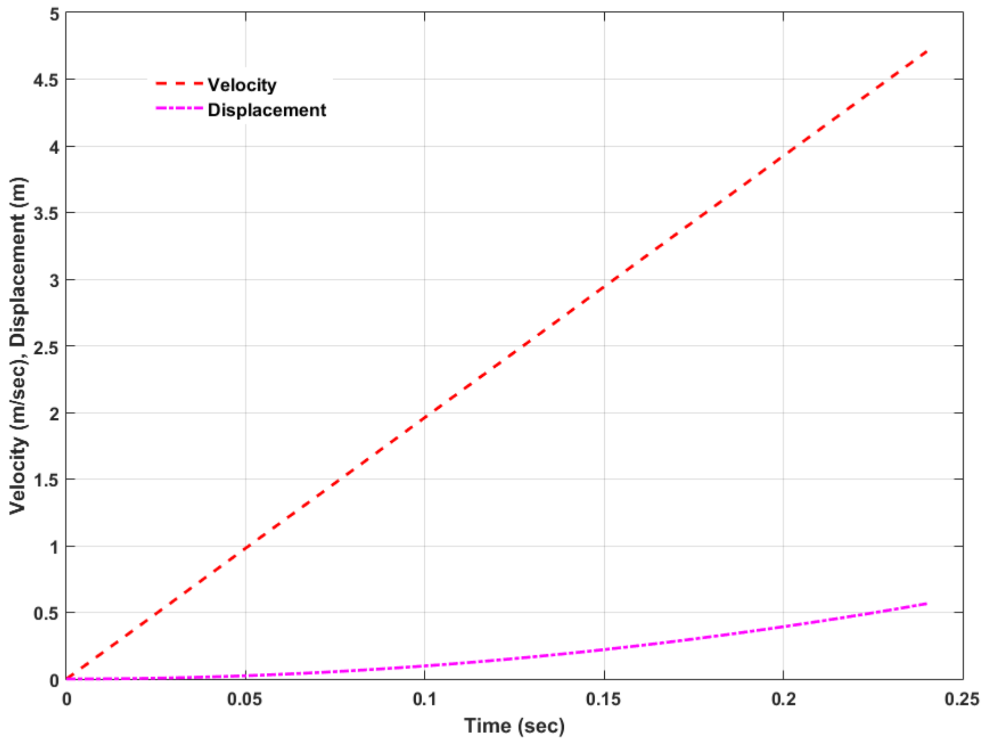

Figure 5.14 Bubble velocity and displacement with respect to time for LN2 cryopump

The liquid nitrogen bubble does not attain the terminal velocity during maximum travelling height available within the cryopump configuration. It strikes the outer surface with the maximum velocity of 4.67 m/sec after traveling maximum height of 0.5123 m.

Bubble motion provides the impact velocities with respect to the height travelled.

5.6. Impact force by the LN2 bubble

The impact force is dependent on the height travelled by the bubble and the impact velocity achieved. The height travelled will vary as per the cryopump configuration.

5.6.1. Height travelled by bubbles for impacting on inner shell

The height travel before impacting to the shells are different in the case of the inner shell and outer shell. The variation of height is calculated for both the shells.

5.6.1.1Impacting to inner shell

The variation in the radius ‘R’ across the inner shell of cryopump along X-direction is,

$$0 < R < R_i \ (0.689 \ m)$$

The variation of H with respect to R is shown in the Fig. (5.15),

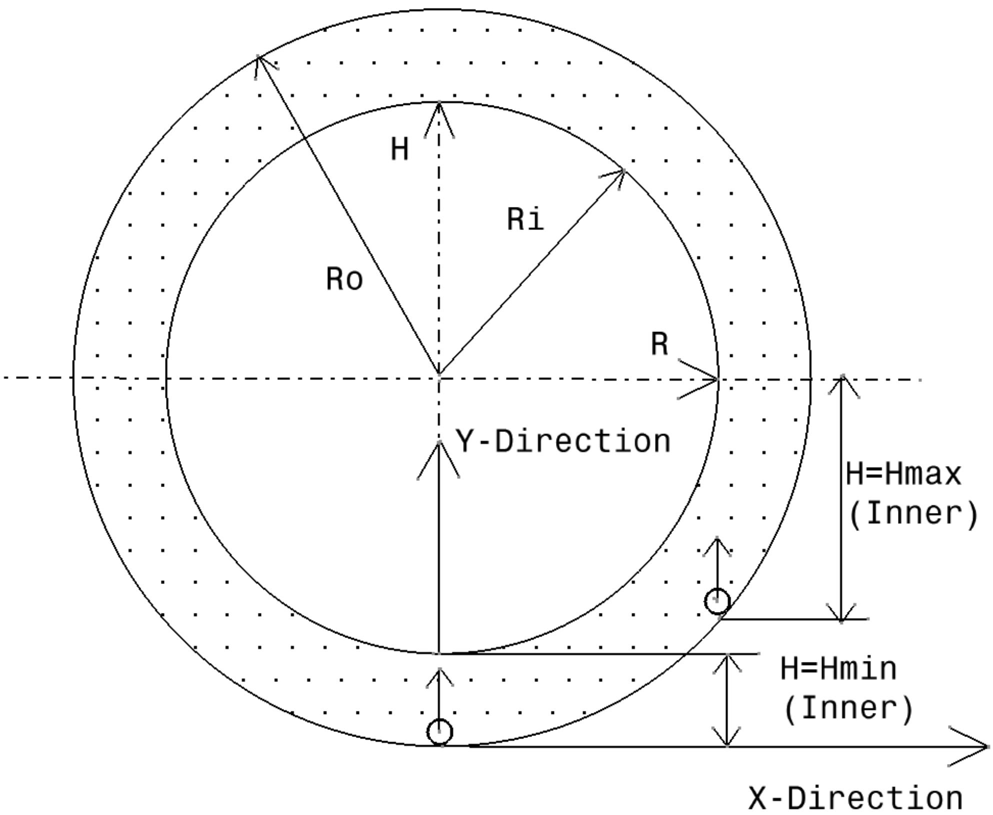

Figure 5.15 Height travelled by bubble before impacting to inner shell of LN2 cryopump

The height variation in Y-direction is formulated as

$$H = \sqrt{\left({R_o}^2 - R^2\right)} - \sqrt{\left({R_i}^2 - R^2\right)} \tag{5.5}$$

The minimum distance travelled in Y-direction by the bubble is at R=0 and is denoted as Hmin (Inner) and the maximum distance travelled by the bubble is at R=0.689 m and is denoted as Hmax (Inner).

5.6.1.2Impacting to outer shell

The variation in the radius 'R' across the outer shell of cryopump along X-direction is,

$$R_i\ (0.689\ m) < R < R_o\ (0.743\ m)$$

The variation of H with respect to R is shown in the Fig. (5.16);

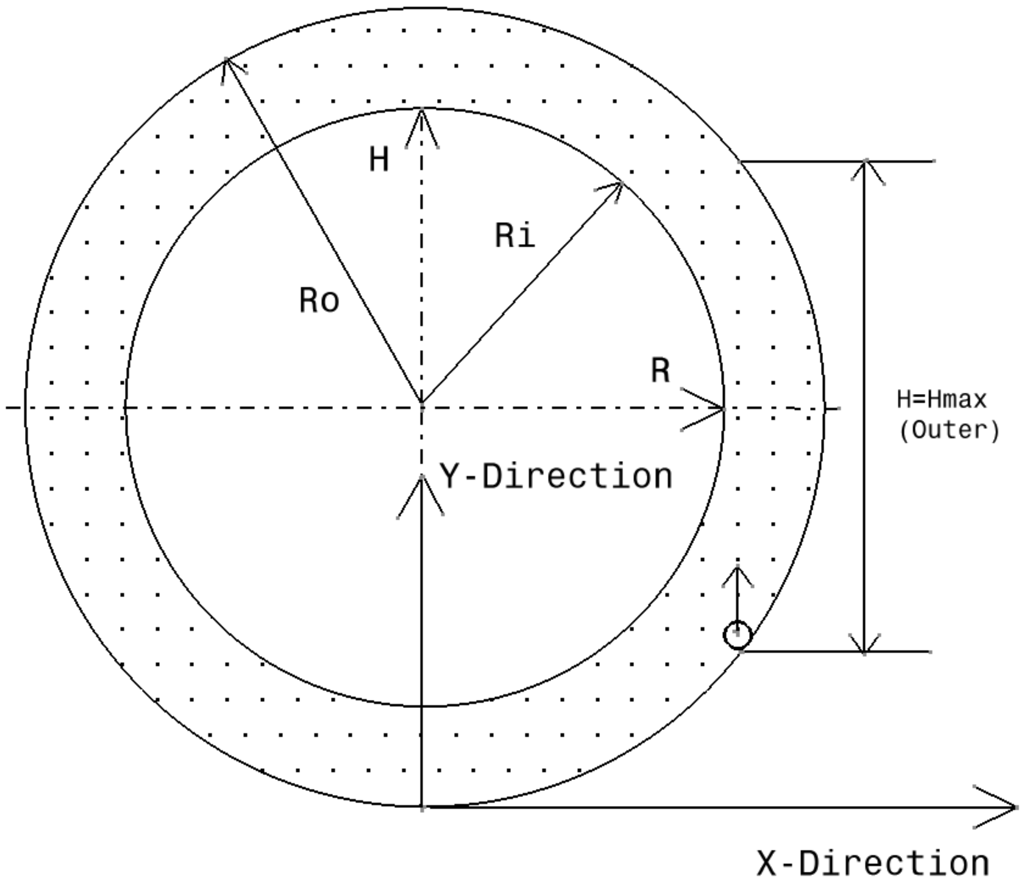

Figure 5.16 Height travelled by bubble before impacting to outer shell of LN2 cryopump

The height variation in Y-direction is formulated as

$$H = 2\sqrt{\left({R_o}^2 - R^2\right)} \tag{5.6}$$

The minimum distance travelled in Y-direction by the bubble is zero at R=0.743 m and the maximum distance travelled by the bubble is at R=0.689 m and is denoted as Hmax (Outer).

5.6.1.3Variation in height travelled by bubble

As per the Section 5.7.1.1 and Section 5.7.1.2, the travel height variation for the bubble before impacting to the inner shell and outer shell is shown in Fig. (5.17).

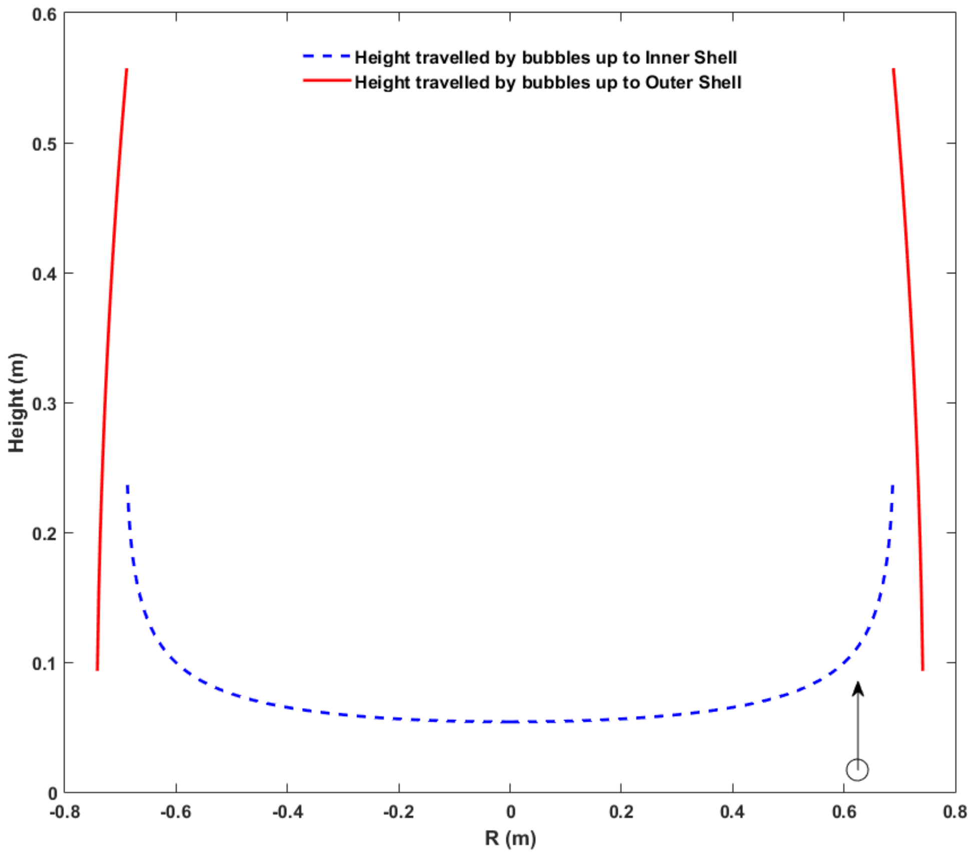

Figure 5.17 Height travelled by bubble before impacting shells of LN2 cryopump

The bubble travels from outer shell to inner shell between the R=0 to R=0.500 m and as soon as it crosses the R=0.500 m, it attains the maximum height and strikes the outer shell itself. Then the distance travelled reduces up to the R=0.550 m.

5.6.2. Impact force and impact velocity by bubble

The impact velocity is the function of the height travelled by the bubble. The impact velocity is shown in Fig. (5.18).

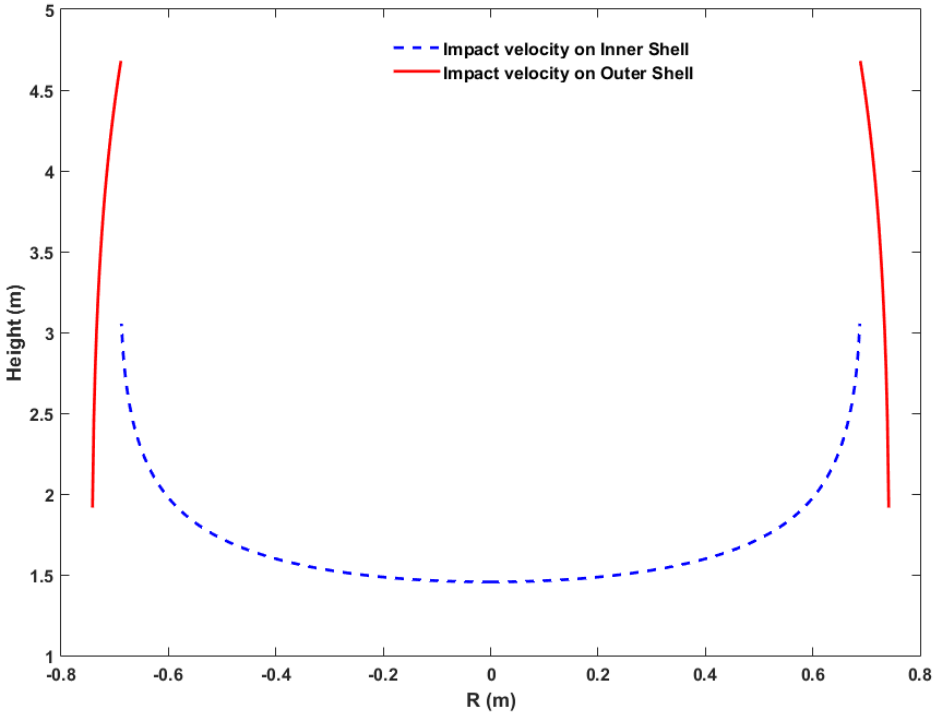

Figure 5.18 Velocity gained by bubble before impacting shells of LN2 cryopump

The impact force (Section 3.6) is also changed accordingly as shown in Fig. (5.19).

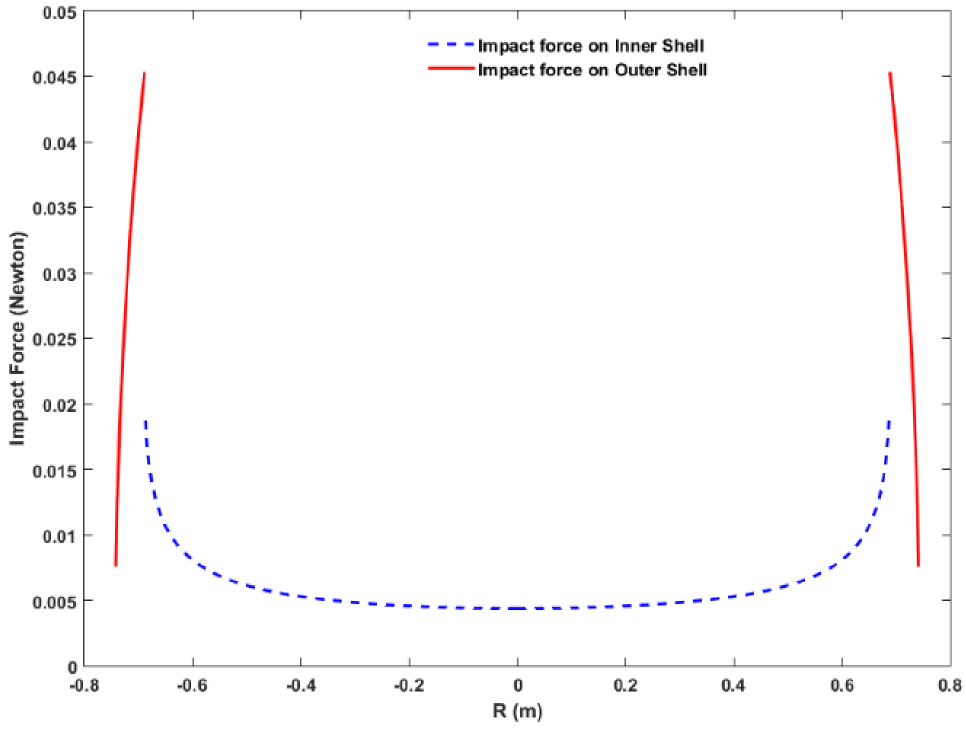

Figure 5.19 Impact force by bubble on shells of LN2 cryopump

The variation of the parameters for the bubbles striking to inner shell and outer shell are tabulated in Table (5.6):

Table 5.6 Height, Velocity, Time and Impact forces by bubble on shells of LN2 cryopump

Parameter	Inner Shell		Outer Shell	
	Min.	Max.	Min.	Max.
Height (m)	0.050	0.236	0.094	0.512
Impact Velocity (m/sec)	1.456	3.045	1.924	4.671
Travelling time (sec)	0.074	0.155	0.098	0.238
Impact force (N)	0.004	0.019	0.007	0.045

The impact force calculated is the force in time domain. The impact force varies from 0.004 N to 0.019 N for the inner shell and 0.007 to 0.045 N for the outer shell.

5.6.3. Total impact force on the shells

The total impact force on the cryopump across the one cross section of width equal to the bubble diameter is the sum of total impact force on the inner shell (F_{it}) and on the outer shell (F_{ot}). The impact force on the inner shell and outer shell is calculated according to the Fig. (5.19). The number of bubbles colliding to the shell's surface (N) at an instant is different for outer and inner shell. The number of bubbles colliding to the surface is calculated by dividing the radial distance (along X-direction) into equal parts of bubble's diameter.

The total force (F_t) generated on the shell is the arithmetic sum of all the individual forces obtained from each of the bubble colliding with the surface. Hence,

$$F_{it} = \sum_{n=1}^{Ni} F_{in} = 1.648\ Newtons \tag{5.7}$$

$$F_{ot} = \sum_{n=1}^{No} F_{on} = 0.679\ Newtons \tag{5.8}$$

where Ni and No are the number of bubbles striking the inner shell and outer shell respectively.

The total impact force on the LN2 cryopump is

$$F_t = F_{it} + F_{ot} \tag{5.9}$$

The magnitude of the total impact force (time domain) in the vertical direction is

2.317 N. The total impact force (1.648 N) on the inner shell is more than the total impact force (0.679 N) on the outer shell. This is due to the number of bubble striking on the inner shell are more than the outer shell, while the amplitude of force on the outer shell is higher than the inner shell.

5.7. Natural frequencies of mode shapes for cryopump

As per the requirement criteria, the natural frequency of the cryopump should not be below 100 Hz because it works as noise in the wave detection range below 100 Hz. The natural frequency depends on the thickness of the different shells. Hence, it is necessary to calculate the thickness of the shells for the inner and outer shell.

5.7.1. Thickness of inner and outer shell

The thickness of the inner shell and outer shell is calculated as per the ASME, Section VIII, and Division 1 code.

5.7.1.1Material for cryopump

The selection of materials for Vacuum and Cryogenic systems is a very important part of the design. The material must be capable of withstanding of structural load (for vacuum) and suitable to low temperature (for cryogenics).

On the basis of above requirement for a cryopump, the austenitic grade SS304L is suitable candidate material among other like; Aluminium, Inconel, titanium mild steel etc. SS304L material confirms the following,

- The requirement of ASME Specification SA-240 Type.
- The surface finish of the material smoother than 3 delta.

5.7.1.2Structural load:

As the Cryopump works in the vacuum environment, hence the major load is the pressure difference (ΔP) due to vacuum inside the chamber and atmosphere outside. The liquid nitrogen is filled at the atmospheric pressure between the annulus-space, as shown in Fig. (5.20)

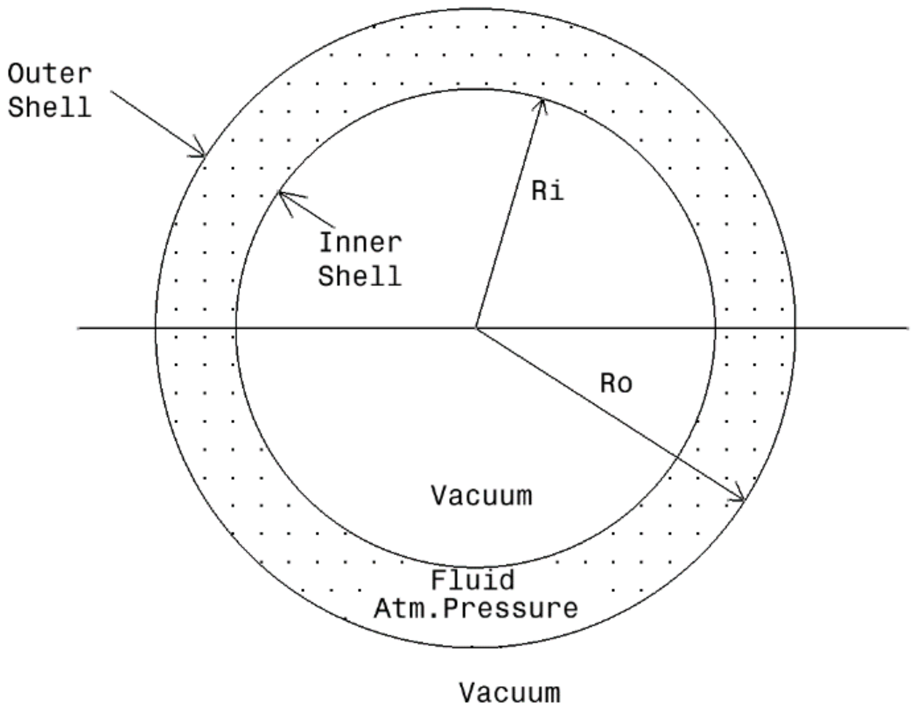

Figure 5.20 Pressure load condition on shells of LN2 cryopump

The inner shell is designed as per the external pressure vessel criteria because the inner shell is subjected to the atmospheric pressure from outside. The outer shell is designed as per the internal pressure vessel criteria because the outer shell is subjected to the atmospheric pressure from inside. The atmospheric pressure is taken as 1.01325 bar or 1.01325×10^{5} Pa.

5.7.1.3Inner shell thickness

The thickness is calculated as per the ASME, Part UG-28. The thickness is dependent on the length to diameter ratio and diameter to thickness ratio. Initially, the thickness is taken as 10 mm. Hence the length to diameter ratio is 2.0 and diameter to thickness ratio is 100. From the charts given in ASME code, the value of factor A is 0.0040 and factor B for the SS304L is 350 bar. The allowable pressure is calculated as

$$Pa = \frac{4\mathrm{B}}{3\ (\mathrm{D_{oi}}|\mathrm{t})} \tag{5.10}$$

where Pa is the allowable pressure. Pa is 3.66 bar for inner shell. The pressure is above the atmospheric pressure. Hence the designed thickness is taken as 10 mm.

The external pressure is checked for the buckling failure because the thickness of the inner shell is relatively small compared with the other dimensions. Elastic buckling is the decisive criteria in the design of thin-walled shells under external pressure, this mode of failure determines the wall thickness required. Buckling occurs when the working pressure difference (ΔP) exceeds the critical buckling pressure (P_{cr}). Hence the critical buckling pressure should be more than the atmospheric pressure for its safe operation. During buckling failure, the vessel can no longer retain its shape and suddenly irreversibly buckles to take new distorted shape [144].

The buckling failure determines the minimum wall thickness required. During the buckling failure, different lobes are formed in the shell at the point of buckling. The failure of the vessel forms two number of lobes, hence the critical buckling pressure for two number of lobes is considered. The critical buckling pressure is calculated as

$$\mathrm{Pcr} = \frac{2\mathrm{E}}{1-\nu^2}\left(\frac{\mathrm{t}}{\mathrm{D}}\right)^3 \tag{5.11}$$

where E is young's modulus of elasticity, ν is the Poisson's ratio, t and D are the thickness and diameter of the shell respectively.

The inner shell is prominent to fail due to buckling. The diameter of the inner shell is 1.378 m. Thickness of shell from the ASME code is 10 mm. Hence, the critical buckling pressure for the inner shell is 1.7 bar which is more than the 1.013 bar. The inner shell thickness is taken as 10 mm for further analysis.

5.7.1.4Outer shell thickness

The thickness is calculated as per the ASME, Part UG-27. The maximum allowable stress is taken as 120 MPa as per the UG-23. The joint efficiency is considered as 0.6 as per UW-12 because it is fabricated from the plate with the help of welding. The thickness is calculated as per the circumferential (tc) and longitudinal stress (tl) consideration and shown in Eq. (5.12) and Eq. (5.13)

$$tc = \frac{\mathrm{PR}}{S.E - 0.6P} \tag{5.12}$$

$$tl = \frac{\mathrm{PR}}{2SE + 0.4P} \tag{5.13}$$

The maximum value of thickness is 1.1 mm but for the fabrication point of view, the minimum value is 3 mm. Hence the outer shell thickness is taken as 3 mm.

5.7.2. Mode shape and natural frequencies

The mode shapes for the cylindrical shapes are lobes in nature when the circumferential mode number ‘n’ is greater than 1. Both the outer and inner shells are cylindrical in nature, hence outer shell is verified for the different mode shapes.

5.7.2.1Mode shapes for the outer shell

The mode shapes for the cylindrical shell is given in the Section 4.3.2 and it is verified from the ANSYS.

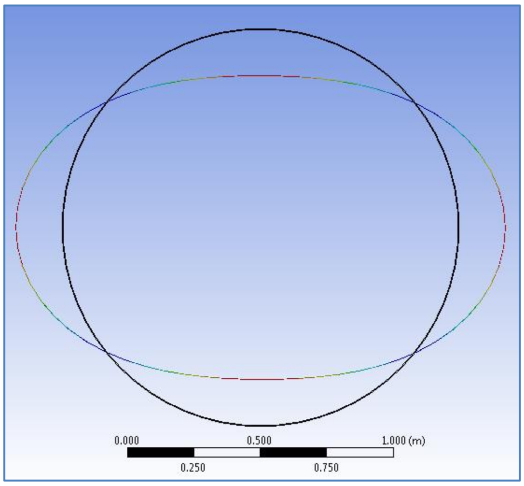

(a) n =2

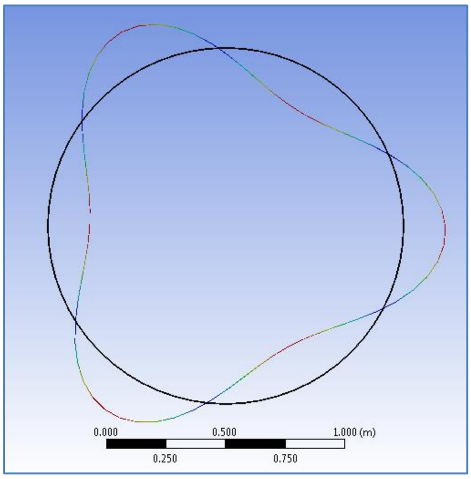

(b) n =3

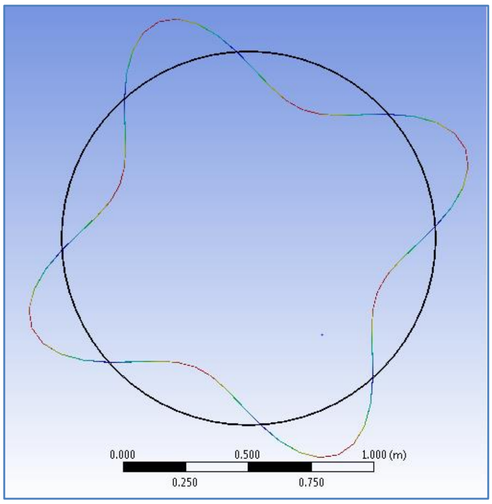

(c) n=4

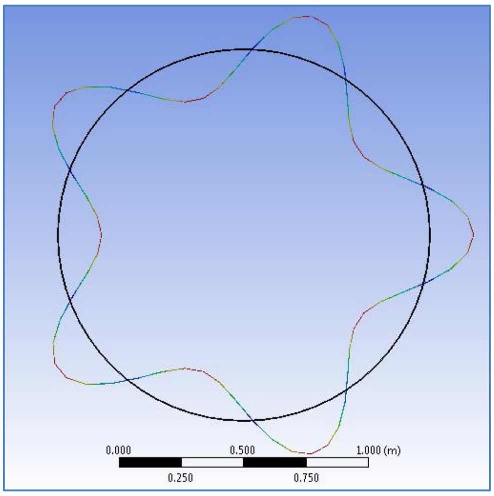

(d) n=5

Figure 5.21 Mode shapes for outer shell w.r.to circumferential mode number

The mode shapes (Fig. (5.21)) are same as per the circumferential mode numbers defined. The boundary condition is taken as free-free at both the ends.

5.7.2.2Natural frequencies of mode shapes for inner shell

The thickness of the inner shell is 10 mm hence the inner shell is modeled with thickness 10 mm. The ends of the shell are fixed-fixed as per the actual condition as shown in Fig. (5.22).

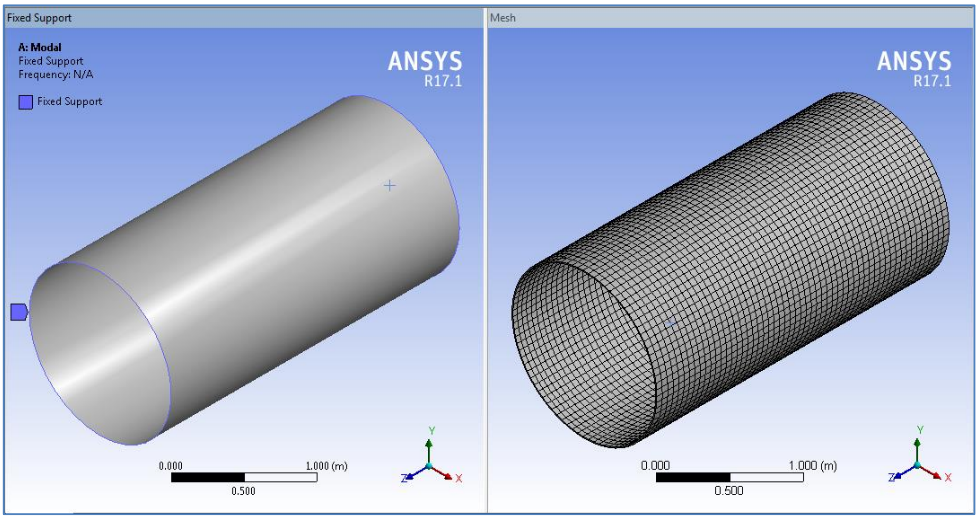

Figure 5.22 Inner shell with boundary condition and mesh

The inner shell is meshed with an element size of 5×10^{-2} m. The mesh has 4701 nodes and 4619 elements. The inner shell is analyzed for the different natural frequencies mode shapes. Twenty number of frequencies are extracted, which are given in the frequency chart (Fig. (5.23))

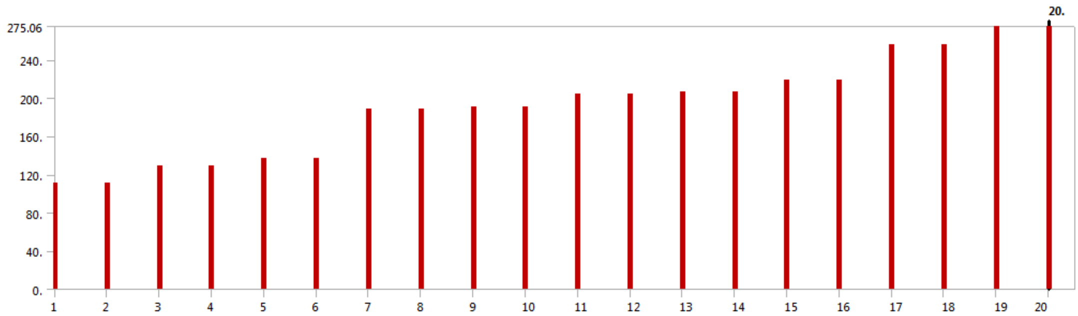

Figure 5.23 Natural frequency against the mode number for Inner Shell

The natural frequencies are summarized in the Table (5.7). The mode number does not represent the circumferential or axial mode number. It is the number of modes extracted during the analysis.

Table 5.7 Natural frequency with mode number for inner shell

Mode Number	1	2	3	4	5	6	7	8	9	10
Frequency(Hz)	111	129	137	188	191	204	206	218	255	275

From the frequency chart, the one frequency exists for two-mode numbers. The difference is in the circumferential rotation of the circumferential-mode shapes as shown in Fig. (5.24) for the frequency 111.

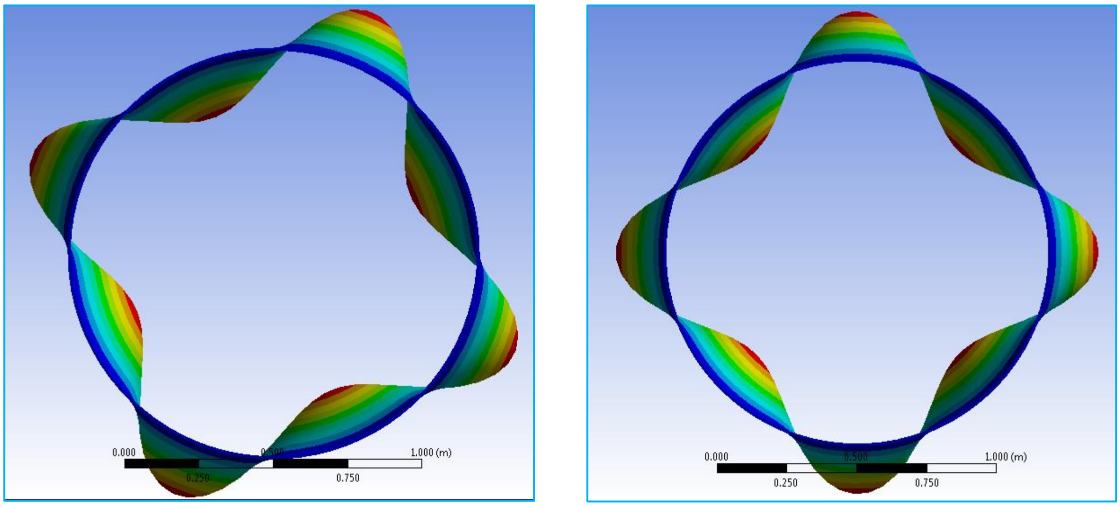

Figure 5.24 Two mode shapes at one frequency

Only one mode shape exist at one time but there are two possibilities as given in the Fig. (5.24).

The mode shapes are the function of the circumferential-mode number (n) and the axial mode number (m). This is the reason that different combination of the mode shapes exists in the non-planer vibration of the cylindrical shell. The Fig. (5.25) shows the mode shape for n=5 and n=6 with m=1

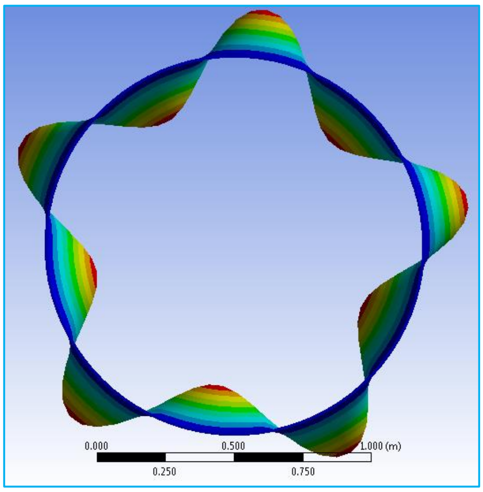

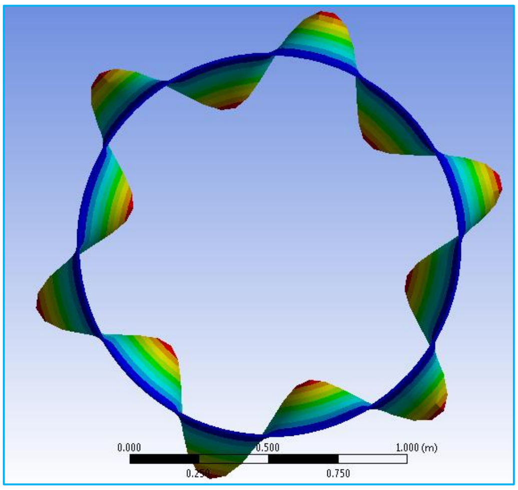

(a) Frequency = 137

(b) Frequency = 188

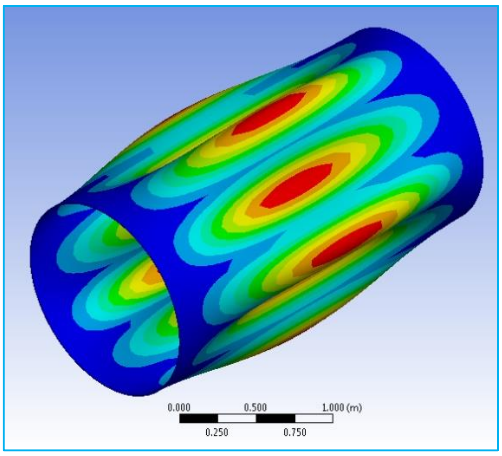

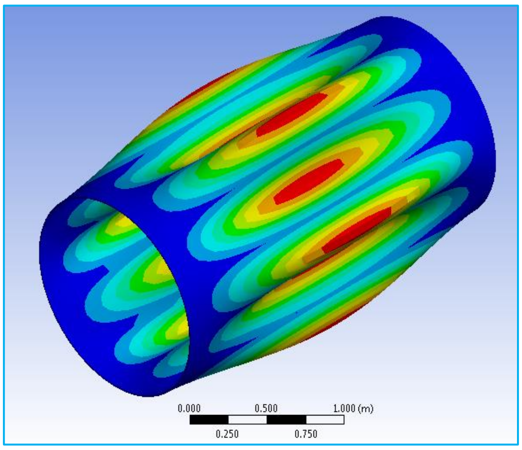

(c) Frequency = 137

(d) Frequency = 188

Figure 5.25 Mode shapes for inner shell for n=5 and 6 with m=1

From the Fig. (5.25) it is clear that the number of lobes is changing from 5 to 6 but the axial mode is almost same in behavior. But the frequency is different for both as 137 Hz and 188 Hz.

The axial mode changes the mode shape as shown in Fig. (5.26) for m=4 and n=2

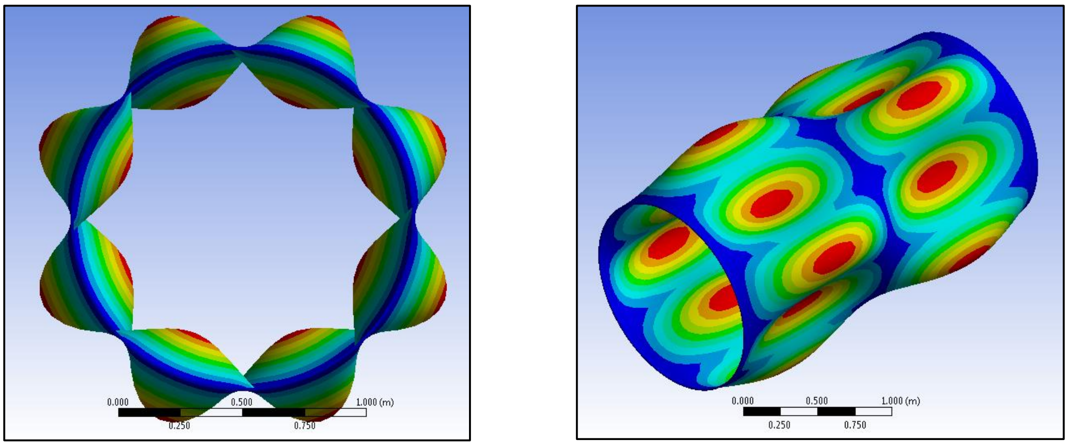

Figure 5.26 Mode shape for inner shell for n=4 and m=2

The Fig. (5.26) shows that first segment of axial mode will have rotation in the circumferential direction with respect to the second segment of axial mode. This is the reason to get the eight lobes in the front view of the shell. The frequency is changed to 206 Hz.

The change of frequency is shown in Fig. (5.27) for the same number of circular mode number i.e. n=5 with m=2.

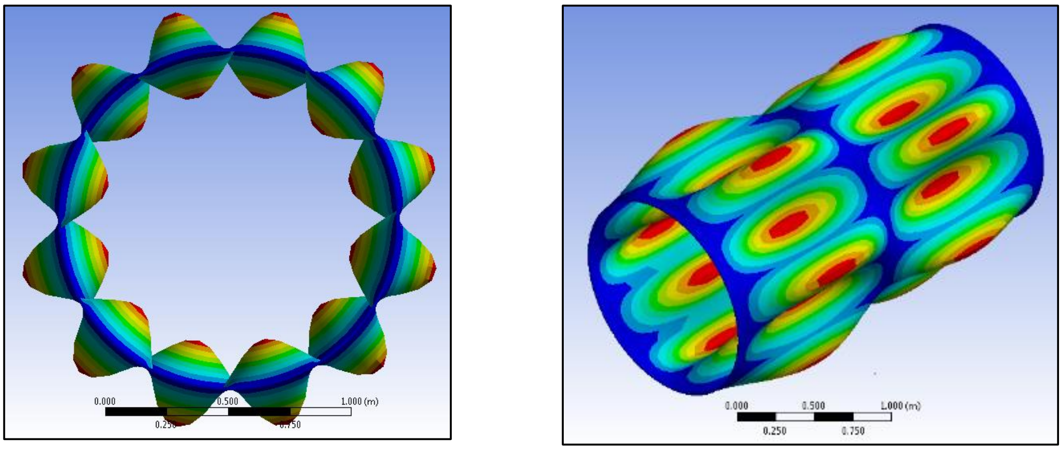

Figure 5.27 Mode shape for inner shell for n=5 and m=2

The Fig. (5.27) shows that natural frequency of the mode shape changed from 137 Hz (n=5, m=1, Fig. (5.25)) to 218 Hz (n=5, m=2, Fig. (5.27)).

5.7.2.3Analytical verification of natural frequencies for inner shell

As stated, the natural frequency is the function of circumferential mode number (n) and axial mode number (m). The approximate frequency is calculated by the Eq. (4.18) (Section 4.4.2)

$$\Omega_{mn} \approx \left[(1-\nu^2)\frac{k_m^4}{k_h^4} + \beta^2 k_h^4 R_o^4\right]^{\frac{1}{2}} (1+n^{-2})^{-\frac{1}{2}}, \qquad n > 0 \tag{5.14}$$

The axial web number km is dependent on the boundary condition and axial mode parameter. The boundary condition is taken Fixed-Fixed.

For the n=5 and m=1 mode, the axial (km) and helical web number (kh) are 1.686 and 7.4503. The approximate non-dimensional frequency parameter as per the Eq. (5.14) is 0.1184. The dialational plate velocity for the shell is 5.257×10^3 m/sec. The angular frequency for the mode shape is 903.398 radian/sec. Hence the natural frequency of the mode is 143 Hz.

For the n=5 and m=2 mode, the axial (k_m) and helical web number (k_h) are 2.811 and 7.7823. The approximate non-dimensional frequency parameter as per the Equation 5.14 is 0.1698. The dialational plate velocity for the shell does not change because it depends on the material property only. The angular frequency for the mode shape is 1296 radian/sec. Hence the natural frequency of the mode is 206 Hz.

The frequencies calculated analytically and with ANSYS are in close agreement. This validates the ANSYS results and process. This process is used for the outer shell for the parametric analysis.

5.7.2.4Natural frequencies of mode shapes for outer shell

The thickness of the outer shell is 3 mm hence the inner shell is modeled with surface modeling so that the thickness can be varied if the natural frequency of mode shape is below 100 Hz. Thickness is taken as a parametric parameter. The ends of the shell are fixed-fixed as per the actual condition.

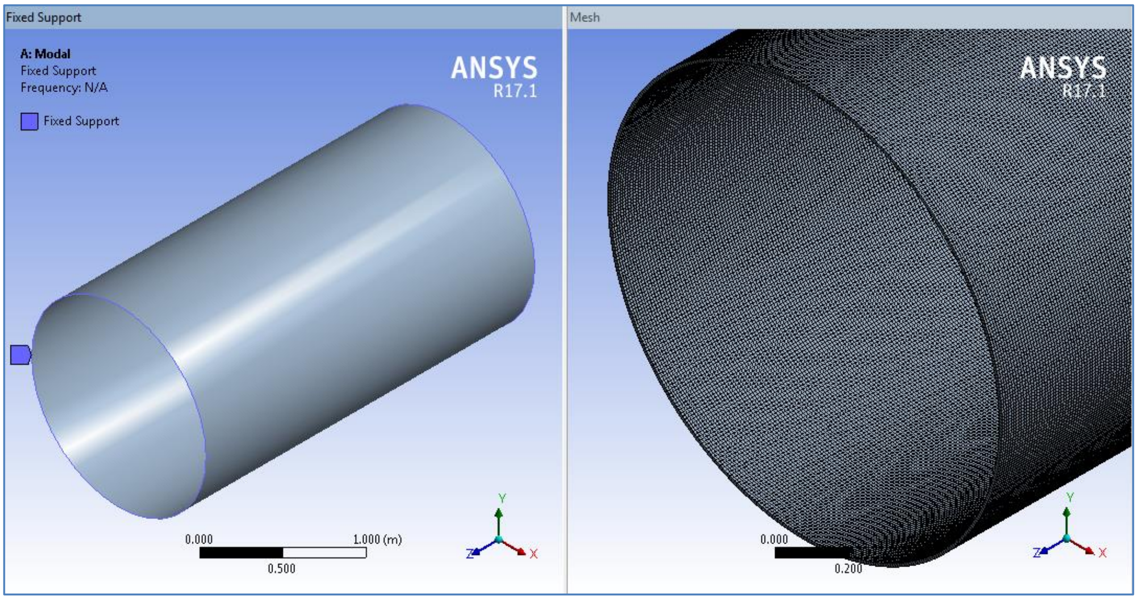

Figure 5.28 Outer shell with boundary condition and mesh

The outer shell (Fig. (5.28)) is meshed with an element size of 1×10^{-2} m to increase the accuracy level. The mesh has 130946 nodes and 130480 elements. The outer shell is analyzed for the different natural frequencies mode shapes for 3 mm thick. Twenty number of frequencies are extracted, which are given in the frequency chart (Fig. (5.29)).

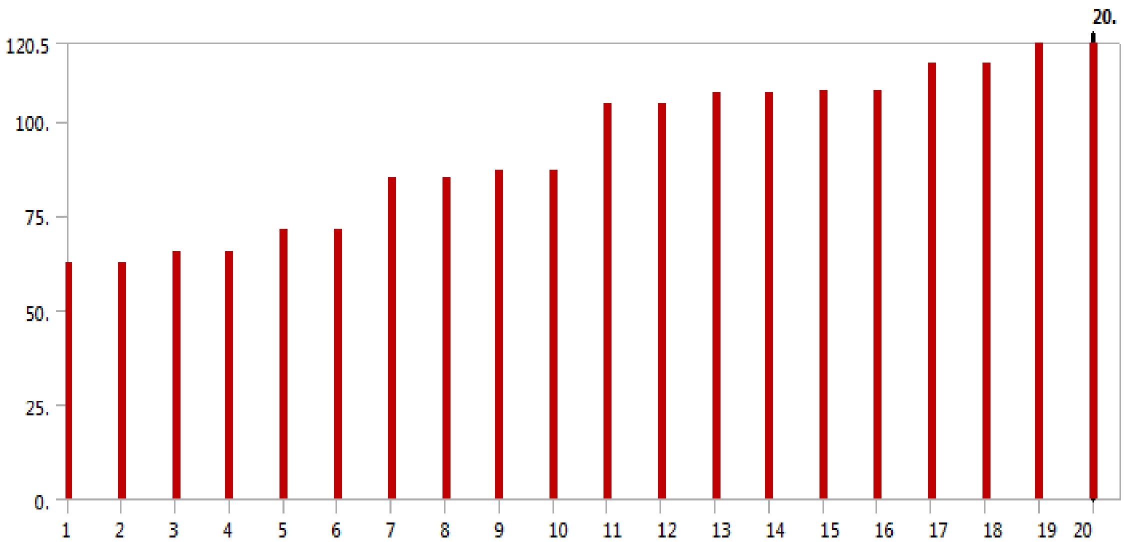

Figure 5.29 Natural frequency against the mode number for Outer Shell (Thk. = 3 mm)

The starting frequency is 61 Hz which is below 100 Hz (as required). Hence the thickness is changed from 3 mm to 11 mm. The twenty number of frequencies extracted for all the different thicknesses. The natural frequencies for 11 mm thick outer shell are shown in Fig. (5.30).

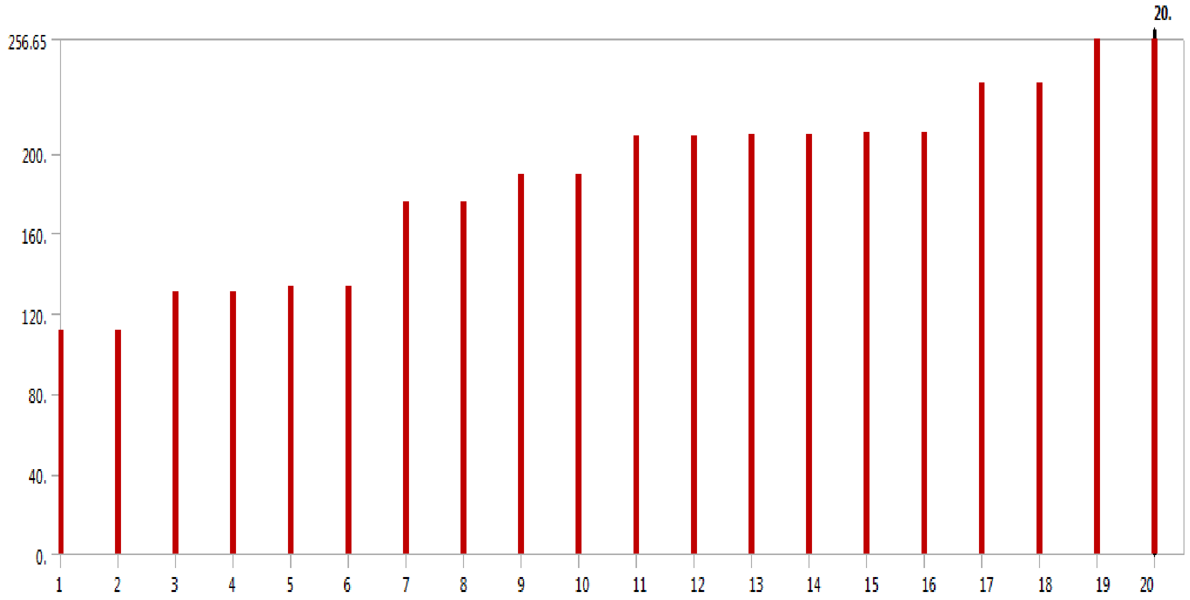

Figure 5.30 Natural frequency against the mode number for Outer Shell (Thk. = 11 mm)

The natural frequencies for all the mode shapes between 3 mm to 11 mm are tabulated in Table (5.8),

Table 5.8 Natural frequency with different thickness for Outer Shell

Frequency	Thickness of outer shell (mm)					
	3	5	7	9	10	11
f1	61	78	94	102	106	111
f2	64	88	95	111	121	130
f3	70	89	116	130	131	133
f4	83	110	129	145	160	175
f5	86	127	151	174	181	189
f6	103	132	155	181	194	208
f7	106	137	161	193	206	209
f8	107	141	174	203	208	210
f9	113	150	196	208	214	234
f10	120	157	198	215	235	256

The thickness of the outer cylinder is taken as 11 mm because it fulfills the criteria of frequency (111 Hz) more than the required frequency (>100 Hz). Another reason for selecting the 11 mm is that the 1st mode frequency of outer shell (111Hz) is matching with Inner shell 1st mode frequency (111 Hz). The mode shapes of outer shell at 111 Hz is same as inner shell as shown in Fig. (5.31).

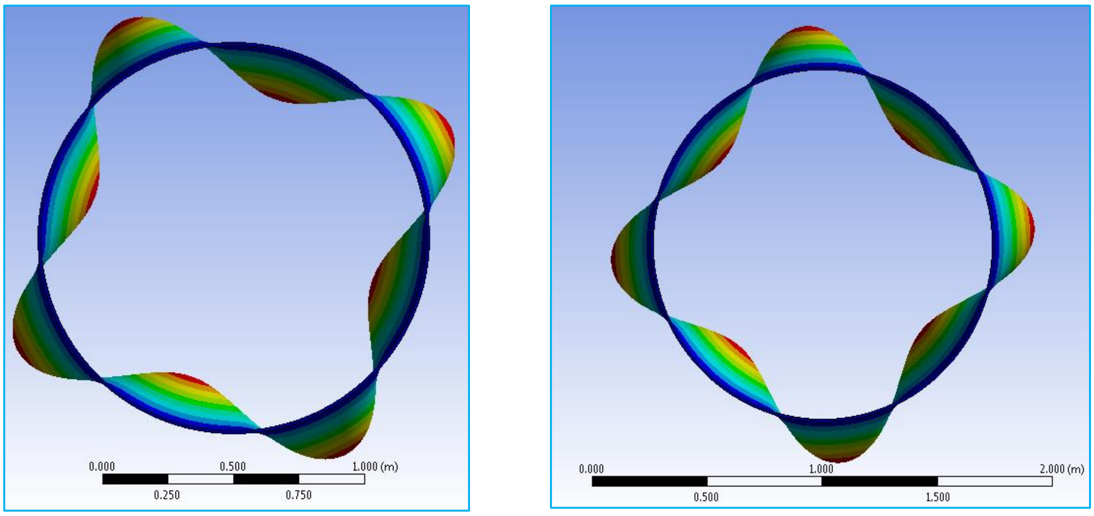

Figure 5.31 Outer shell mode shapes at 111 Hz frequency

The frequencies for both the inner shell and outer shell are shown in the Table (5.9).

Table 5.9 Natural frequency with different thickness for Outer Shell

Mode Number	1	2	3	4	5	6	7	8	9	10
Frequency(Hz) Inner Shell (Thk. -10 mm)	111	129	137	188	191	204	206	218	255	275
Frequency(Hz) Outer Shell (Thk. -11 mm)	111	130	133	175	189	208	209	210	234	256

The comparison of both the frequencies is shown in the Fig. (5.32).

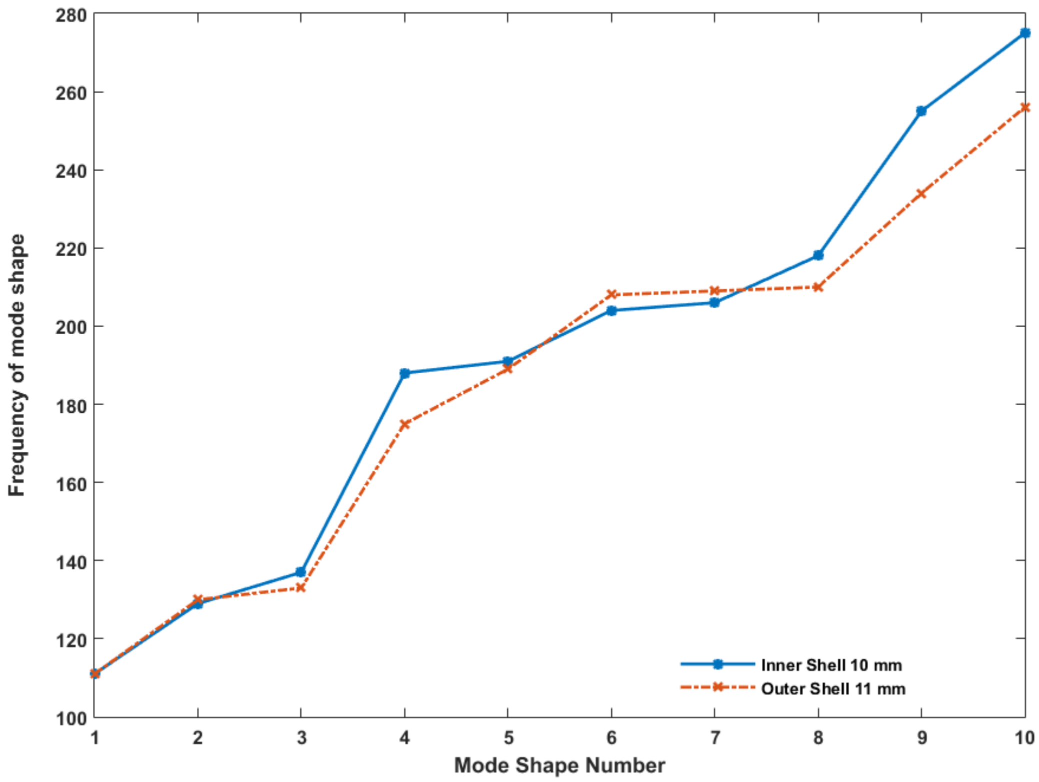

Figure 5.32 Natural frequency for Inner (10 mm thk.) and Outer shell (11 mm thk.)

The Fig. (5.32) shows that as the mode shape increases the diversion of the frequency increases.

As per the mode shapes and vibration criteria, the thickness of the inner shell is taken as 10 mm. The thickness of the outer shell is 3 mm as per the structural design point of view and 11 mm as per the vibration point of view. Hence noise level is checked for the range from 3 mm to 11 mm. If the frequency of vibration and mode shapes are same for both the shells then the fluid disturbance is minimum. The minimum fluid disturbance is the base for low noise.

5.7.3. Bubble-induced noise

The noise induced by impacting the surface is abbreviated as bubble-induced noise. The noise is calculated based on the flow chart as shown in Fig. (5.33)

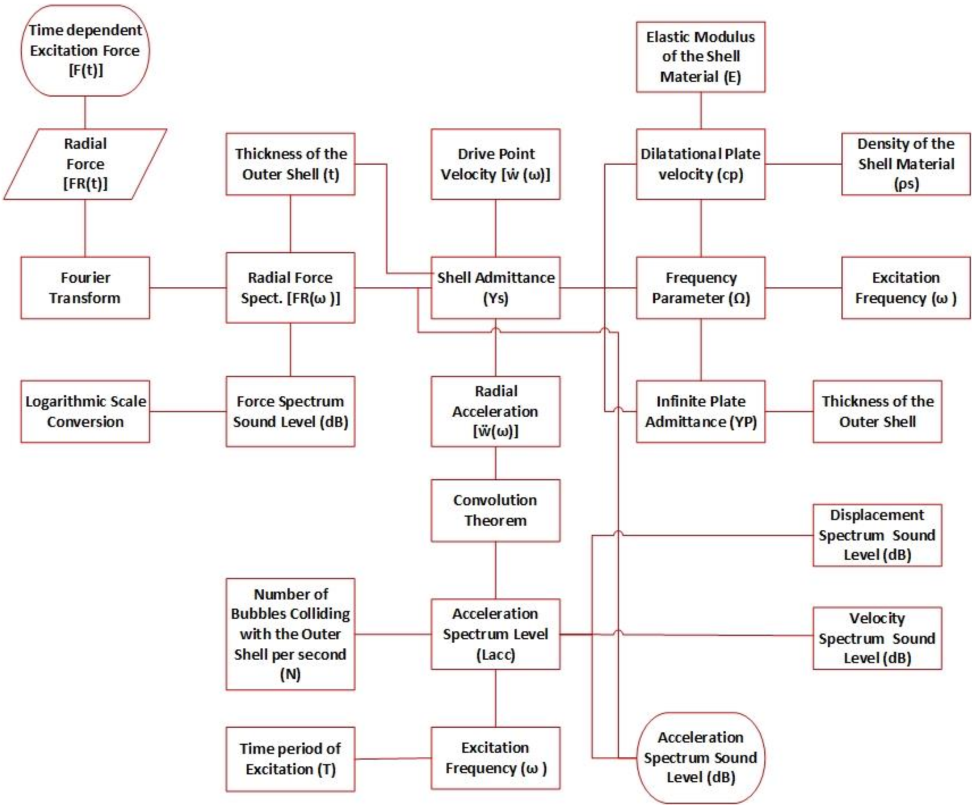

Figure 5.33 Flow chart for the bubble induced noise in terms of Force, Acceleration, Velocity and Displacement

5.7.3.1Plate admittance and shell admittance

The admittance is the function of the configuration and the material properties. The material properties for SS304L are mentioned in the Table (5.2). The dialational plate velocity is calculated as 5.257×10^3 m/sec, which is closely matching with the value of dialational plate velocity mentioned as 5.4×10^3 m/sec (Section 4.5.2). Plate admittance is the function of the shell thickness. The values of plate admittance for the inner shell (10 mm) and outer shell (11 mm) are 1.04×10^{-4} m/Ns and 8.56×10^{-5} m/Ns. The variation of plate admittance with the thickness is shown in Fig. (5.34).

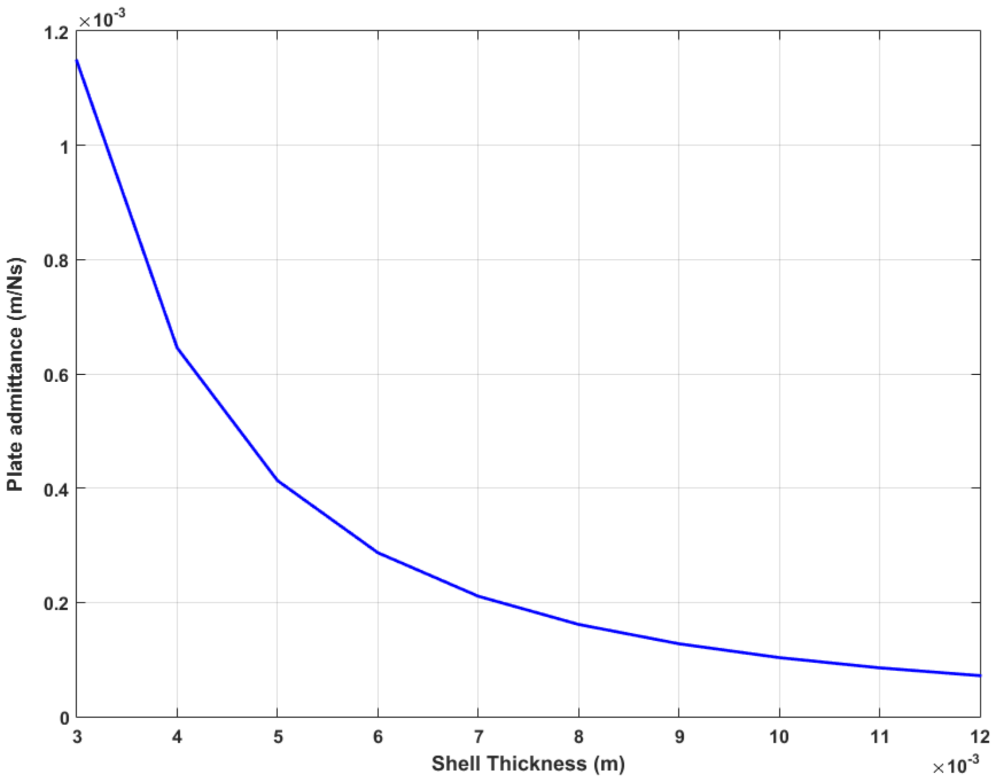

Figure 5.34 Plate admittance variation with the shell thickness

Fig. (5.34) shows that plate admittance decreases with the increase in the thickness. The shell admittance is related with the plate admittance. The relation for the shell admittance for the cylindrical configuration with respect to noise is used. The relation is,

$$20\,log\left|\frac{Y_s}{Y_p}\right| = 15\,dB + 20\log\Omega \tag{5.15}$$

The value of the non-dimensional parameter (Ω) is taken lowest for the mode number 3 as 0.049. This parameter is equivalent to the excitation frequency of 56 Hz for the outer shell and 60 Hz for the inner shell. The change in the frequency is due to the change in the value of diameter of the shell. The thickness of inner shell is fixed as 10 mm. Hence the shell admittance for the inner shell is 2.87×10^{-5} m/Ns. For the outer shell, the thickness is varied from 3 mm to 11 mm, hence entire range is calculated for the outer shell. The shell admittance variation as per the value of plate admittance for the outer shell is shown in the Fig. (5.35).

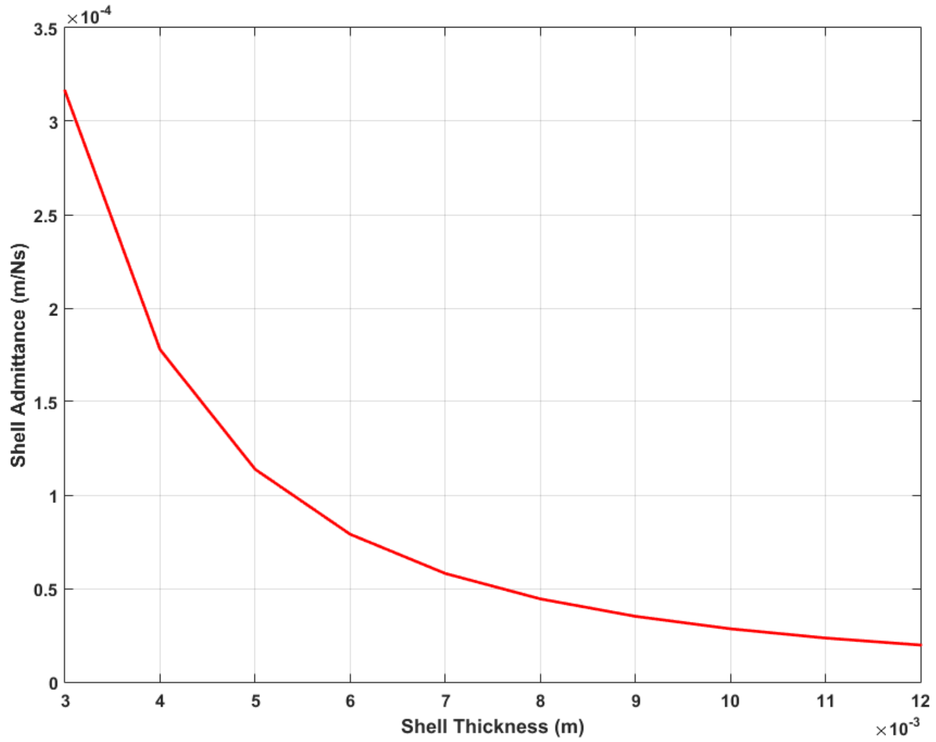

Figure 5.35 Shell admittance variation with the shell thickness

From the Fig. (5.35), the value of shell admittance for the inner shell (10 mm) thickness is the thickness of 3 mm and 11 mm are 3.16×10^{-4} m/Ns and 2.39×10^{-5} m/Ns. The value of shell admittance continuously decreases as per the increase in the thickness of shell.

5.7.3.2Radial impact force (Time domain)

The bubble strikes the inner shell and outer shell in the vertically upward direction, hence it produces the total impact force. This impact force is resolved in the normal and tangential direction of the shell surface. The force in the normal direction is called as a radial force. The radial force is the responsible force to produce the noise.

The radial force for the outer shell and inner shell is shown in Fig. (4.9) and Fig. (4.10) under Section 4.5.1.1 and Section 4.5.1.2 and is expressed as.

$$F_R = Fsin\emptyset_0 \tag{5.16}$$

The value of $sin\emptyset_0$ is dependent on the travel height of bubble. The equations for the inner and outer shell with respect to height are

$$sin\emptyset_0 = \frac{H_i}{R_i} \quad \text{and} \quad sin\emptyset_0 = \frac{H_o}{2R_0} \tag{5.17}$$

where Hi and Ho are the heights traveled by the bubble before striking to the inner and outer shell respectively. Ri and Ro are the radii of inner and outer shell respectively.

The height travelled by the bubble for the inner shell between $0 < R < R_i\ (0.689\ m)$ is calculated from

$$H_i = \sqrt{(R_o{}^2 - R^2)} - \sqrt{(R_i{}^2 - R^2)} \tag{5.18}$$

And the height traveled by the bubble for the outer shell between $R_i\ (0.689\ m) < R < R_o\ (0.743\ m)$ is calculated from

$$H_o = 2\sqrt{(R_o{}^2 - R^2)} \tag{5.19}$$

The cryopump is symmetric in nature about the center line, hence the analysis is carried out only on one side of the cryopump.

The radial impact force for the inner shell is shown in Fig. (5.36).

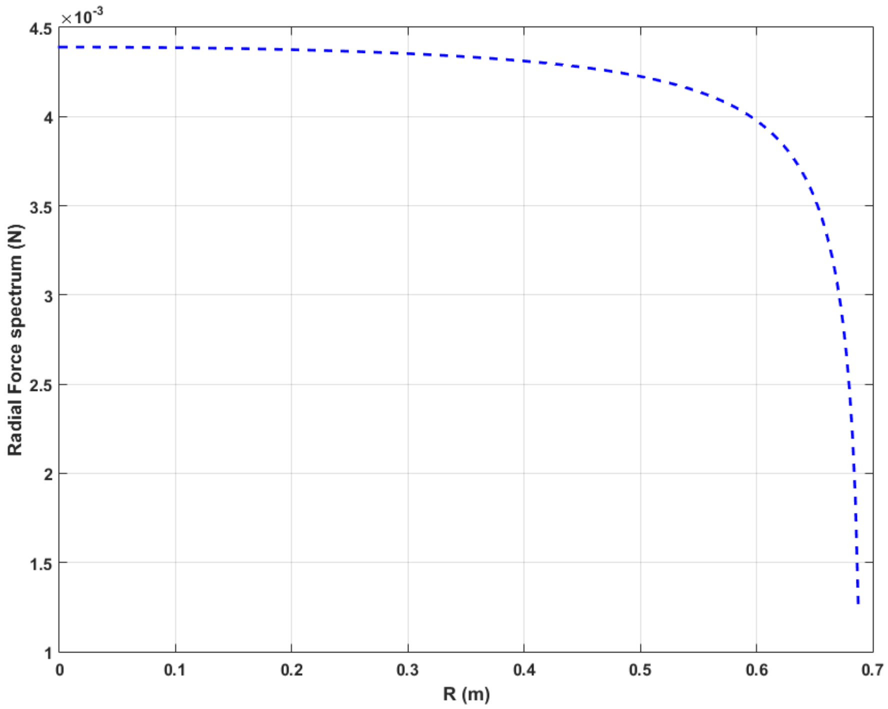

Figure 5.36 Radial impact force on one side of cryopump for inner shell (R=0 to R=Ri)

The radial force (0.0044 N) at R=0 is same as the total impact force (0.0044 N) at R=0 because the bubble at R=0 strikes normal to the surface. The radial force decreases as the radial distance increases and becomes negligible at R=Ri.

The radial impact force for the Outer shell is shown in Fig. (5.37).

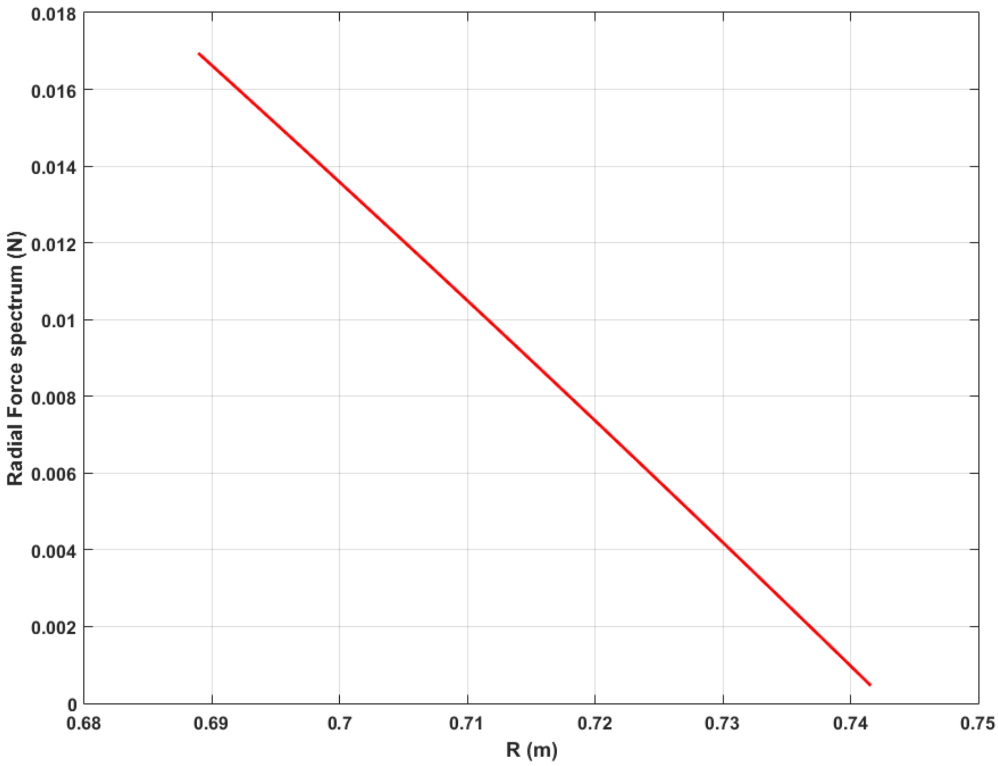

Figure 5.37 Radial impact force on one side of cryopump for outer shell (R=Ri to R=Ro)

The maximum radial impact force is 0.017 N (at R=Ri) on the outer shell. The bubble does not strike the outer shell normal to the surface at any point. Hence the impact force normal to surface decreases, which is responsible for the vibration.

5.7.3.3Radial impact force (Frequency domain)

The radial impact force is changed from the time domain to the frequency domain. This force is the base for the noise level. The radial impact force in the frequency domain for the inner shell is shown in Fig. (5.38).

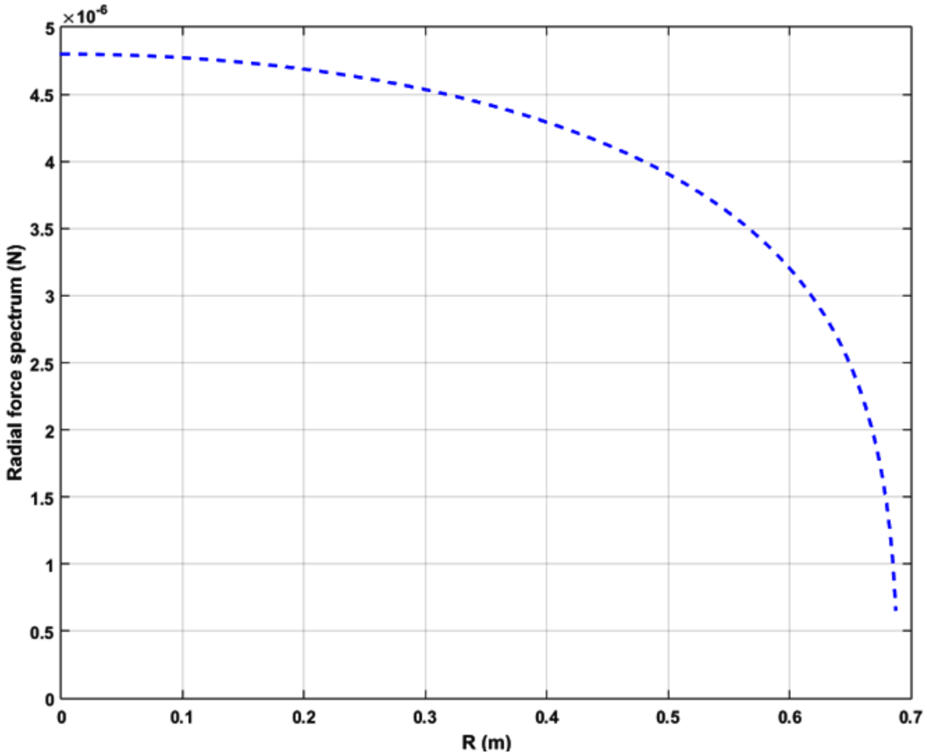

Figure 5.38 Radial impact force (frequency domain) on one side of cryopump for inner shell

Fig. (5.38) shows that radial impact force is 4.8×10^{-6} N at R=0, which is the maximum force and it decreases with radial distance.

The radial impact force in the frequency domain for the outer shell is shown in Fig. (5.39).

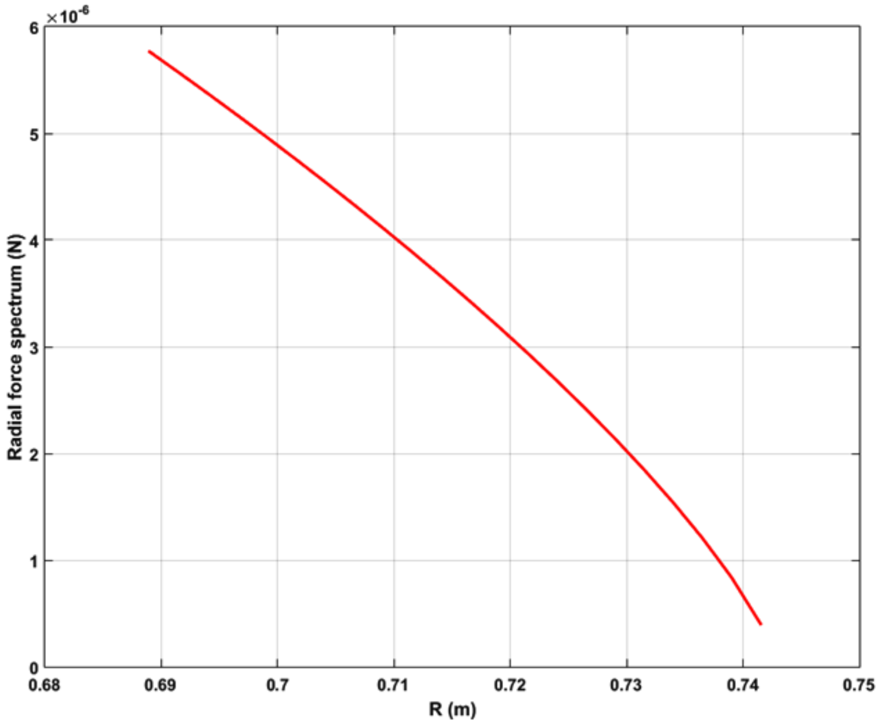

Figure 5.39 Radial impact force (Frequency domain) on one side of cryopump for outer shell

Fig. (5.39) shows the maximum radial impact force for the outer shell is 5.8×10^{-6} N. This force is quite close to the maximum radial impact force for the inner shell. It indicates that maximum noise produced by bubble on the inner shell will be almost closer to the maximum noise produce by bubble on the outer shell.

5.7.3.4Force sound level spectrum

The radial impact force is calculated in terms of sound level. The sound level is abbreviated as noise because it interferes with the actual data at low frequency. The force sound level spectrum for the inner shell is shown in Fig. (5.40).

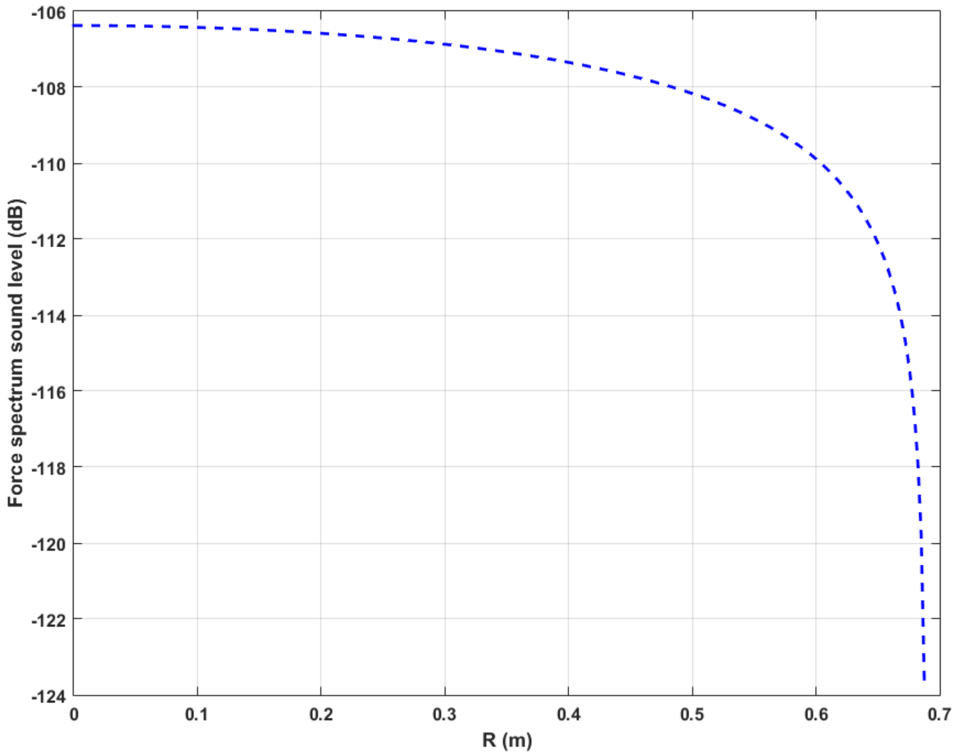

Figure 5.40 Force sound level spectrum for inner shell

Fig. (5.40) shows that the force sound level spectrum for inner shell varies from -106.4 dB (max.) to -123.6 dB (min.).

The force sound level spectrum for the outer shell is shown in Fig. (5.41).

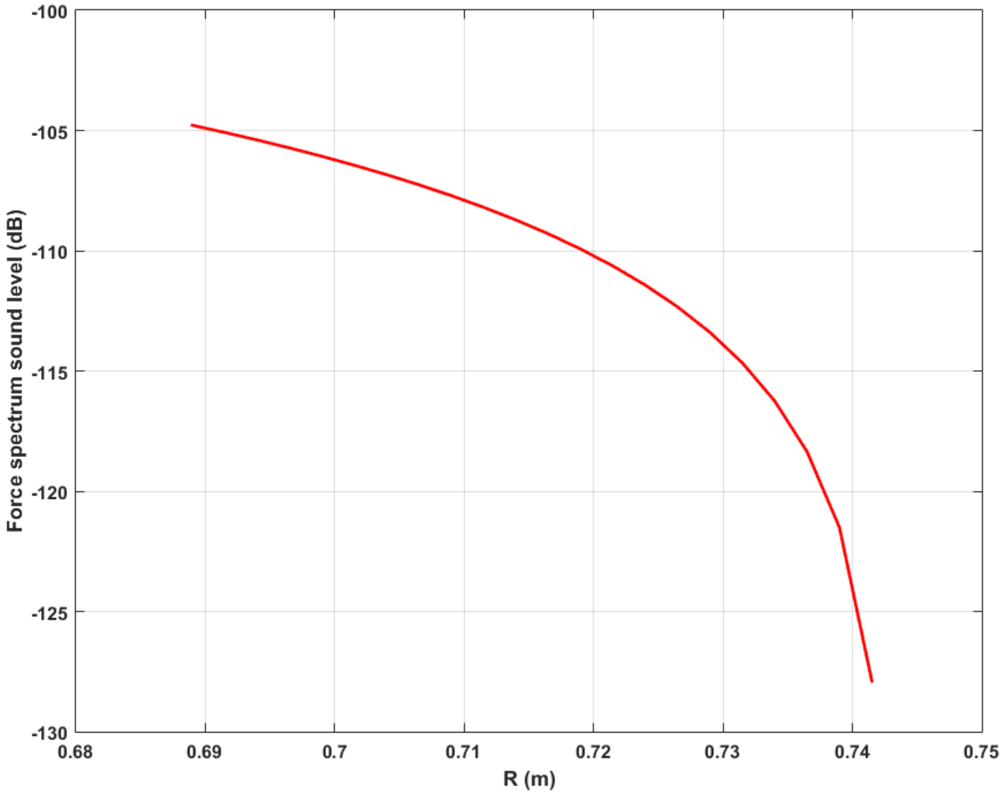

Figure 5.41 Force sound level spectrum for outer shell

Fig. (5.41) shows that the force sound level spectrum for outer shell varies from -104.8 dB (max.) to -127.9 dB (min.). This shows that the magnitude and direction of impact force are crucial parameters. The distance travelled by the bubble before impacting the outer shell is more than the distance travelled before impacting the inner shell. In the case of the inner shell, the maximum impact force was normal to the surface while for the outer shell, the maximum impact force was not normal to the surface. It confirms that the direction and magnitude are crucial to evaluate the noise spectrum. This force does not depend on the number of bubble striking or any other configuration of the material. It depends on the fluid and bubble diameter.

5.7.3.5Acceleration, velocity, and displacement sound level spectrum

The acceleration, velocity, and displacement sound level exist when any bubble strikes to the shell. This sound level spectrum depends on the material configuration, material property, admittances, force, excitation frequency, the number of striking bubbles etc.

The number of striking bubbles on outer and inner shell are different. The number of bubbles are calculated for the entire length of the circular shell. The number of striking bubbles from the single row of length is 1118. The frequency of the striking bubble depends upon the impact velocity. The impact velocity depends on the distance travelled. Hence the number of bubbles striking also changes as per the radial distance. The frequency of striking bubbles per second for inner shell is shown in Fig. (5.42)

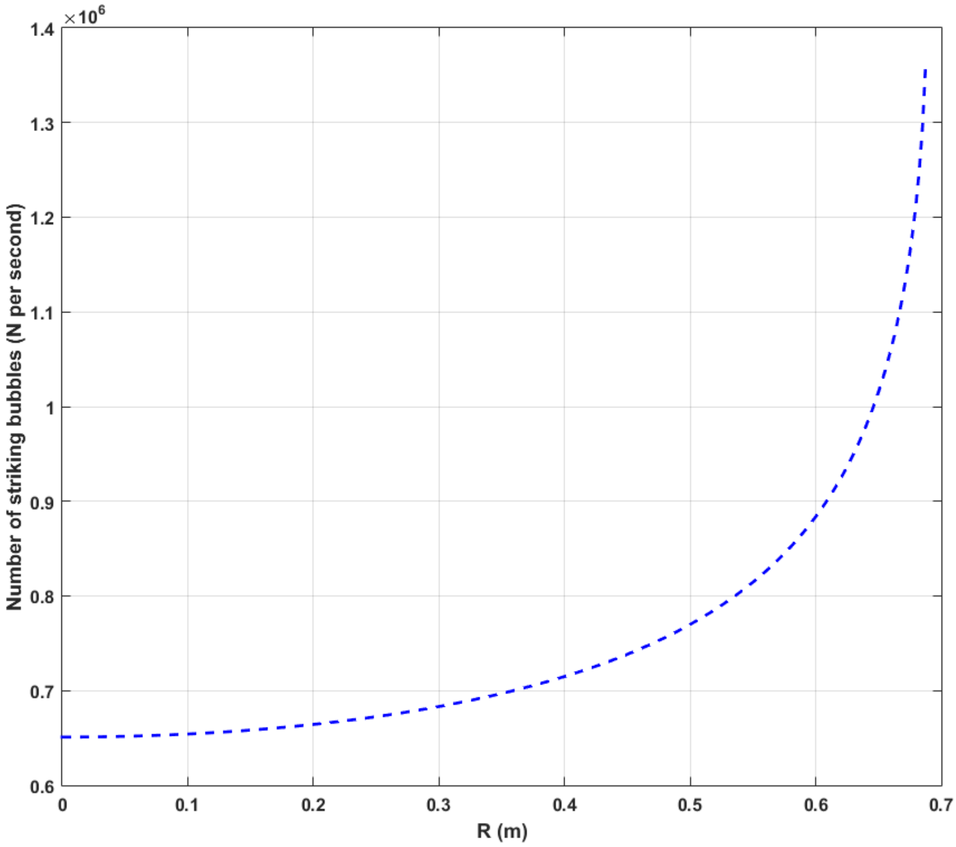

Figure 5.42 Frequency of striking bubbles on inner shell along radial direction

The total number of bubbles striking on inner shell are 2.06×10^{8} per second along the radial direction. The inner shell has a wide range for striking the bubbles i.e. along the diameter of the inner shell. The bubbles moving from the outer shell will strike the inner shell. Hence the total number is significant.

The frequency of striking bubbles per second for outer shell is shown in Fig. (5.43)

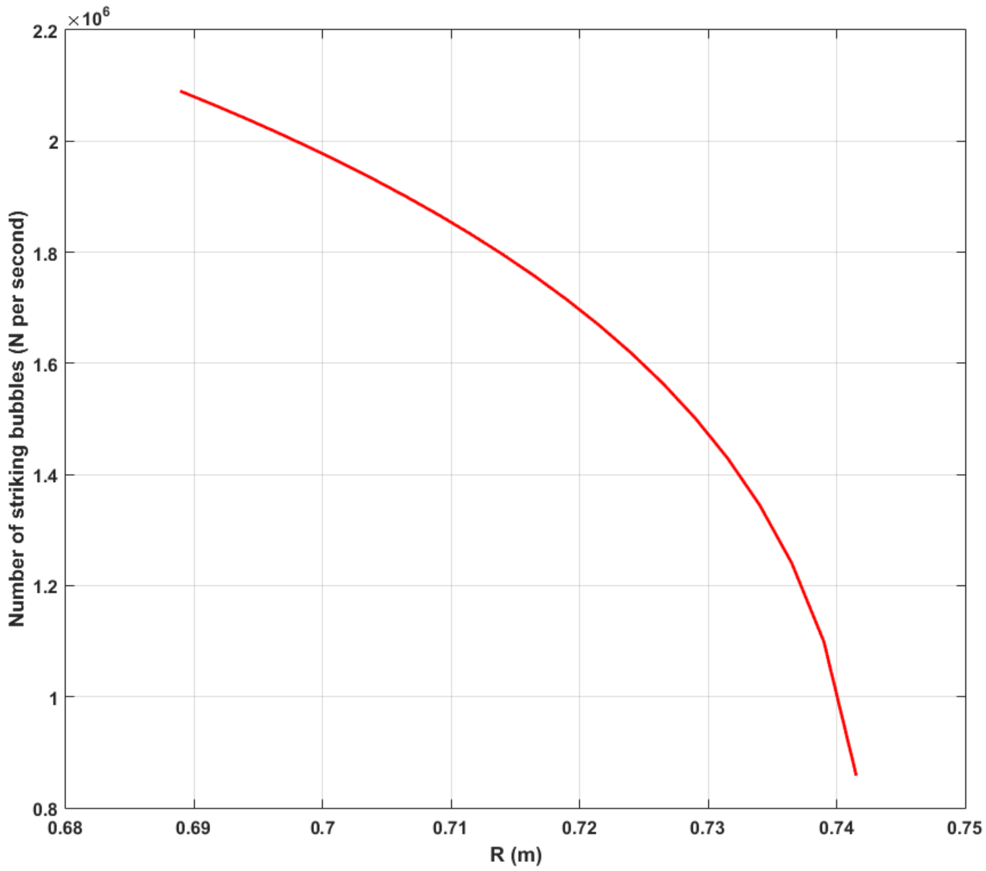

Figure 5.43 Frequency of striking bubbles on outer shell along radial direction

The total number of bubbles striking on inner shell are 3.72×10^7 per second along the radial direction. The outer shell has a very narrow annular gap. Only the bubbles coming out from the outer shell will strike to outer shell through the annular gap.

The excitation frequency for the inner shell is 60 Hz for the lowest non-dimensional frequency parameter at mode number 3. The sound level spectrum is shown in Fig. (5.44).

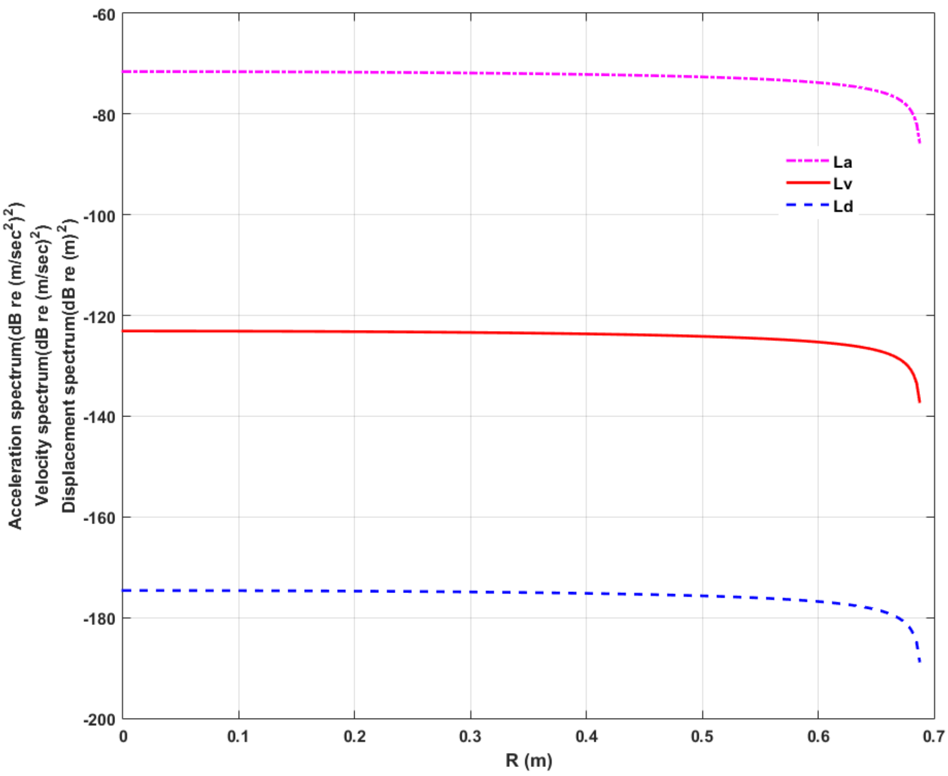

Figure 5.44 Acceleration, Velocity, and Displacement level spectrum for Inner shell

The sound level acceleration is produced by the force within the material, which in turn produces velocity and the displacement spectrum. The maximum and minimum values for sound level for the inner shell are shown in Table (5.10).

Table 5.10 Sound level spectrum for Inner Shell

Sound level spectrum (dB)	Acceleration	Velocity	Displacement
Maximum	-71.6	-123.1	-174.6
Minimum	-85.6	-137.1	-188.6

The excitation frequency for the outer shell is 55 Hz for the lowest non-dimensional frequency parameter at mode number 3. The thickness of the outer shell is taken as 11 mm (as per the vibration criteria). The sound level spectrum is shown in Fig. (5.45).

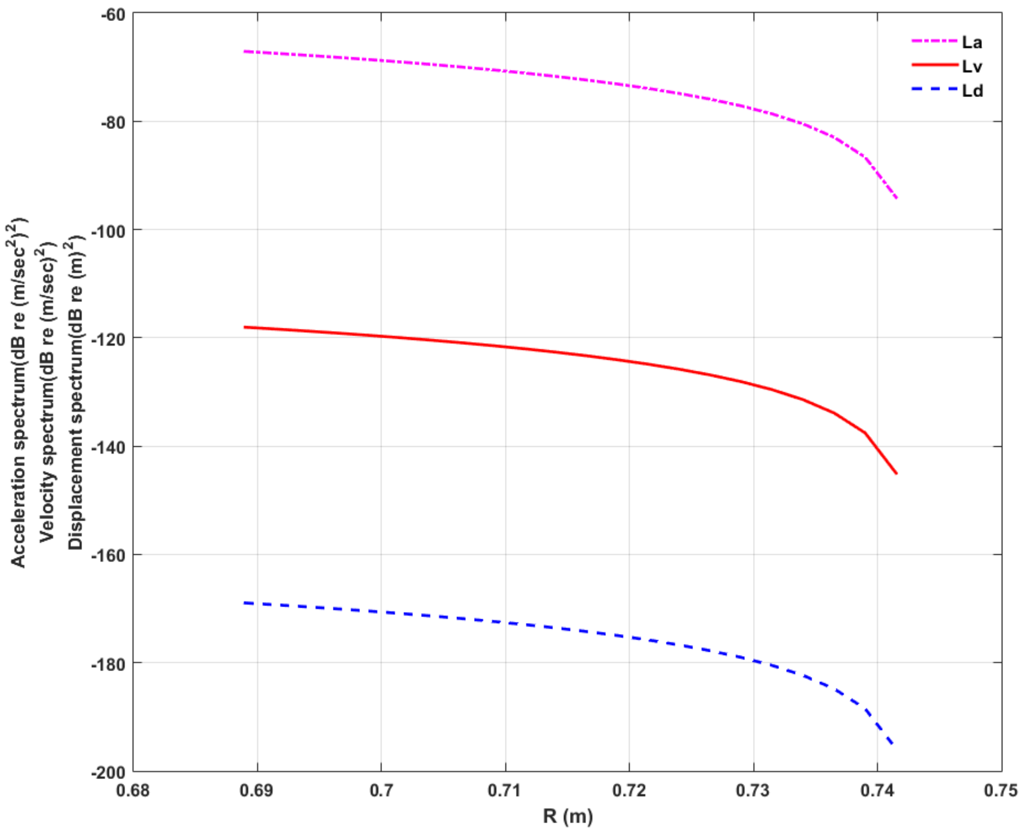

Figure 5.45 Acceleration, velocity, and displacement level spectrum for outer shell

Fig. (5.45) shows the same trend for the outer shell as given by the inner shell. The maximum and minimum values for sound level for outer shell are shown in Table (5.11).

Table 5.11 Sound level spectrum for Outer Shell

Sound level spectrum (dB)	Acceleration	Velocity	Displacement
Maximum	-67.1	-118.0	-168.9
Minimum	-94.1	-145.0	-195.9

The Table (5.10) and Table (5.11) indicates that the maximum magnitude of the sound level spectrum is same for both the shells either the thickness of both the shells are different. The thickness is also one of the key parameters for the sound to propagate within the shell. The effect of various parameters is checked on the sound level spectrums.

5.7.3.6Total bubble induced noise through LN2 cryopump

The bubble induced noise is calculated for the different travelling height of the bubble. The variation of sound spectrum level on the inner and outer shell is shown in Section 5.8.3.4 (Force) and Section 5.8.3.5 (Acceleration, Velocity, and Displacement). The variation is taken at one side of cryopump due to the symmetricity. The total noise is calculated by adding all the sound levels along the inner shell and outer shell.

The sound levels are based on a log scale, hence they can not be added directly. The addition of sound levels is dependent on the type of sources i.e. coherent or incoherent. For coherent sources, the sound levels are added as,

$$L_{Sum(c)} = 20log_{10}\left(10^{\left(L1/_{20}\right)} + 10^{\left(L2/_{20}\right)} +.\dots\dots..+10^{\left(Ln/_{20}\right)}\right) \tag{5.20}$$

where $L_{Sum(c)}$ is the total sound level from coherent sources and L1, L2, ……Ln are the individual coherent noise levels which have to be added. The Eq. (5.20) is written as

$$L_{Sum(c)} = 20log_{10}\left(\sum_{i=1}^{n} 10^{\left(Li/_{20}\right)}\right) \tag{5.21}$$

The incoherent sources are added as per the equation

$$L_{Sum(ic)} = 20log_{10}\left(\sum_{i=1}^{n} 10^{\left(Li/_{20}\right)}\right) \tag{5.22}$$

where $L_{Sum(ic)}$ is the total sound level from incoherent sources

The addition of n sound levels of equal amplitude (L) from the coherent and incoherent sources is

$$L_{Sum-n} = L + \Delta L \tag{5.23}$$

$$L_{Sum-n(c)} = L + 20log_{10}n \tag{5.24}$$

$$L_{Sum-n(ic)} = L + 10log_{10}n \tag{5.25}$$

where $L_{Sum-n(c)}$ and $L_{Sum-n(ic)}$ are the total noise from n sound coherent and incoherent sources and ΔL is the increase in the sound level with respect to L. ΔL is formulated up to 10 noise sources (Table (5.12)).

Table 5.12 Sound level increase in dB

Number of sources	1	2	3	4	5	6	7	8	9	10
$\Delta \boldsymbol{L}$ in dB (coherent)	0.0	3.0	4.8	6.0	7.0	7.8	8.5	9.0	9.5	10.0
$\Delta \boldsymbol{L}$ in dB (incoherent)	0.0	6.0	9.6	12.0	14.0	15.6	17.0	18.0	19.0	20.0

The sound level (dB) depends on the number of sound sources as shown in Fig. (5.46).

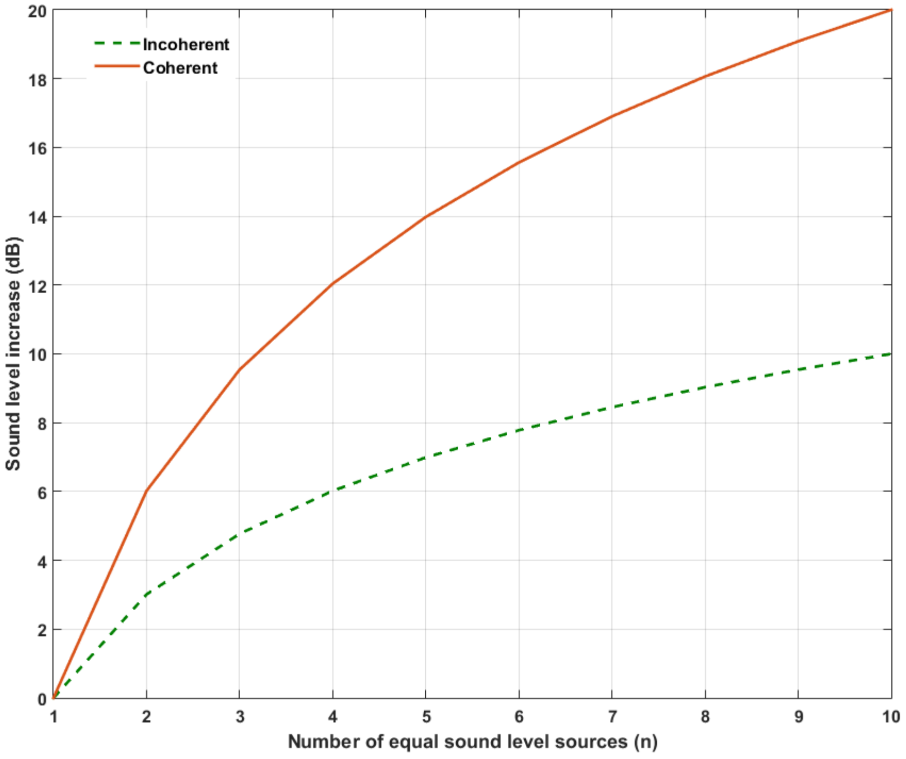

Figure 5.46 Sound level increase from equal sound level sources

The Fig. (5.46) shows that the sound level for the coherent sources increases twice than the incoherent sources. The sum of the sound levels spectrum for the cryopump on one side and both sides of the cryopump for Inner shell are given in Table (5.13) and Table (5.14) respectively.

Table 5.13 Sound level spectrum for inner shell (one side of cryopump)

Sound level spectrum	Acceleration	Velocity	Displacement	Force
Coherent (dB)	-23.6	-75.1	-126.7	-58.8
Incoherent (dB)	-47.9	-99.5	-150.9	-83.1

Table 5.14 Sound level spectrum for inner shell (both side of cryopump)

Sound level spectrum	Acceleration	Velocity	Displacement	Force
Coherent (dB)	-17.6	-69.1	-120.7	-52.8
Incoherent (dB)	-44.9	-96.5	-147.0	-80.1

The sum of the sound levels spectrum for the cryopump on one side and both sides of the cryopump for Outer shell are given in Table (5.15) and Table (5.16) respectively.

Table 5.15 Sound level spectrum for outer shell (one side of cryopump)

Sound level spectrum	Acceleration	Velocity	Displacement	Force
Coherent (dB)	-45.4	-96.3	-147.3	-82.5
Incoherent (dB)	-57.8	-108.7	-159.6	-95.1

Table 5.16 Sound level spectrum for outer shell (both side of cryopump)

Sound level spectrum	Acceleration	Velocity	Displacement	Force
Coherent (dB)	-39.4	-90.3	-141.3	-76.5
Incoherent (dB)	-54.8	-105.7	-156.6	-92.1

The total sound level spectrum from the LN2 cryopump is calculated by adding the sound level for inner shell and outer shell (Table (5.17)).

Table 5.17 Sound level spectrum for LN2 cryopump

Sound level spectrum	Acceleration	Velocity	Displacement	Force
Coherent (dB)	-16.9	-68.4	-119.9	-52.3
Incoherent (dB)	-44.5	-96.0	-146.5	-79.8

The total bubble induced noise band for the coherent and incoherent is shown in Fig. (5.47).

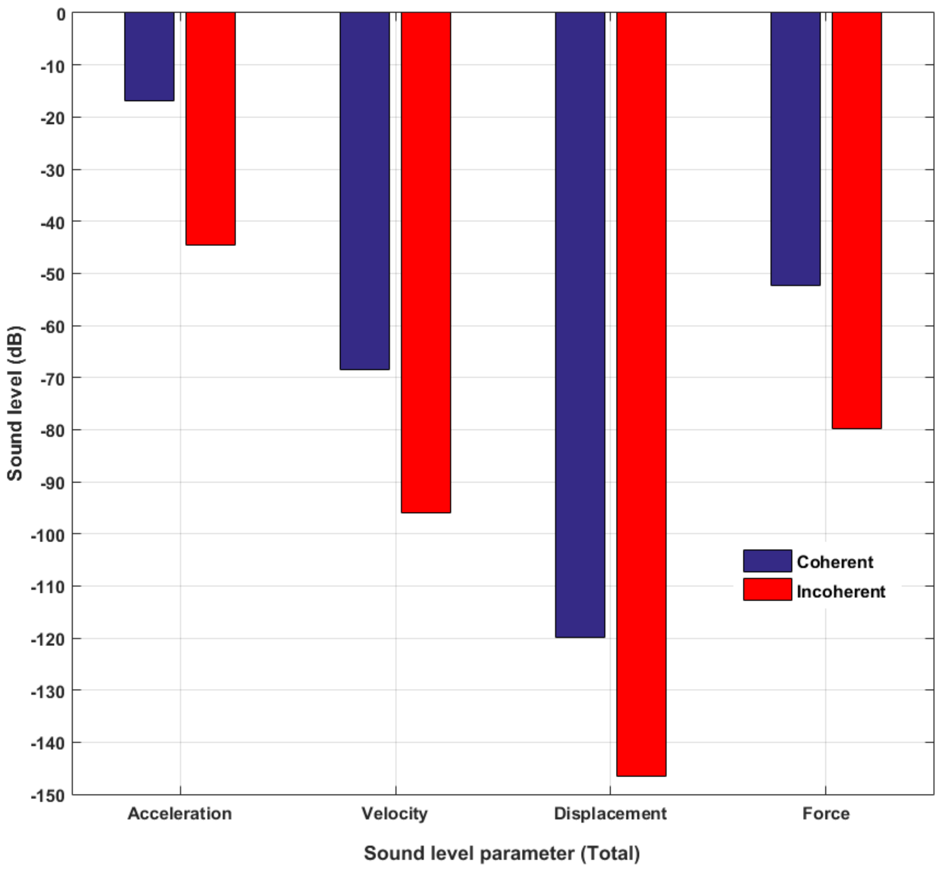

Figure 5.47 Total sound level for different sound level parameters

The Fig. (5.47) shows the variation in the sound level noise and it gives the maximum (coherent) and minimum (incoherent) value of noise for the LN2 cryopump. The bubble impacting may be coherent or incoherent in nature due to the different variable parameters. Hence the bubble induced noise will vary between the coherent and incoherent. The maximum noise of -16.9 dB is due to the acceleration.

5.7.4. Parametric study on bubble induced noise

The bubble induced noise is a function of various parameters like bubble diameter, the number of bubble striking, the thickness of shell etc. Few parameters are studied to check its effect on the bubble induced noise on the outer shell.

5.7.4.1Force noise Vs bubble diameter

Bubble diameter is the function of fluid properties. The fluid properties will change as per the different temperature and pressure conditions. At the atmospheric pressure, the fluid properties remain constant. In the case of liquid nitrogen, the temperature difference (ΔT) between the wall (Tw) and the saturation temperature (Tsat) can vary from 2-10 K for nucleate boiling [145], [146]. The boiling regime graphs indicate that after 10 K, the film boiling will start. ΔT = 5 K is the temperature, where the liquid nitrogen is purely in the nucleate boiling. After $\Delta T =$ 5 K, the film boiling phenomenon intitiates up to $\Delta T = 10$ K.

The temperature difference is responsible for the bubble departure diameter. The variation of bubble departure diameter is shown in Fig. (5.48).

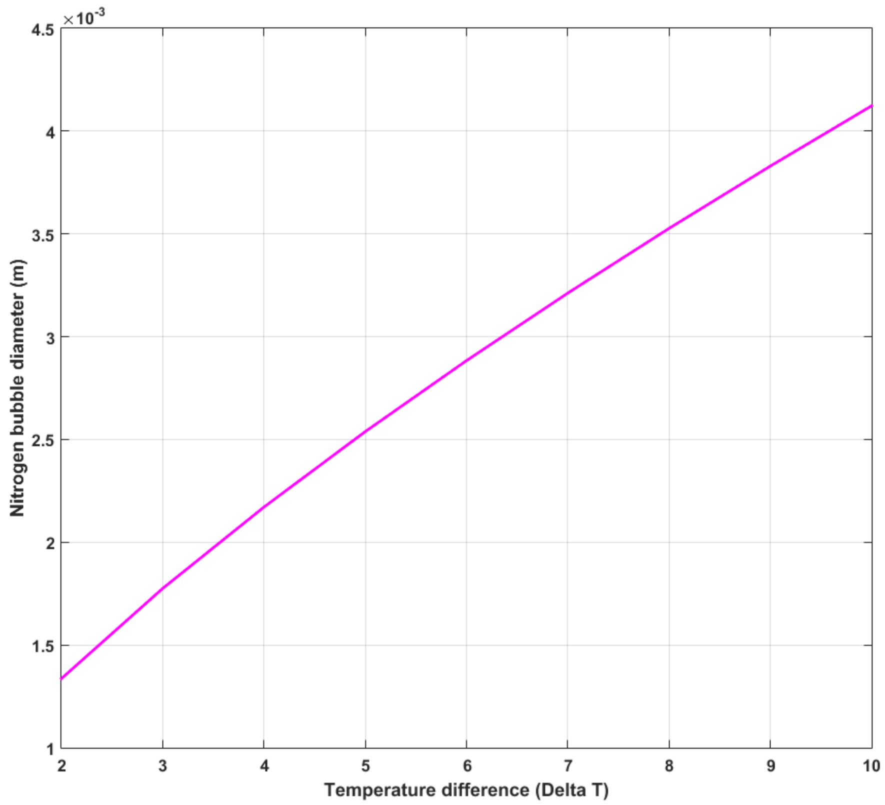

Figure 5.48 Total sound level for different sound level parameters

Fig. (5.48) shows that the bubble diameter is changed from 1.3 mm to 4.1 mm for the liquid nitrogen for nucleate boiling. The force spectrum (Fig. (5.49)) is analyzed according to the diameter of the bubble for the outer shell.

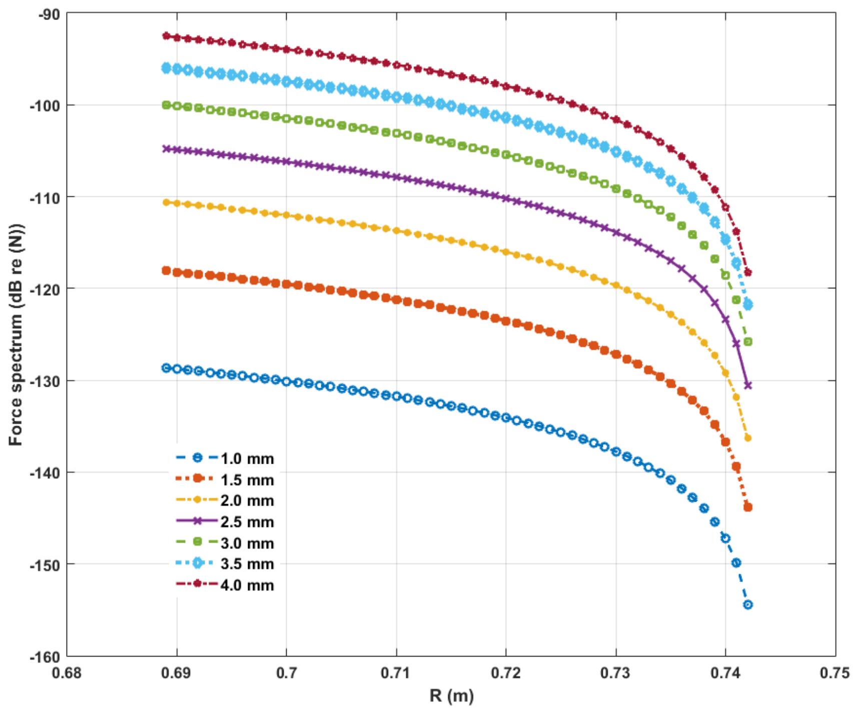

Figure 5.49 Force spectrum noise for different bubble diameter

Total force is the sum of all the individual forces, hence the bubble induced total force noise variation is calculated for the outer shell.

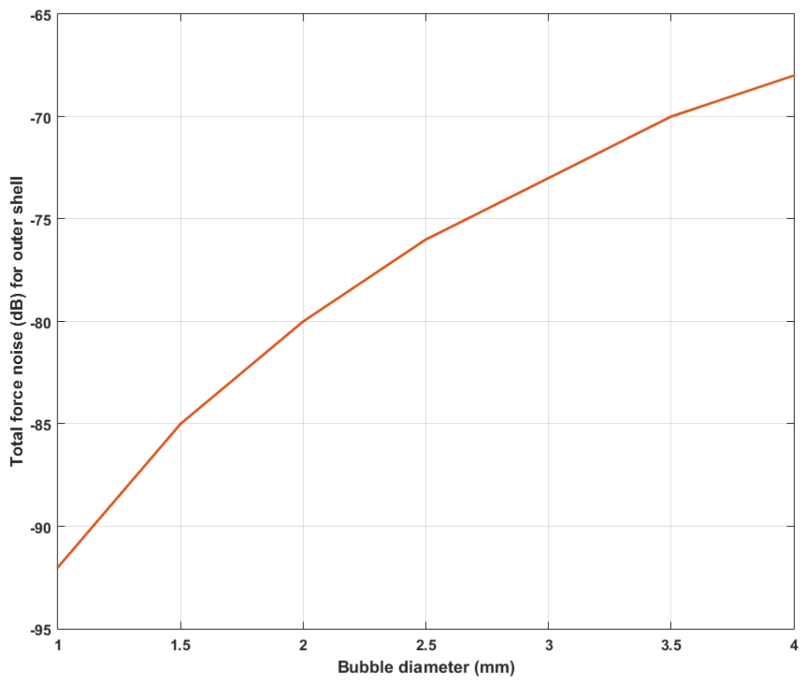

Figure 5.50 Total force noise with different bubble diameter for outer shell

Fig. (5.50) shows that the total noise increases as per the increase in the bubble diameter i.e. increase in the temperature difference.

5.7.4.2Acceleration, velocity and displacement spectrum Vs shell thickness

The acceleration, velocity, and displacement is a function of the thickness of the shell. The outer shell has 3 mm as per the mechanical design and 11 mm as per the vibration criteria. Hence the thickness is changed for outer shell from 3 mm to 11 mm. The changes in the spectrum are shown in the Fig. (5.51), Fig. (5.52) and Fig. (5.53).

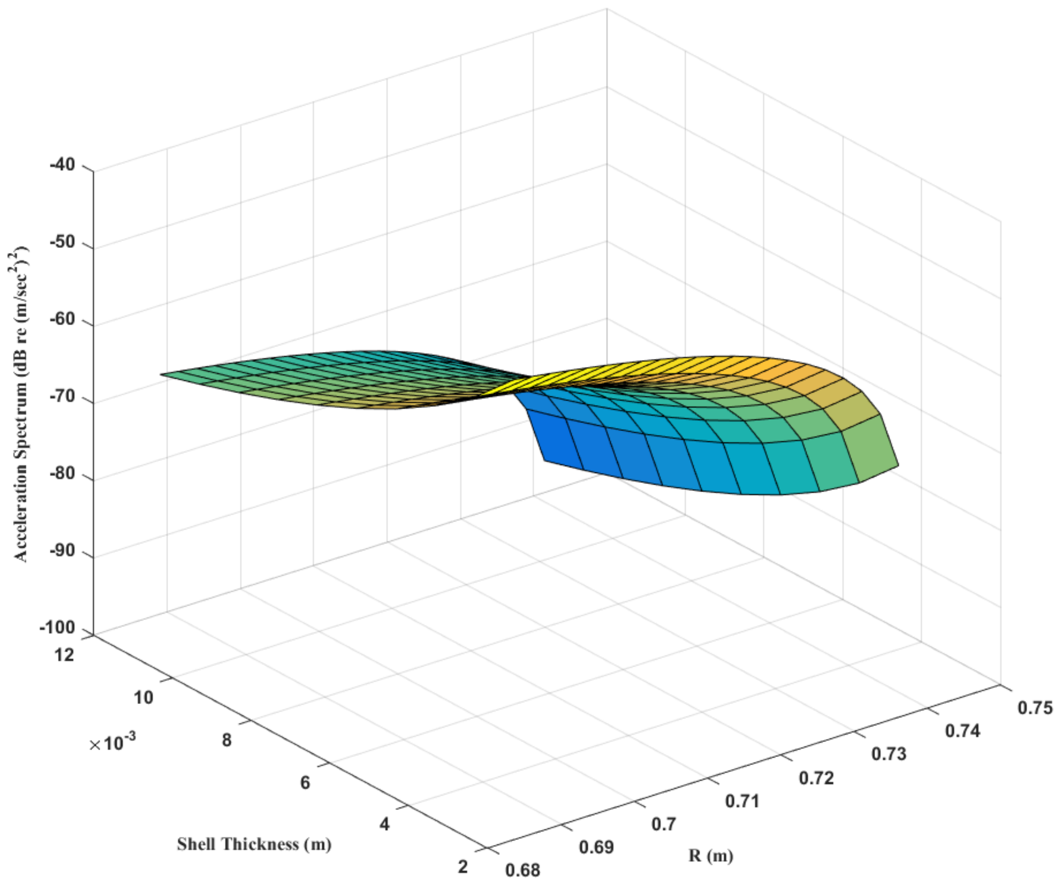

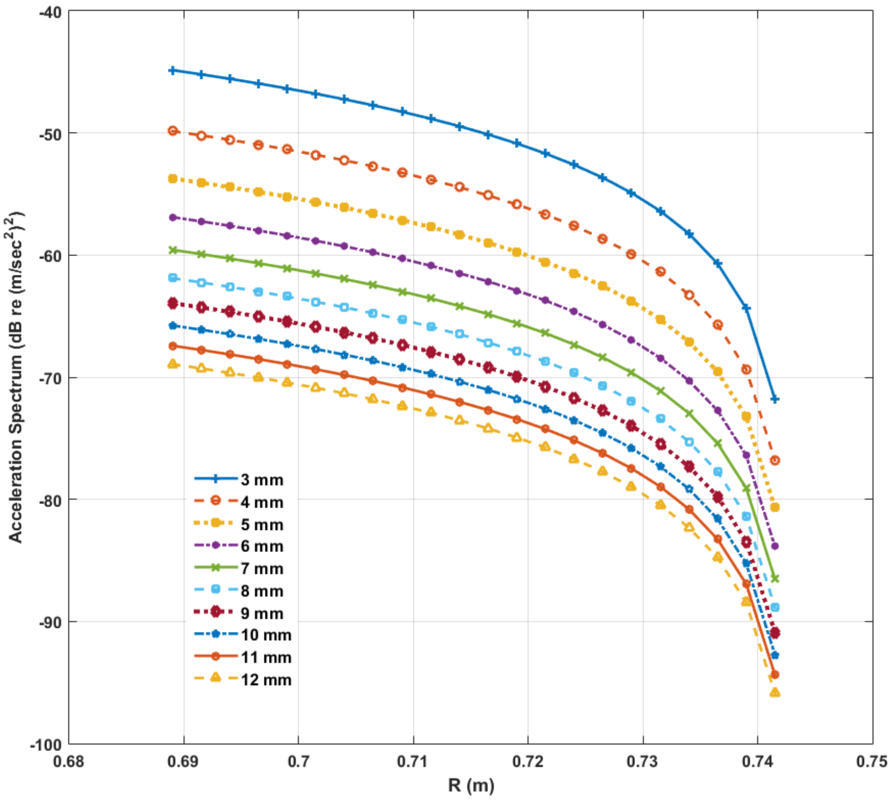

Figure 5.51 Acceleration noise spectrum with different shell thickness for outer shell

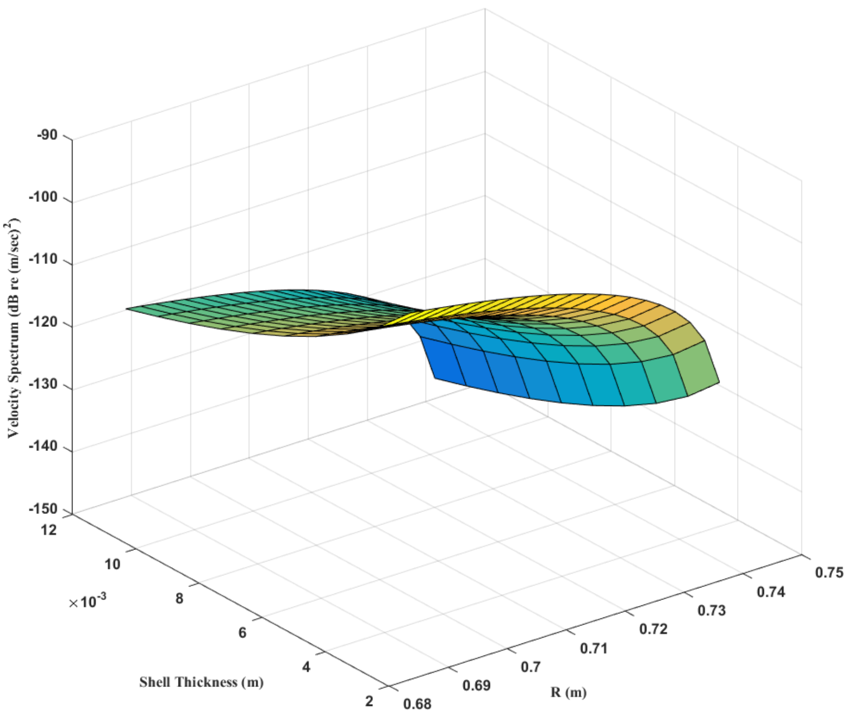

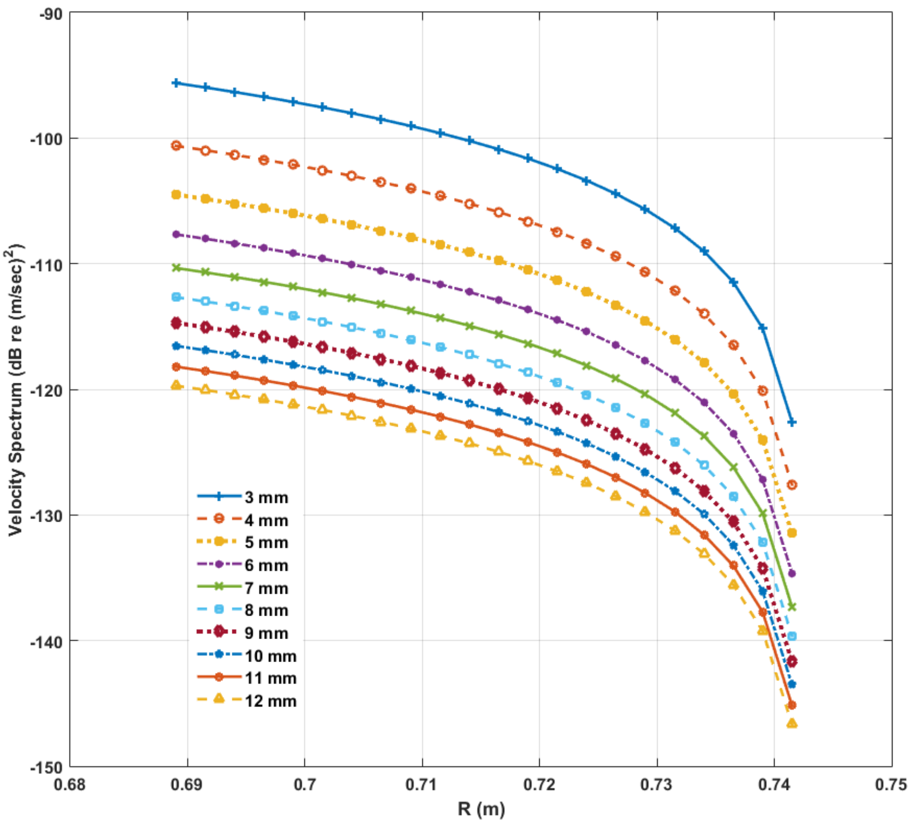

Figure 5.52 Velocity noise spectrum with different shell thickness for outer shell

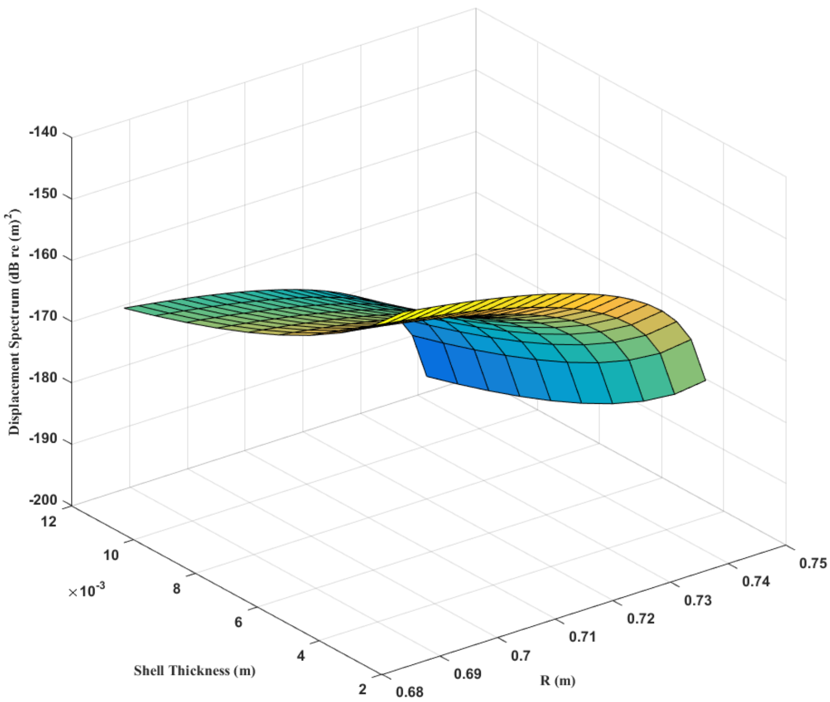

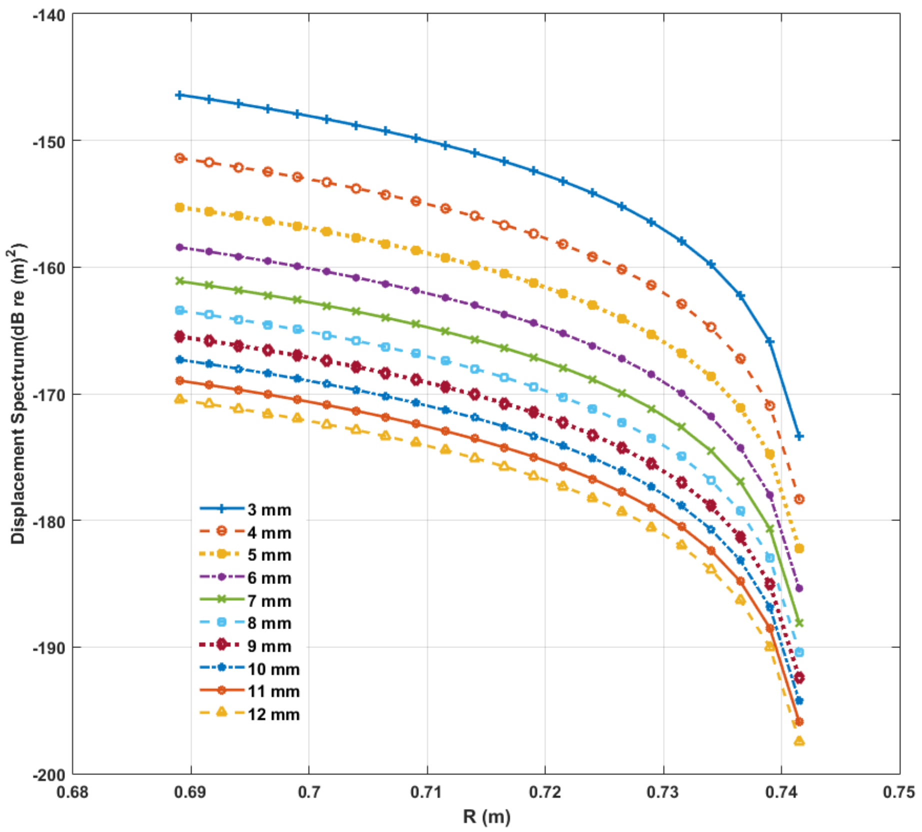

Figure 5.53 Displacement noise spectrum with different shell thickness for outer shell

The Fig. (5.51), Fig. (5.52) and Fig. (5.53) shows that the all the noises decrease with increase in the thickness of the shell. The decrement is shown in the Table (5.18).

Table 5.18 Sound level spectrum for LN2 cryopump

Noise Parameter	Thickness			
	3 mm		11 mm	
	Min. (dB)	Max. (dB)	Min. (dB)	Max. (dB)
Acceleration	-71	-44	-94	-67
Velocity	-122	-95	-145	-118
Displacement	-173	-146	-195	-168

From the Table (5.18), it is concluded that as the thickness of the shell increases, the noise reduces. The reduction in acceleration, velocity, and displacement are found as 17-20%, 12-13% and 10% in the displacement when thickness of shell changes from 3 mm to 11 mm.

5.7.4.3Noise level Vs number of bubbles striking the shell

The noise level is a function of the number of bubbles striking the shell. The outer shell is taken and the only single bubble is taken for a maximum height of 0.5561 m. If the number of striking bubbles increases on the same point then the noise level is plotted in Fig. (5.54).

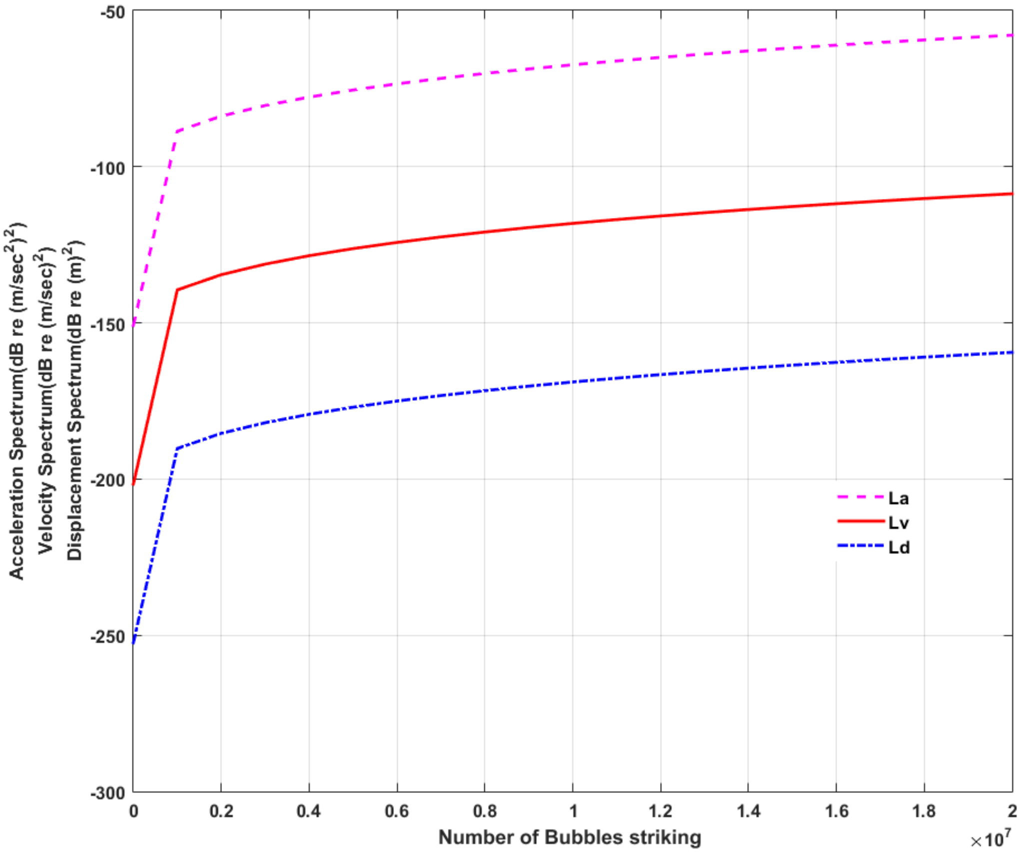

Figure 5.54 Noise spectrum with number of bubble striking for outer shell

Fig. (5.54) shows that as the number of striking bubbles increases the noise level also increases. The number of striking bubbles at a time for inner shell and outer shell are 308568 and 24596. Hence, the noise for the inner shell is more than the outer shell due to the more number of bubbles striking the inner shell.

5.8. Closing remarks

In this Chapter, the bubble dynamics for the bubble departure and motion are discussed. The motion with respect to the early and late time zone is analyzed for the liquid nitrogen bubble. The thickness required for the bubble induced noise is calculated according to the mechanical design, buckling criteria and vibration point of view. Different mode shapes are illustrated with the circumferential and axial mode numbers. The bubble induced noise spectrum for force, acceleration, velocity, and displacement are analyzed. The parametric study is given to check the effect of different parameters on the bubble-induced noise.

Chapter 6

Conclusions and Summary

LIGO is very sensitive towards the noise generated by any source. Liquid nitrogen cryopump is one of the noise source but it is one of the key component for LIGO. The noise generated by the cryopump is due to the bubble-structure interaction. This noise can distort the gravitational wave signal. Hence the noise generated by the cryopump is the main focus for investigation.

The problem is the amalgamation of three important domains as cryogenics, bubble dynamics, and noise associated with vibration. The noise and vibration produced inside the cryopump is due to the nucleate boiling of liquid nitrogen. Through the literature survey, it is known that these areas are not explored much for the sensitive applications like LIGO.

Bubble dynamics is used to analyze the noise and vibration. A generalized solution for the bubble dynamics is derived for a single liquid nitrogen bubble. The bubble displacement, velocity, and acceleration are derived for the early time zone and late time zone. The time to reach the terminal velocity by the bubble is also calculated. The bubble dynamics is applied to find out the impact force on the liquid nitrogen cryopump.

The radial impact force is responsible for the non-planer vibration. Hence the non-planer vibration for the circular shell has been investigated. The solution obtained is general for different sizes of circular shells with the different boundary conditions. The non-dimensional frequency parameter is drawn for all the circumferential modes of circular shell. The lowest frequency mode is achieved for the circumferential mode which corresponds to the radial impact force.

The thickness of the circular shells is calculated with the help of ASME code Section VIII division 1 for the external pressure vessel and internal pressure vessel sections. The external pressure vessel is checked for the buckling failure criteria. The thickness is verified for the low-frequency vibrational modes. The optimum thickness is obtained which satisfy the mechanical and vibrational criteria of the cryopump.

The analytical model for the bubble induced noise is developed, this model is generalized in nature for the circular shells. The different parameters responsible for the sound level spectrum are considered. Mechanical mobility of circular shell is taken into consideration with the help of shell admittance and plate admittance. The bubble induced noise for the force, acceleration, velocity and the displacement is analyzed.

The configuration of the liquid nitrogen cryopump is quite different than the other geometries as simple circular, rectangular etc. The configuration is concentric shells and the fluid is filled in the annular gap. The fluid present in the annular region makes the analysis difficult because the height traveled by bubble varies continuously. The bubble striking the inner shell and outer shell has different force on the shells. The impact force is also not normal to the surface and varies with respect to striking point. This provides the different spectrum for the bubble induced noise for the force, acceleration, velocity, and displacement.

The effect of bubble diameters due to the different temperature difference in the case of nucleate boiling, shell thickness and the number of bubbles striking the surface has been studied.

6.1. Conclusions

An analytical solution for the bubble induced noise is proposed which can be either used to study the circular shell or any other geometry. The bubble dynamics is dependent on the fluid properties according to different types of fluid. Hence the generalized solution is derived for any type of fluid. The concluding points are presented below.

1. The bubble diameter is dependent on the fluid properties, the temperature difference (ΔT) between the wall (or surface) and the saturation temperature of the fluid. Fluid properties depend on the operating pressure and temperature of the fluid. For a particular type of fluid, the bubble diameter increases as the temperature difference (ΔT) increases.

2. The net bubble departure force is in the order of 10^{-5} N in the case of nucleate boiling. Nucleate boiling considers only the vertical upward force. The main departure force is the buoyancy force, other forces do not affect too much.

3. The initial acceleration and entrained mass are found to be ~ 2g and half of the mass displaced by the bubble during the motion.

4. The bubble dynamics is dependent on the bubble diameter, migration time and the traveling time. If the traveling time is less than the migration time then the bubble is moving in early time zone otherwise in late time zone. Bubble motion parameters (acceleration, velocity, and displacement) changes according to the early time and late time zone. In early time zone, the bubble does not attain terminal velocity.

5. The impact force changes as per the distance travelled and impact velocity at the instant of striking the surface. The radial impact force is more important than the total impact force because the radial force is responsible for the vibration in the circular shell.

6. The natural frequencies corresponding to different mode shapes is are dependent on the boundary conditions, shape and size of the shell, length, and thickness of the shell. The combination of circumferential and axial mode number changes the natural frequency and the mode shapes.

7. The criteria for adopting the thickness of the outer and inner shell is based on the cut-off frequency (> 100 Hz) as well as mechanical stress.

8. The bubble induced noise provides the sound level spectrum for the different parameters. The induced noise is dependent on the bubble diameter, shell

thickness, the number of bubble striking, type of fluid, material properties, and configuration etc.

The methodology presented here is for a liquid nitrogen spherical bubble striking for the circular shell made up of isotropic and homogeneous material.

6.2. Contribution of the present work

The present work was initiated with the objectives of developing a generalized analytical formulation to study the bubble induced noise in the liquid nitrogen cryopump. The low-frequency noise is avoided during the operation of the cryopump which provides difficult data analysis in the detection of gravity waves. The set objectives are fulfilled effectively and following are the major contribution in the field of gravity wave detection.

1. A generalized solution to study the effect of bubble diameter on the bubble dynamics for any type of fluid is derived. The formulation can be used for any fluid with any bubble diameter.

2. The generalized analytical solution can be employed to analyze the bubble induced noise for circular shell made up of any material, having any boundary condition, for any noise parameter.

3. The nucleate boiling as a part of Sub-cooled Boiling Induced Vibration (SBIV) is analyzed in terms of vibration and noise.

6.3. Limitations

1. The present formulation is for the bubble induced noise in case of nucleate boiling only and can not be applied for the film boiling.
2. The solution is valid for quasi-static fluid condition only.
3. The solution is valid for isotropic and homogeneous material of the shell.

6.4. Future scope

- The present method can be verified experimentally for liquid nitrogen with different pressure fluids present in the annular gap.

- Heat transfer criteria can be considered for the bubble growth during the motion.
- The bubble induced vibration in the fluid flow condition can be extended further for different flow rates.

Publications

Journal Papers :

1. **Gupta M. K.,** Sharma D. S., and Lakhera V. J., "Vapor Bubble Formation, Forces, and Induced Vibration: A Review," Appl. Mech. Rev., vol. 68, no. 3, p. 30801-12, 2016. (ASME, Impact Factor – 7.912)
2. **Gupta M. K.,** Sharma D. S., and Lakhera V. J., "Bubble-induced noise and vibration in cylindrical shell filled with liquid nitrogen", The Journal of Mechanical Engineering Science, DOI: 10.1177/0954406217692842, (SAGE, Impact Factor – 0.730)
3. **Gupta M. K.,** Sharma D. S., and Lakhera V. J., "Detachment forces on Spherical bubble during formation" Materials Today: Proceedings (In Print) (Elsevier)
4. **Gupta M. K.,** Sharma D. S., and Lakhera V. J., "Material Selection Criteria for Vacuum and Cryogenic Applications" Materials Today: Proceedings, (Accepted) (Elsevier)
5. **Gupta M. K.,** Sharma D. S., and Lakhera V. J., " Bubble Dynamics in 80K LN2 Cryopump" (To be communicated)

Conference Papers :

6. **Gupta M. K.,** Sharma D. S., and Lakhera V. J., "Bubble Departure Force in 80k LN2 Cryopump", Conference Proceedings, National Conference on Design, Analysis, and Optimization in Mechanical Engineering (DAOME-2016), ISBN: 978-93-5258-81-2, p119-123, 18-19 March 2016. (In Proceeding)

References

[1] B. P. Abbott, M. K. Gupta, and E. Al., "Observation of Gravitational Waves from a Binary Black Hole Merger," *Phys. Rev. Lett.*, vol. 116, no. 6, p. 61102, 2016.

[2] J. K. Blackburn, "The Laser Interferometer Gravitational-Wave Observatory (LIGO) Project," *Math. Subj. Classification, Banach Cent. Publ.*, vol. 41, no. 617, pp. 95–135, 1991.

[3] J. F. J. Van den Brand, "Cryogenic vacuum links to isolate interferometer arms for Advanced Virgo (Nikhef Project Plan: Cryolinks)," National Institute for Subatomic Physics, The Netherlands, June 18, pp. 1-55, 2010.

[4] E. A. Hemmingsen, "Cavitation in gas−supersaturated solutions," *J. Appl. Phys.*, vol. 46, no. 1, p. 213, 1975.

[5] W. Gerth and E. Hemmingsen, "Gas supersaturation thresholds for spontaneous cavitation in water with gas equilibration pressures up to 570 atm," *Zeitschrift Naturforsch. Tl. A*, vol. 31, pp. 1711–1716, 1976.

[6] E. A. Hemmingsen, "Spontanous formation of bubbles in gas-supersaturated water," *Nature*, vol. 267, no. 1972, pp. 141–142, 1977.

[7] E. A. Hemmingsen, "Effects of Surfactants and Electrolytes on the Nucleation of Bubbles in Gas-Supersaturated Solutions," *Zeitschrift fur Naturforsch. - Sect. A J. Phys. Sci.*, vol. 33, no. 2, pp. 164–171, 1978.

[8] Cole R., *Boiling Nucleation*, vol. 10, no. 1. 1974.

[9] M. Blander, "Bubble Nucleation In Liquids," *Adv. Colloid Interface Sci.*, vol. 10, p. 1, 1979.

[10] R. E. Smallman and R. J. BiShop, "Modern Physical Metallurgy and Materials Engineering," *Mod. Phys. Metall. Mater. Eng.*, pp. 320–350, 1999.

[11] Oxtoby D. W., "Homogeneous nucleation: theory and experiment," *J. Phys. Condens. Matter*, vol. 4, p. 38, 1992.

[12] S. F. Jones, G. M. Evans, and K. P. Galvin, "The cycle of bubble production from a

gas cavity in a supersaturated solution," *Adv. Colloid Interface Sci.*, vol. 80, no. 1, pp. 51–84, 1999.

[13] W. A. Gerth and E. A. Hemmingsen, "Heterogeneous nucleation of bubbles at solid surfaces in gas-supersaturated aqueous solutions," *J. Colloid Interface Sci.*, vol. 74, no. 1, pp. 80–89, 1980.

[14] A. G. Tenner, "Nucleation in bubble chambers," *Nucl. Instruments Methods*, vol. 22, pp. 1–42, 1963.

[15] H. Y. Kwak and S. D. Oh, "Gas–vapor bubble nucleation—a unified approach," *J. Colloid Interface Sci.*, vol. 278, no. 2, pp. 436–446, 2004.

[16] S. Siedel, S. Cioulachtjian, and J. Bonjour, "Experimental analysis of bubble growth, departure and interactions during pool boiling on artificial nucleation sites," *Exp. Therm. Fluid Sci.*, vol. 32, pp. 1504–1511, 2008.

[17] X. Fu, P. Zhang, C. J. Huang, and R. Z. Wang, "Bubble growth, departure and the following flow pattern evolution during flow boiling in a mini-tube," *Int. J. Heat Mass Transf.*, vol. 53, no. 21–22, pp. 4819–4831, 2010.

[18] B. Bon, C. K. Guan, and J. F. Klausner, "Heterogeneous nucleation on ultra smooth surfaces," *Exp. Therm. Fluid Sci.*, vol. 35, no. 5, July, p. 746, 2011.

[19] C. Han and P. Griffith, "The Mechanism of Heat Transfer In Nucleate Pool Boiling," *Rep. No . 7673-19 , Dep. Mech. Eng. Massachusetts Inst. Technol.*, p. 19, 1962.

[20] D. Farajisarir, "Growth and Collapse of Vapour Bubbles in Convective subcooled boiling of water," 1993.

[21] Y. Y. Hsu, "On the size range of active nucleation cavities on a heating surface," *J. Heat Transfer*, vol. 84, pp. 207–216, 1962.

[22] D. B. R. Kenning, "Nucleate Boiling," *Thermopedia*, 2011.

[23] H. S. Lee and H. Merte, "Spherical vapor bubble growth in uniformly superheated liquids," *Int. J. Heat Mass Transf.*, vol. 39, no. 12, pp. 2427–2447, 1996.

[24] N. Divinis, M. Kostoglou, T. D. Karapantsios, and V. Bontozoglou, "Self-similar growth of a gas bubble induced by localized heating: The effect of temperature-dependent transport properties," *Chem. Eng. Sci.*, vol. 60, no. 6, pp. 1673–1683, 2005.

[25] N. Divinis, T. D. Karapantsios, R. Bruijin, M. Kostoglou, V. Bontozoglou, and J. Legros, "Bubble Dynamics During Degassing of Liquids at Microgravity Conditions," *AIChE*, vol. 52, no. J., pp. 3029–40, 2006.

[26] H. D. Haustein, G. F. Dietze, and R. Kneer, “A New Empirical Model for Bubble Growth: Boiling in an Infinite Medium and on a Wall at High Superheat,” *ASME/JSME 2011 8th Therm. Eng. Jt. Conf.*, vol. 135, no. July 2013, pp. T10236-T10236-10, 2011.

[27] L. Reyleigh, “On the pressure developed in a liquid during the collapse of a spherical cavity,” *Phil. M.*, vol. 34, no. Series 6, pp. 94–98, 1917.

[28] J. G. Collier and J. R. Thome, “Convective boiling and condensation,” *(3rd Ed.), Oxford Univ. Press*, pp. 99–280, 1994.

[29] S. J. D. Van Stralen, “The growth rate of vapour bubbles in superheated pure liquids and binary mixtures,” *Int. J. Heat Mass Transf.*, vol. 11, no. 10, pp. 1467–1489, 1968.

[30] M. S. Plesset and S. A. Zwick, “The growth of vapor bubbles in superheated liquids,” *J. Appl. Phys.*, vol. 25, no. 4, pp. 493–500, 1954.

[31] P. Dergarabedian, “The rate of growth of vapor bubbles in superheated water,” *J. Appl. Mech.*, vol. 20, pp. 537–545, 1953.

[32] H. K. Forster and N. Zuber, “Growth of a vapor bubble in a superheated liquid,” *J. Appl. Phys.*, vol. 25, no. 4, pp. 474–478, 1954.

[33] G. Birkhoff, R. S. Margulies, and W. A. Horning, “Spherical Bubble Growth,” *Phys. Fluids*, vol. 1, no. 3, pp. 201–204, 1958.

[34] L. E. Scriven, “On the dynamics of phase growth,” *Chem. Eng. Sci.*, vol. 1, pp. 1–13, 1959.

[35] P. G. Kosky, “Bubble growth measurements in uniformly superheated liquids,” *Chem. Eng. Sci.*, vol. 23, no. 7, pp. 695–706, 1968.

[36] L. W. Florschuetz, C. L. Henry, and A. R. Khan, “Growth rates of free vapor bubbles in liquids at uniform superheats under normal and zero gravity conditions,” *Int. J. Heat Mass Transf.*, vol. 12, no. 11, pp. 1465–1489, 1969.

[37] B. Mikic, W. M. Rohsenow, and P. Griffith, “On bubble growth rates,” *Int. J. Heat Mass Transf.*, vol. 13, no. 4, pp. 657–666, 1970.

[38] Y. C. Lien, “Bubble growth rates at reduced pressure,” MIT, 1969.

[39] A. Luke, “Interactions between bubble formation and heating surface in nucleate boiling,” *Exp. Therm. Fluid Sci.*, vol. 35, no. 5, pp. 753–761, 2011.

[40] W. Zijl, D. Moalem, and S. J. D. Van Stralen, “Inertia and Diffusion controlled Bubble Growth and implosion in initially uniform Pure and Binary systems,” *Lett. Heat Mass Transf.*, vol. 4, pp. 331–339, 1977.

[41] J. Kim, “Review of nucleate pool boiling bubble heat transfer mechanisms,” *Int. J. Multiph. Flow*, vol. 35, no. 12, pp. 1067–1076, 2009.

[42] M. Bongué-Boma and M. Brocato, “Liquids with vapour bubbles,” *Comput. Math. with Appl.*, vol. 55, no. 2, pp. 268–284, 2008.

[43] W. Fritz, “Maximum Volume of Vapor Bubbles,” *Phys Z*, vol. 36, pp. 379–384, 1935.

[44] M. Colombo and M. Fairweather, “Prediction of bubble departure in forced convection boiling: A mechanistic model,” *Int. J. Heat Mass Transf.*, vol. 85, pp. 135–146, 2015.

[45] W. G. J. Van Helden, C. W. M. Vander Geld, and Boot P. G. M., “Forces on bubbles growing and detaching in flow along a vertical wall,” *Int. J. Heat Mass Transf.*, vol. 38, no. 11, pp. 2075–2088, 1995.

[46] S. G. Kandlikar, V. K. Dhir, and M. Shoji, *Handbook of Phase Change: Boiling and Condensation*, vol. 53. Philadelphia, PA: Taylor and Francis, 1999.

[47] H. J. Ivey, “Relationships between bubble frequency, departure diameter and rise velocity in nucleate boiling,” *Int. J. Heat Mass Transf.*, vol. 10, no. 8, pp. 1023–1040, 1967.

[48] I. G. Malenkov, “The Frequency of vapour bubble seperation as Funcion of Bubble size,” *Fulid Mech. Sov. Res.*, vol. 1, pp. 36–42, 1971.

[49] R. Situ, M. Ishii, T. Hibiki, J. Y. Tu, G. H. Yeoh, and M. Mori, “Bubble departure frequency in forced convective subcooled boiling flow,” *Int. J. Heat Mass Transf.*, vol. 51, no. 25–26, pp. 6268–6282, 2008.

[50] T. Jin, S. Y. Zhang, K. Tang, and Y. Z. Huang, “Observation and analysis of the detachment frequency of coalesced bubbles in pool boiling liquid nitrogen,” *Cryogenics (Guildf).*, vol. 51, no. 9, pp. 516–520, 2011.

[51] P. W. McFadden and P. Grassmann, “The relation between bubble frequency and diameter during nucleate pool boiling,” *Int. J. Heat Mass Transf.*, vol. 5, no. 3–4, pp. 169–173, 1962.

[52] H. Sakashita and T. Kumada, “Method for predicting boiling curves of saturated nucleate boiling,” *Int. J. Heat Mass Transf.*, vol. 44, no. 3, pp. 673–682, 2001.

[53] T. G. Theofanous, J. P. Tu, a T. Dinh, and T. N. Dinh, “The Boiling Crisis Phenomenon Part I: nucleation and nucleate boiling heat transfer,” *Exp. Therm. Fluid Sci. P*, vol. 26, pp. 775–792, 2002.

[54] J. R. Thome, *Enhanced Boiling Heat Transfer*. Hemisphere Pub. Corp.(Taylor &

Francis), 1990.

[55] J. R. Thome, "Boiling in microchannels: A review of experiment and theory," *Int. J. Heat Fluid Flow*, vol. 25, no. 2, pp. 128–139, 2004.

[56] V. Prodanovic, D. Fraser, and M. Salcudean, "On the transition from partial to fully developed subcooled flow boiling," *Int. J. Heat Mass Transf.*, vol. 45, no. 24, pp. 4727–4738, 2002.

[57] F. J. Lesage, S. Siedel, J. S. Cotton, and A. J. Robinson, "A mathematical model for predicting bubble growth for low Bond and Jakob number nucleate boiling," *Chem. Eng. Sci.*, vol. 112, pp. 35–46, 2014.

[58] Y. J. Cho, S. B. Yum, J. H. Lee, and G. C. Park, "Development of bubble departure and lift-off diameter models in low heat flux and low flow velocity conditions," *Int. J. Heat Mass Transf.*, vol. 54, no. 15–16, pp. 3234–3244, 2011.

[59] D. Lucas, E. Krepper, and H. M. Prasser, "Use of models for lift, wall and turbulent dispersion forces acting on bubbles for poly-disperse flows," *Chem. Eng. Sci.*, vol. 62, no. 15, pp. 4146–4157, 2007.

[60] R. Kurose and S. Komori, "Drag and lift forces on a rotating sphere in a linear shear flow," *J. Fluid Mech.*, vol. 384, pp. 183–206, 1999.

[61] J. F. Klausner, R. Mei, D. M. Bernhard, and L. Z. Zeng, "Vapor bubble departure in forced convection boiling," *Int. J. Heat Mass Transf.*, vol. 36, no. 3, pp. 651–662, 1993.

[62] Buyevich Y. A. and Webbon B.W., "Bubble formation at a submerged orifice in reduced gravity," *Chem. Eng. Sci.*, vol. 41, no. 21, pp. 4843–4857, 1996.

[63] K. Sugioka and T. Tsukada, "Direct numerical simulations of drag and lift forces acting on a spherical bubble near a plane wall," *Int. J. Multiph. Flow*, vol. 71, pp. 32–37, 2015.

[64] W. Dijkhuizen, E. I. V. van den Hengel, N. G. Deen, M. van Sint Annaland, and J. A. M. Kuipers, "Numerical investigation of closures for interface forces acting on single air-bubbles in water using Volume of Fluid and Front Tracking models," *Chem. Eng. Sci.*, vol. 60, no. 22, pp. 6169–6175, 2005.

[65] R. Sugrue and J. Buongiorno, "A modified force-balance model for prediction of bubble departure diameter in subcooled flow boiling," *Nucl. Eng. Des.*, vol. 305, pp. 717–722, 2016.

[66] B. J. Yun, A. Splawski, S. Lo, and C. H. Song, "Prediction of a subcooled boiling flow with advanced two-phase flow models," *Nucl. Eng. Des.*, vol. 253, pp. 351–

359, 2012.

[67] R. M. Sugrue, “The Effects of Orientation Angle , Subcooling , Heat Flux , Mass Flux , and Pressure on Bubble Growth and Detachment in Subcooled Flow Boiling,” Massachusetts Institute of Technology, Cambridge, MA, 2012.

[68] G. H. Yeoh and J. Y. Tu, “A unified model considering force balances for departing vapour bubbles and population balance in subcooled boiling flow,” *Nucl. Eng. Des.*, vol. 235, no. 10–12, pp. 1251–1265, 2005.

[69] M. R. Nematollahi, S. Toda, and H. Hashizume, “Characteristics Phenomenoa of subcooled flow boiling instability,” *Proc. Sixth Int. Conf. Nucl. Eng.*, p. Paper No. 6403, 1998.

[70] M. R. Nematollahi, S. Toda, and H. Hashizume, “Vibration characteristics of subcooled flow boiling instability,” *1st Eur. Japanese Two-Phase flow Gr. Meet. 36th Eur. Two-Phase flow Gr. Meet.*, p. Portproz, Slovenia, 1998.

[71] M. R. Nematollahi, S. Toda, H. Hashizume, and K. Yuki, “Vibration Characteristic of Heated Rod Induced by Subcooled Flow Boiling,” *J. Nucl. Sci. Technol.*, vol. 36, no. 7, pp. 575–583, 1999.

[72] M. R. Nematollahi, “Evaluation of Exerting Force on the Heating Surface Due to Bubble Ebullition in Subcooled Flow Boiling,” *World Acad. Sci. Eng. Technol.*, vol. 2, pp. 401–408, 2008.

[73] H. F. Smirnov, V. V Zrodnikov, and I. L. Boshkova, “Thermoacoustic phenomena at boiling subcooled liquid in channels,” *Int. J. Heat Mass Transf.*, vol. 40, no. 8, pp. 1977–1983, 1997.

[74] P. Zhang, M. Murakami, R. Z. Wang, and H. Inaba, “Study of film boiling in He II by pressure and temperature oscillation measurements,” *Cryogenics (Guildf).*, vol. 39, no. 7, pp. 609–615, 1999.

[75] A. C. Leonard, “Helium -2 noisy film boiling and silent film boiling heat transfer coefficient values,” *Proc ICEC*, vol. 3, p. 109, 1970.

[76] P. Bussieres and A. C. Leonard, “Noise associated with heat transfer to liquid helium II,” *Bull IIR Annex.*, vol. 5, p. 61, 1966.

[77] D. M. Coulter, A. C. Leonard, and J. G. Pike, “Heat transport visualization in helium II using focused shadowgraph and Schlieren techniques,” *Adv Cryog Eng.*, vol. 13, p. 640, 1968.

[78] F. L. Eisinger, J. T. Francis, and R. E. Sullivan, “Prediction of Acoustic Vibration in Steam Generator and Heat Exchanger Tube Banks,” *J. Press. Vessel Technol.*,

vol. 118, no. 2, pp. 221–236, 1996.

[79] R. D. Blevins, *Flow-induced vibration*, 2nd ed. New York: Van Nostrand reinhold Press, 1977.

[80] M. P. Paidoussis, “Flow-induced vibrations in nuclear reactors and heat exchangers: practical experiences and state of knowledge,” *Pract. Exp. with Flow-Induced Vib. Springer-Verlag*, no. Berlin, pp. 1–81.

[81] H. G. D. Goyder, “Flow-Induced Vibration in Heat Exchangers,” *Inst. Chem. Eng. Trans IChemE*, vol. 80A, no. 3, pp. 226–232, 2002.

[82] F. Axisa, J. Antunes, and B. Villard, “Random excitation of heat exchangertubes by cross-flows,” *J. Fluids Struct.*, vol. 4, no. 3, pp. 321–341, 1990.

[83] C. Zhang, M. J. Pettigrew, and N. W. Mureithi, “Correlation Between Vibration Excitation Forces and the Dynamic Characteristics of Two-Phase Cross Flow in a Rotated-Triangular Tube Bundle,” *ASME J. Press. Vessel Technol.*, vol. 130, pp. 1–10, 2008.

[84] M. J. Pettigrew and C. E. Taylor, “Two-Phase Flow-Induced Vibration : An Overview,” *ASME J. Press. Vessel Technol.*, vol. 116, pp. 233–253, 1994.

[85] M. J. Pettigrew, C. Zhang, N. W. Mureithi, and D. Pamfil, “Detailed flow and force measurements in a rotated triangular tube bundle subjected to two-phase cross-flow,” *J. Fluids Struct.*, vol. 20, no. 4 SPEC. ISS., pp. 567–575, 2005.

[86] T. Nakamura, K. Fujita, N. Kowanishi, N. Yamaguchi, and A. Tsuge, “Study on the vibration characteristics of a tube array caused by two-phase flow, part 1: random vibration,” *J. Fluids Struct.*, vol. 9, pp. 519–538, 1995.

[87] C. Zhang, M. J. Pettigrew, and N. W. Mureithi, “Quasi-periodic vibration excitation mechanisms due to two-phase cross flow in steam generator tube bundles,” *Proc. 5th CNS Int. Steam Gener. Conf.*, no. Toronto, Canada, 2006.

[88] C. Zhang, M. J. Pettigrew, and N. W. Mureithi, “Vibration Excitation Force Measurements in a Rotated Triangular Tube Bundle Subjected to Two-Phase Cross Flow,” *ASME J. Press. Vessel Technol.*, vol. 129, pp. 21–27, 2007.

[89] M. J. Pettigrew and G. D. Knowles, “Some Aspects of Heat-Exchanger Tube Damping in Two-Phase Mixtures,” *J. Fluids Struct.*, vol. 11, no. 8, pp. 929–945, 1997.

[90] F. Hara, “A theory on the two-phase flow-induced vibrations in piping systems,” *Trans. 3rd Int. Conf. Struct. Mech. React. Technol.*, vol. Paper No., p. London, U.K., 1975.

[91] Y. Liu *et al.*, "Experimental study of internal two-phase flow induced fluctuating force on a 90 degree elbow," *Chem. Eng. Sci.*, vol. 76, pp. 173–187, 2012.

[92] S. Miwa *et al.*, "Study of unsteady gas-liquid two-phase flow induced force fluctuation (Part 1: Evaluation and modeling of two-phase flow induced force fluctuation)," *Trans. JSME (in Japanese)*, vol. 80, pp. 1–11, 2014.

[93] C. Zhang, M. J. Pettigrew, and N. . Mureithi, "Correlation Between Vibration Excitation Forces and the Dynamic Characteristics of Two-Phase Flow in a Rotated Triangular Tube Bundle," *ASME J. Press. Vessel Technol.*, vol. 130, pp. 1–10, 2008.

[94] C. Zhang, N. W. Mureithi, and M. J. Pettigrew, "Development of models correlating vibration excitation forces to dynamic characteristics of two-phase flow in a tube bundle," *Int. J. Multiph. Flow*, vol. 34, no. 11, pp. 1048–1057, 2008.

[95] S. Miwa *et al.*, "Study of unsteady gas-liquid two-phase flow induced force fluctuation (Part 2: Horizontal downward two phase flow)," *Trans. JSME (in Japanese)*, vol. 80, pp. 1–11, 2014.

[96] T. Hibiki and M. Ishii, "One-dimensional drift-flux model and constitutive equations for relative motion between phases in various two-phase flow regimes," *Int. J. Heat Mass Transf.*, vol. 46, no. 25, pp. 4935–4948, 2003.

[97] C. Charreton, C. Béguin, a. Ross, S. Étienne, and M. J. Pettigrew, "Two-phase damping for internal flow: Physical mechanism and effect of excitation parameters," *J. Fluids Struct.*, vol. 56, pp. 56–74, 2015.

[98] M. An, M. Liu, Y. Ma, and X. Xu, "Multi-scale vibration behavior of a graphite tube with an internal vapor-liquid-solid boiling flow," *Powder Technol.*, vol. 291, pp. 201–213, 2016.

[99] C. C. Feng, "The measurement of vortex idunced effects in flow past stationary and oscillating circular and D-section cylinders," 1968.

[100] N. Cagney and S. Balabani, "Wake modes of a cylinder undergoing free streamwise vortex-induced vibrations," *J. Fluids Struct.*, vol. 38, pp. 127–145, 2013.

[101] Y. S. Shin and M. W. Wambsganss, "Flow-Induced Vibration in LMFBR Steam Generators : A State of the Art Review," *Nucl. Eng. Des.*, vol. 40, no. 2, pp. 235–284, 1977.

[102] J. H. Lienhard, "Synopsis of lift, drag, and vortex frequency data for rigid circular cylinders," *Bulletin 300*. p. Technical Extension Service, Washington State Univ, 1966.

[103] B. W. Roberts, “Low Frequency, self-excited vibration in a row of circular cylinders mounted in an airstream.,” 1962.

[104] B. W. Roberts, “Low frequency, aeroelastic vibrations in a cascade of circular cylinders,” *Inst. Mech. Eng.*, p. London, 1966.

[105] M. P. Païdoussis, “A review of flow-induced vibrations in reactors and reactor components,” *Nucl. Eng. Des.*, vol. 74, no. 1, pp. 31–60, 1983.

[106] N. Zuber, “Hydrodyanic aspects of boiling heat transfer,” *US AEC Rep. AECU 4439*, p. June, 1959.

[107] R. Cole and H. L. Shulman, “Bubble departure diameters at subatmospheric pressures,” *Chem. Eng. Prog. Symp. Ser.*, vol. 62, pp. 6–16, 1966.

[108] R. Cole, “Bubble frequencies and departure volumes at sub-atmospheric pressures,” *AIChE J*, vol. 13, no. 4, pp. 779–783, 1967.

[109] R. Cole and W. M. Rohsenow, “Correlation of bubble departure diameter for boiling of saturated liquids,” *Chem. Eng. Prog. Symp. Ser.*, vol. 65, pp. 211–213, 1969.

[110] R. Ruckenstein, “Recent trends in boiling heat and mass transfer,” *APPI Mech. Rev.*, vol. 17, pp. 663–672, 1964.

[111] S. J. D. Van Stralen and W. Zijl, “Fundamental developments in bubble dynamics,” *Proc. Sixth Int. Heat Transf. Conf. Torronto*, vol. 6, pp. 429–450, 1978.

[112] U. Stephan Wenzel, “Saturated pool boiling and Subcooled flow boiling mixtures at Atmospheric Pressure,” Ph. D.thesis, University of Auckland, New Zealand, 1993.

[113] J. Kim and M. H. Kim, “On the departure behaviors of bubble at nucleate pool boiling,” *Int. J. Multiph. Flow*, vol. 32, no. 10–11, pp. 1269–1286, 2006.

[114] H. C. Lee, B. Do Oh, S. W. Bae, and M. H. Kim, “Single bubble growth in saturated pool boiling on a constant wall temperature surface,” *Int. J. Multiph. Flow*, vol. 29, no. 12, pp. 1857–1874, 2003.

[115] J. N. Koster and R. L. Sani, “Low-Gravity Fluid Dynamics and Transport Phenomena.” Progress in Astronautics and Aeronautics, 1990.

[116] P. G. Saffman, “The lift on a small sphere in a slow shear flow,” *J. Fluid Mech.*, vol. 22, no. 2, pp. 385–400, 1965.

[117] T. R. Auton, “The lift force on a spherical body in a rotational flow,” *J. Fluid Mech.*, vol. 183, pp. 199–218, 1987.

[118] R. Mei and J. F. Klausner, “Shear lift force on spherical bubbles,” *Int. J. Heat Fluid Flow*, vol. 15, pp. 62–65, 1994.

[119] A. Tomiyama, "Drag and lift and virtual mass forces acting on a single bubble," *3rd Int. Symp. Two-phase Flow Model. Exp.*, no. September, p. Pisa, Italy, 2004.

[120] A. Tomiyama, H. Tamai, I. Zun, and S. Hosokawa, "Transverse migration of single bubbles in simple shear flows," *Chem. Eng. Sci.*, vol. 57, no. 11, pp. 1849–1858, 2002.

[121] I. G. Malenkov, "The frequency of Vapor Bubble Seperation as Function of Bubble Size," *Fluid Mech. Sov. Res.*, vol. 1, pp. 36–42, 1971.

[122] L. Z. Zeng, J. F. Klausner, and R. Mei, "A unified model for the prediction of bubble detachment diameters in boiling systems- I. Pool boiling," *Int. J. Heat Mass Transf.*, vol. 36, no. 9, pp. 2261–2270, 1993.

[123] T. G. Leighton, "The translating bubble," in *The Acoustic Bubble*, 1st Editio., Academic press, London, 1997, pp. 116–117.

[124] T. G. Leighton, *The Acoustic Bubble*, vol. 96. 1994.

[125] H. Lamb, *Hydrodynamics*, 6th ed. Dover, New York, 1945, 1945.

[126] B. O. Peirce, "A Short Table of Integrals." Ginn & Company, The Athenaum Press, Boston, USA, 1899.

[127] F. J. Fahy and G. Paolo, *Sound and structural vibration: radiation, transmission and response*. Academic press, 2007.

[128] A. S. Scott *et al.*, "A novel method for the measurement of mechanical mobility," *J. Sound Vib.*, vol. 320, no. 3, pp. 559–575, 2009.

[129] W. Xu and L. L. Koss, "Frequency response functions for structural intensity Part I: Theory," *J. Sound Vib.*, vol. 185, no. 2, pp. 299–334, 1995.

[130] ISO 7626-1., "Vibration and shock - Experimental determination of mechanical mobility – Part 1: Basic definitions and transducers." International Organization for Standardization, Geneva, p. 23, 1986.

[131] U. Ingard, *Notes on Acoustics*. Laxmi Publications Ltd, 2010.

[132] P. Gardonio and M. J. Brennan, "On the Origins and Development of Mobility and Impedance Methods in Structural Dynamics," *J. Sound Vib.*, vol. 249, no. 3, pp. 557–573, 2002.

[133] F. Fahy and J. Walker, *Advanced Applications in Acoustics, Noise and Vibration*. CRC Press, 2004.

[134] H. P. Olesen and R. B. Randall, "A Guide to Mechanical Impedance and Structural Response Techniques," 1977.

[135] M. J. Crocker, "Handbook of Acoustics." John Wiley & Sons, 1998.

[136] A. W. Leissa, *Vibration of shells*, vol. 288, no. 9. Washington, DC, USA: Scientific and Technical Information Office, National Aeronautics and Space Administration, 1973.

[137] A. Farshidianfar, M. H. Farshidianfar, M. J. Crocker, and W. O. Smith, “Vibration analysis of long cylindrical shells using acoustical excitation,” *J. Sound Vib.*, vol. 330, no. 14, pp. 3381–3399, 2011.

[138] L. Bing-ru, W. Xuan-yin, G. Hui-liang, and D. Yuan-ming, “Study on applicability of modal analysis of thin finite length cylindrical shells using wave propagation approach,” *J. Zhejiang Univ. Sci.*, vol. 6A, no. 10, pp. 1122–1127, 2005.

[139] S. S. Rao, *Vibration of continuous systems*. John Wiley & Sons, 2007.

[140] M. Heckl, “Vibrations of Point Driven Cylindrical Shells,” *J. Acoust. Soc. Am.*, vol. 34, no. 10, pp. 1553–1557, 1962.

[141] S. A. Hambric, “Structural Acoustics Tutorial—Part 1: Vibrations in Structures,” *Acoust. Today*, vol. 2, no. 4, pp. 21–33, 2006.

[142] A. P. G. Peterson, J. Gross, and E. Ervin, *Handbook of Noise Measurements*, Seventh Ed. General Radio Comany, 1972.

[143] J. F. James, *A student’s guide to Fourier Transforms: with applications in physics and engineering*. Cambridge university press, 2011.

[144] R. K. Sinnott, *Chemical Engineering Design*, 4th ed., vol. 6. Elsevier Butterworth-Heinemann, 2005.

[145] T. M. Flynn, J. W. Draper, and J. J. Roos, “The Nucleate and Film Boiling Curve of Liquid Nitrogen at One Atmosphere,” *Adv. Cryog. Eng.*, vol. 7, pp. 539–545, 1962.

[146] M. Kida, Y. Kikuchci, O. Takahashi, and I. Takahashi, “Pool-Boiling Heat Transfer in Liquid Nitrogen,” *J. Nucl. Sci. Technol.*, vol. 18, no. 7, pp. 501–513, 1981.